Linearity, Shift-Invariance and Resolution Improvement for Quantitative Magnetic Particle Imaging

by

Kuan Lu

A dissertation submitted in partial satisfaction of the

requirements for the degree of

Joint Doctor of Philosophy
with University of California, San Francisco

in

Bioengineering

in the

Graduate Division
of the
University of California, Berkeley

Committee in charge:

Professor Steven Conolly, Chair
Professor John Clarke
Professor John Kurhanewicz

Spring 2015

Linearity, Shift-Invariance and Resolution Improvement for Quantitative Magnetic Particle Imaging

Abstract

Linearity, Shift-Invariance and Resolution Improvement for Quantitative Magnetic Particle Imaging

by

Kuan Lu
Joint Doctor of Philosophy
with University of California, San Francisco in Bioengineering

University of California, Berkeley

Professor Steven Conolly, Chair

Magnetic Particle Imaging (MPI) is an emerging tracer imaging modality that utilizes safe, low-frequency magnetic fields and an existing, human-safe, superparamagnetic iron oxide (SPIO) nanoparticle tracer. MPI already shows high contrast and high sensitivity in small animal imaging. The technique exploits the nonlinear magnetization response of SPIO nanoparticles to time-varying magnetic fields at very low frequencies (VLF). Hence, for medical imaging, MPI only detects a signal from the tracers and not from the diamagnetic biological tissue. Moreover, since tissue is completely transparent to VLF magnetic fields, there is no depth attenuation of the MPI signal. Thus, the physics of MPI shows that it has the ideal contrast for tracer imaging, and is ideally suited for clinical applications such as angiography, cancer imaging, inflammation imaging, and *in vivo* stem cell therapy tracking.

The fundamental advantages of MPI as a tracer imaging modality are its superb tracer sensitivity, ideal image contrast, and safety of the tracer and modality. Our lab has already shown experimentally that MPI can detect a minuscule sample of 10 nanogram (100 nM) of tracer in a prototype scanner. In principle, there is another 2 orders of magnitude achievable improvement before the sensitivity reaches the physical limit of the technique. MPI is currently shown to have 200x higher net signal-to-noise ratio (SNR) than magnetic resonance imaging (MRI), and this sensitivity is approaching that of the nuclear medicine, such as positron emission tomography (PET) and single-photon emission computerized tomography (SPECT). Moreover, because MPI tracer is not radioactive, the dose-limited sensitivity can easily exceed PET and SPECT and effectively be more sensitive. MPI has ideal image contrast because the contrast is positive, quantitative, has no tissue background, and independent of depth. Lastly, MPI has ideal tracer and modality safety. MPI tracers, notably SPIO nanoparticles, have been shown to be much safer for patients with chronic kidney disease than currently available tracers (iodine and gadolinium) used in planar X-ray imaging, X-ray computed tomography (CT), and MRI. In addition, MPI uses no ionizing radiation, and thus is safer than X-ray, CT, PET and SPECT.

MPI is still a young technology in the medical imaging field. With 10 years of development since the first introduction of the technique in 2005, the current state of MPI research is very much like MRI in the 1980s. There remain many open challenges to be addressed, which makes this field very exciting. In this thesis, we will investigate and address three major challenges in MPI that are crucial for the preclinical and clinical adoption. These challenges are: 1) Restoration of MPI's linearity and shift-invariance (LSI), which are hallmarks of almost all clinically relevant imaging modalities; 2) Achieving isotropic resolution,which is an indispensable characteristic for any diagnostic and quantitative imaging technique; and 3) Understanding the source of the background image haze and eliminate it, which is essential for further improving image resolution, contrast and conspicuity.

We begin by investigating the LSI properties in MPI. In MPI, high-pass filters designed to remove unavoidable direct feedthrough interference also remove information crucial to ensuring LSI in MPI scans. We present a complete theoretical and experimental description of the image artifacts from filtering, and propose and validate a robust algorithm to completely restore the lost information for the x-space MPI method. We provide the theoretical, simulated, and experimental proof that our algorithm indeed restores the LSI properties of MPI, which is indispensable for quantification and diagnostic utility.

We then detailed an investigation into one of MPI's unique resolution challenge: MPI's point spread function (PSF) is highly dependent on the scanning parameters, and every experimental MPI scan ever created lacks desirable isotropic resolution, which leads to ambiguous and inaccurate diagnosis. In this thesis, we generalized a tensor imaging theory for multidimensional x-space MPI to explore the physical source of this anisotropy, presented a multichannel hardware and scanning trajectory to remove anisotropy, and designed and constructed two orthogonal excitation and detector coils to enable isotropic resolution. We experimentally verified the resolution improvement with the new hardware and reconstruction, and showed that isotropic resolution enabled accurate diagnosis of stenosis in small human arterial phantoms.

Lastly, we investigated on MPI's reduced image contrast due to significant background image haze. We have found that the image haze comes from the undesirable rotation of the nanoparticle magnetic moment in response to the applied field outside of the scanning region. Consequently, the native PSF contains a hazy component that falls off as 1/Gr, where G is the gradient field strength, and r is the radially symmetric spatial coordinate. This haze resembles the haze seen in CT images reconstructed with non-filtered backprojection. We propose that we can reshape the MPI PSF with k-space equalization filter that dehazes the image without any noise amplification. We demonstrate experimentally that equalization dramatically increases image conspicuity and enables the first quantitative measurements of lumen size in a sub-millimeter diameter blood vessel phantom.

In conclusion, this thesis work has proposed significant advancement in imaging theory, hardware and algorithm for MPI that ensures LSI properties, and improves image resolution, contrast and conspicuity. Taken together, these are major contributions to the fundamental imaging science of MPI. LSI and sharp isotropic resolution is essential for quantitative imaging, and could foster clinical adoption of MPI.

A dedication to my heavenly Father, my husband, my parents, my wonderful church community at Gracepoint, and my friends.

Acknowledgments

This work would not have been possible without the constant support and guidance from my advisor, Professor Steven Conolly, for the past 6 years. I would also like to thank Dr. Patrick Goodwill and Dr. Emine Ulku Saritas for their mentorship, and my husband as well as my great work companion, Bo Zheng, for his unfailing support and insight. Last but not the least, I would like to thank all of the rest of my lab, Laura Croft, Justiin Konkle, Paul Keselman, Daniel Hensley, Elaine Yu, Ryan Orendorff, Zhiwei Tay and my undergraduate researcher, Mindy Bishop, for their enthusiastic help with many aspects of the experimentation.

The authors gratefully acknowledge support from these research grants: CIRM Tools and Technology Grant RT2-01893, NIH R01 5R01EB013689-03, Keck Foundation 034317, NIH R24 1R24MH106053-01, NIH R01 1R01EB019458-01, ACTG 037829, and two years of CIRM predoctoral fellowship 2013-2014. The contents of this thesis are solely the responsibility of the authors and do not necessarily represent the official views of CIRM, the National Institutes of Health, Keck foundation, ACTG or any other agency of the State of California.

Contents

List of Figures

List of Tables

List of Acronyms

MPI	Magnetic Particle Imaging
SPIO	Superparamagnetic Iron Oxide
VLF	Very Low Frequencies
LSI	Linearity and Shift-Invariant
CT	Computerized Tomography
MRI	Magnetic Resonance Imaging
PET	Positron Emission Tomography
DC	Direct Current
FFP	Field-Free Point
FFL	Field-Free Line
DC	Direct Current
FOV	Field of View
pFOV	Partial Field of View
PSF	Point Spread Function
SNR	Signal to Noise Ratio
FFT	Fast Fourier Transform
CTA	CT Angiography
MRA	Magnetic Resonance Angiography
FBP	Filtered Back Projection
FWHM	Full Width at Half Maximum
SAR	Specific Absorption Rate

Notation and Symbols

Chapter 2

$\vec{\mathbf{x}}$	Spatial Location Vector.
$\mathbf{h}(\vec{\mathbf{x}})$	Point Spread Function.
$h_{ij}\left(\vec{\mathbf{x}}\right)$	i,jth Component of $\Omega(\vec{\mathbf{x}})$.
$E_T(\vec{\mathbf{x}})$	Tangential Envelope (Good Resolution).
$E_N(\vec{\mathbf{x}})$	Normal Envelope (Bad Resolution).
$\mathbf{W}_T(\vec{\mathbf{x}})$	Tangential Weighting Matrices.
$\mathbf{W}_N(\vec{\mathbf{x}})$	Normal Weighting Matrices.
$\boldsymbol{\Omega}(\vec{\mathbf{x}})$	Multidimensional Image tensor.
$\hat{\rho}_{ij}(\vec{\mathbf{x}})$	i,j th Component of $\Omega(\vec{\mathbf{x}})$.
$\vec{\mathbf{u}}_a\left(t\right)$	Excitation vector.
$\vec{\mathbf{u}}_b\left(t\right)$	Detection vector.
$\hat{\rho}_{\tilde{\mathbf{u}}_a,\tilde{\mathbf{u}}_b}\left(\vec{\mathbf{x}},t\right)$	Image with Tx/Rx Vector $\tilde{\mathbf{u}}_a\left(t\right)$ and $\tilde{\mathbf{u}}_b\left(t\right)$.
$\hat{\rho}(\vec{\mathbf{x}})$	Isotropic Summed Image.
$\mathbf{G}$	Gradient Matrix.

Preface

When I first joined the Conolly lab, the field of Magnetic Particle Imaging has only been established for 4 years, started by an excellent 2005 Nature paper by Gleich *et al* at Philips. Our lab was intrigued by the great clinical potential of MPI as a highly sensitive and safer alternative for tracer and molecular imaging, but at the same time, we were faced with many open challenges of this technique. Some of these challenges are so unique that there are no parallels in the medical imaging field.

We were also caught in a worldview switch in terms of how do we view the MPI imaging physics. The original Philips paper views the MPI as a nonlinear harmonic imaging technique. The authors record the harmonic response of the particles to the single frequency drive field. To reconstruct the input particle distribution from the detected signal spectrum, one needs the *a prior* information of the "system functions", which is a verbose matrix of all the harmonic signatures from a point source placed at every location within the imaging field of view (FOV). Using algebraic reconstruction techniques, the authors then invert their library of "system functions" to produce an image. The "system functions" are acquired for every study in a calibration procedure through the FOV using the same tracer per study. This reconstruction is ill-posed because the "system functions" have poor condition number and are susceptible to system noise, change of tracers and the microenvironment of the tracers.

Coming from a linear systems background, our lab did not understand this approach. In 2009, our lab proposed to use linear and shift-invariant (LSI) theory to analyze MPI, which is what we called "x-space" theory. We proposed that MPI could be actually viewed as a real time sensitive point method, where as we raster the field free point across the FOV in a controlled manner, we know that the instantaneous signal induced in the receiver coil must be from the response of the particles from the location the FFP scans across at the same time. With this temporal-spatial correlation determined by the FFP trajectory, we could directly reconstruct our temporal signal and grid them onto the imaging FOV and thus form an image. Moreover, the x-space worldview characterizes MPI to be an LSI system, with powerful implications that helps us to define SNR, resolution, LSI and other important discussions for the first time. With this powerful and elegent x-space imaging theory, we went on trying to improve the performance of MPI system.

We first encountered the direct feedthrough challenge in MPI. In MPI, the excitation and detection occur simultaneously because the particle responds to the external excitation instantaneously. Thus, there is no temporal separation of the excitation and received signal. The excitation signal then inevitatbly feeds through the receiver coil and contaminates the recevied signal at the fundamental frequency. The contamination is unfortunately more than 10 million times stronger than the particle signal. Therefore, we need to apply intense hardware and software filtering to remove the fundamental frequency entirely to prevent the contamination to saturate the dynamic range of the A/D converter. The loss of the fundamental frequency breaks the LSI of the MPI system, and the artifact this filtering introduces has not been previously investigated. We speculate that one motivation for the Philips group to treat MPI as a nonlinear black-box and develop the "system functions" method is that they believed the lost signal was unrecoverable. The feasibility of x-space theory to treat MPI as a LSI system then hinges upon the understanding of the nature of this lost fundamental signal and ability to recover it.

Chapter 1 describes this challenge, and analyzes the image contribution from each harmonic, and concludes that the signal loss due to filtering of direct feedthrough is only a DC offset in the image. I propose a simple continuity algorithm to completely recover the lost image content. I also provide a theoretical and experimental demonstration of the efficacy of the solution in detail, and I prove that with this simple DC recovery algorithm, we can restore the linearity and shift-invariance of MPI, a crucial characteristic for quantitative imaging.

Chapter 2 expands on Chapter 1, and unifies the two existing MPI imaging theory: the "system functions" method and the "x-space" method. It turns out that the x-space harmonic image basis set I developed in Chapter 1, which is meant to investigate image contribution from each harmonic frequencies, has a much further implication than intended. Using this basis set, I found out that a simple Chebyshev transform connects the image (x-space) domain and the temporal frequency domain, and the x-space method and the theoretical form of the system functions method are indeed two sides of the same coin.

As we restored the LSI property of MPI, it enabled us to use MPI to image blood vessels diseases or cell tracking *in vivo*. However, one limiting factor of MPI's adoption clinically would be its inadequate resolution. Previously, MPI has achieved 2-3 mm resolution with a high gradient field strength (3.5 T/m). This resolution is less than ideal for many applications needing to resolve fine structures, like capillaries or small organ structures. Additionally, MPI resolution is anisotropic and is highly dependent of the scanning parameters. Moreover, MPI's PSF drops off as slowly as 1/Gr, which introduces a lot of background haze that compromises resolution as well as image contrast. I decided to break this resolution challenge down into two steps: first, to address the physics of the anisotropy and arrive at a solution to reshape the PSF into isotropic; and second, to address the haze problem, to understand and achieve the best achievable resolution given a scanner and tracer.

Chapter 3 details the physical investigation of the source of anisotropy in MPI and proposes a multichannel method to restore isotropic resolution. I generalize a tensor imaging theory for multidimensional x-space MPI to explore the physical source of this anisotropy, present a multichannel scanning trajectory to remove anisotropy, and design and construct two orthogonal excitation and receiver coils to enable isotropic resolution. The resolution improvement is experimentally verified.

Chapter 4 analyzes the physical origin of the haze and talks about the rationale of generating an equalization filter in k-space, and how the equalization filter would dehaze the image and improve both resolution and contrast, without any noise amplification. Experimentally, I've shown that together with multichannel acquisition, equalization filter dramatially increase image quality and enable the first quantitative measurements of lumen area in a sub-millimeter diameter blood vessel phantom.

Chapter 1

Linearity and Shift Invariance for Quantitative Magnetic Particle Imaging

Linearity and Shift-Invariance (LSI) are hallmarks of almost all clinically relevant imaging techniques – including ultrasound, CT, nuclear medicine, and MRI [1]. LSI systems guarantee that the image pixel intensity is *linearly* proportional to the amount of tracer located at that pixel, and that the imaging system's blur is independent of the spatial location of the input (*shift-invariance*). Therefore, LSI is a crucial and indispensable characteristic for quantification and diagnostic ultility. For example, because X-ray CT is LSI, the reconstructed CT image of tissue attenuation coefficient maps can provide reliable and quantitative lumen diameter measurements for cardiovascular diagnosis. Similarly, MRI is LSI and therefore can provide quantitative estimates of tumor volume for cancer diagnosis.

In MPI, high-pass filters designed to remove unavoidable direct feedthrough interference removes information crucial to ensuring LSI in MPI scans. In this chapter, we present a complete theoretical and experimental description of the image artifacts from filtering and conclude that this high-pass temporal filtering removes *only* a DC component of an MPI scan, which is recoverable. We then propose and validate a robust baseline recovery algorithm to completely restore the lost information for the x-space MPI method. We provide the theoretical, simulated, and experimental proof that our baseline recovery algorithm indeed restores the LSI properties of MPI system, a crucial step toward making MPI a quantitative tracer imaging modality.

1.1 MPI Overview

Magnetic Particle Imaging (MPI) detects the magnetic signature of superparamagnetic nanoparticles in a confluence of static and dynamic magnetic fields (see Fig. 1.1). The static magnetic field, or selection field, is a very strong magnetic field gradient (typically stronger than 2.5 T/m), producing a localized region where the static magnetic field is zero (known as the field-free-point or FFP) at the midpoint between the magnets. This static gradient field effectively saturates all nanoparticles outside of the FFP and provides spatial encoding in MPI. We then apply one or more homogeneous oscillating magnetic fields, called a drive or excitation field, to measure the mass of the nanoparticles within the FFP. These oscillating fields have amplitudes in the range of 10-40 mTpp, and frequency around 20 kHz, and they rapidly translate the instantaneous FFP across a small region, called the partial field of view (pFOV). When the FFP moves across a SPIO particle, it causes the magnetization of the SPIOs to saturate, inducing a voltage signal in the receive coil that is rich in harmonics of the fundamental drive frequency, and thus can be isolated from the strong fundamental frequencies using frequency-domain techniques. On top of the drive fields, the FFP is then scanned either mechanically or electronically (10-100 Hz, much slower than the drive frequency) to cover the entire imaging subject, and the harmonic response is recorded for each FFP location, to create a full 3D scan of SPIO distribution.

The basic principle of signal generation in MPI relies on the nonlinear magnetization response $M(H)$ of the ensemble superparamagnetic particles to an applied magnetic field H (see Fig. 1.2), described by the Langevin curve. When applying a single frequency sinusoidal drive field $H_s(t)$ of sufficient amplitude, the magnetization response $M(t)$ of the particles is saturated due to the intense nonlinear M-H curve, and induces a signal with rich spectrum of higher harmonics than the fundamental frequency of the drive field. Because of this temporal-frequency separation between the excitation and received signal, we can isolate the signal spectrum that is only from the particles.

Currently, there are two methods to reconstruct the MPI image from the received, high-pass filtered, MPI signal: the *system function* method [2,3] and the *x-space* method [4,5]. The *system function* method employs a large *system matrix* that describes the spatial dependence of signal harmonics from a point source input for every pixel within the imaging bore. This large matrix is estimated either by acquiring a time-consuming calibration scan of experimental impulse responses at every desired location [3] or through a full Langevin nanoparticle model simulation [2]. *System function* reconstruction typically involves inverting the *system matrix* estimate, which may require regularization to deal with poor conditioning. The matrix inversion process can be computationally intense, and if deconvolution is employed, it can amplify noise in the image [6]. Moreover, the system matrix estimate is often acquired from nanoparticles in water, which may not match the viscosity of blood, a thixotropic fluid [7]. Further, blood viscosity is known to decrease by about 35% [8] from larger vessels (0.5 mm in diameter) to capillaries (40 microns in diameter) due to the Fåhræus–Lindqvist effect. Such modeling errors could create image reconstruction artifacts in the system matrix method when applied *in vivo*.

The *x-space* method does not rely on an estimate of the system matrix, but instead reconstructs the MPI image using only the instantaneous MPI signal and FFP velocity through space. As a result, the *x-space* image reconstruction algorithm is computationally

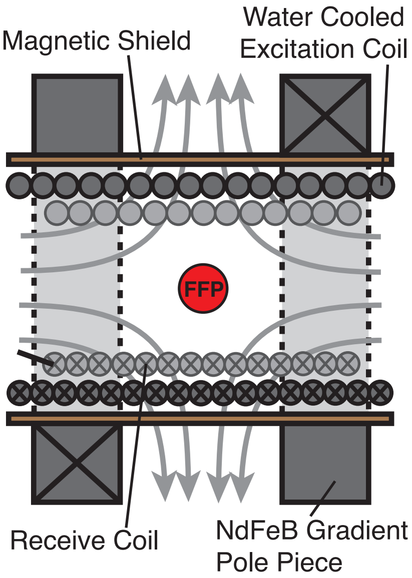

Figure 1.1: Overview of MPI instrument. The NdFeB magnet pole piece generates a strong magnetic field gradient, and produces a field free point (FFP) in the middle of the imaging bore. The excitation coil generates an oscillating field that solicitate a signal from the particles located at the FFP.

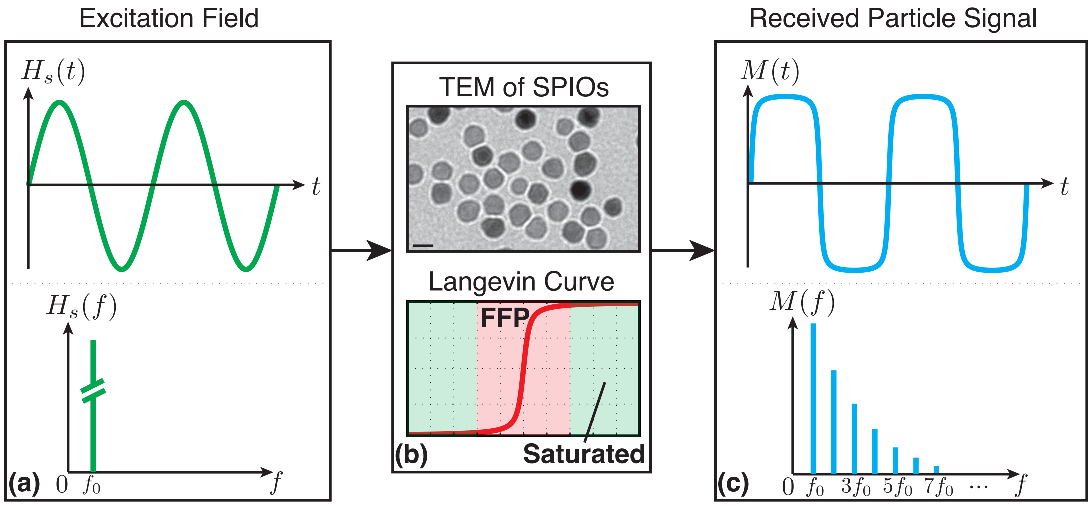

Figure 1.2: SPIO signal is rich in harmonics generated by the nonlinear magnetic saturation. (a) Excitation field is a sinusoid with a single frequency. (b) The Langevin function accurately describes the magnetization of an ensemble of magnetic nanoparticles in response to an applied magnetic field. (c) Nonlinear particle response generates a harmonic-rich particle signal.

fast and well-conditioned, and reconstructs the native undeconvolved MPI image, whose resolution is defined only by the strength of the magnetic field gradient and the magnetic properties of the nanoparticle tracer.

For the rest of this thesis, we use the *x-space* method to reconstruct all of the experimental MPI data.

1.2 Direct Feedthrough Filtering Destroys Linearity and Shift-Invariance

One crucial practical consideration in MPI is the effect of suppressing direct feedthrough interference, an unavoidable phenomenon in current MPI techniques. Because the excitation and signal reception occur simultaneously in MPI, significant direct feedthrough interference is induced in the receive coil by the excitation field at its fundamental excitation frequency (Fig. 1.3). To reject this direct feedthrough interference, nearly all MPI scanners rely on high-pass filters, which pass only higher-order harmonic frequency signals to the pre-amplifier and A/D converter. Of course, these high-pass filters also unavoidably remove the nanoparticle response's first harmonic information, which also destroys the LSI properties of MPI. The impact of the loss of first harmonic information has never been fully analyzed in MPI.

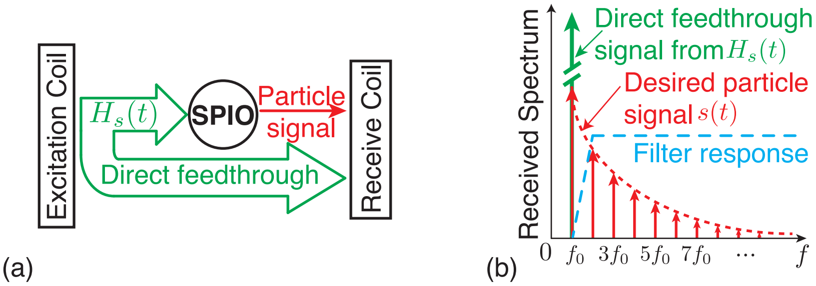

Figure 1.3: Simultaneous excitation and reception in MPI leads to direct feedthrough interference, which contaminates the received signal at the fundamental drive frequency. Aggressive filtering removes the direct feedthrough interference, however it also removes part of the nanoparticle signal. It is necessary to recover the lost signal to enable artifact-free MPI images. (a) Simplified block diagram of the MPI system. Excitation and reception occur simultaneously. (b) Frequency spectrum of the signal detected in the receive coil. Sinusoidal excitation leads to harmonics in the nanoparticle signal spectrum. A high-pass filter is applied to remove the fundamental feedthrough signal.

The MPI x-space analysis relies on three assumptions:

1. *Uniqueness*: the instantaneous position of the FFP in the bore is unique at all times. This is always valid given the modest (e.g., 10%) homogeneity specifications of the

FFP magnet and the excitation magnets.

2. *Adiabaticity*: the nanoparticles respond adiabatically (i.e., instantaneously) to the applied magnetic field. This is not always valid, as analyzed by Weizenecker *et al.* [9], Reeves *et al.* [10], Goodwill *et al.* [11], Croft *et al.* [12], and Ferguson *et al.* [13].

3. *Complete MPI Signal Recoverability*: the x-space reconstruction requires the complete MPI signal, including the lost first harmonic information. Hence, x-space reconstruction requires that the lost first harmonic information is recoverable via robust methods.

The practical implications of the assumption that the lost first harmonic information is fully recoverable have never been analyzed. Here, we prove for the first time that the lost first harmonic information corresponds to offsets of the constant (or DC) component of the MPI image. We propose a robust algorithm to restore the lost DC information in conjunction with x-space MPI. Finally, we provide the first theory, simulation and experimental evidence that our proposed algorithm does indeed restore the LSI properties of the MPI images. This DC recovery method may also improve system function method, since the loss of DC information is common to all MPI methods.

1.3 Theory

In this section, we prove that the direct feedthrough filtering in MPI causes a loss of a constant (or DC) information in an unmodified x-space reconstruction. This insight informs the robust and fast algorithm that we propose below to restore this lost DC information.

1.3.1 1D X-space Theory: Brief Review

MPI requires a strong magnetic field gradient for spatial encoding and selectively saturating the sample at all locations except near the FFP. Applying a strong magnetic gradient $-\mu_0 G$ [T/m] across the sample, the particles within the sample experience a magnetic gradient field

$$H(x) = -Gx \tag{1.1}$$

To elicit a nanoparticle signal, we apply a spatially homogenous and temporally sinusoidal magnetic field to the sample. Without loss of generality, we model the excitation field as a 1D cosine function with peak amplitude B_{ex} [T] and frequency f_0 [Hz]

$$H_s(t) = \frac{B_{ex}}{\mu_0} \cos(2\pi f_0 t) \tag{1.2}$$

Solving $H(x)+H_s(t)=0$, we obtain the instantaneous Field Free Point (FFP), $x_s(t)$ [m]

$$x_s(t) = G^{-1}H_s(t) = \frac{W}{2}\cos\left(2\pi f_0 t\right), \tag{1.3}$$

where we have defined $W = 2B_{ex}/(\mu_0 G)$ [m]. This equation shows that the FFP trajectory sinusoidally scans across a region of width W, which we refer to as the "partial Field-of-View" (pFOV).

The particle signal is picked up by an inductive coil. The *1D MPI signal equation* in volts can be derived using the Reciprocity Theorem and the three assumptions above [4]. Assuming the receiver coil has a sensitivity map of $-B_1$ [T/A] and the input particle distribution is $\rho(x)$ [particles/m], we obtain the following convolution relation:

$$s(t) = \gamma\dot{x}_s(t)\rho\left(x\right) * \dot{\mathscr{L}}\left(Gx/H_{sat}\right)\Bigg|_{x=x_s(t)} \tag{1.4}$$

where $\gamma \triangleq B_1 m G/H_{sat}$, m [Am^2] is the magnetic moment of the magnetic nanoparticle, H_{sat} [A/m] is the amplitude of the magnetic field it takes to half saturate the nanoparticle tracer, $\dot{x}_s(t)$ [m/s] is the instantaneous FFP speed, and $\mathscr{L}$ refers to the Langevin function that characterizes SPIO magnetization.

We can analytically convert the time-domain signal equation directly into a native MPI image, $\hat{\rho}(x)$, using the x-space reconstruction method [4]. This only requires normalizing the received signal by the instantaneous velocity, followed by gridding to the instantaneous position of the FFP (Fig. 1.5):

$$\begin{aligned}\hat{\rho}\left(x_s(t)\right) &= \frac{s(t)}{\gamma\dot{x}_s(t)}\\ &= \rho\left(x_s(t)\right) * \dot{\mathscr{L}}\left[Gx_s(t)/H_{sat}\right]\end{aligned} \tag{1.5}$$

Note that the x-space reconstruction only requires a single point-wise division and gridding operation, which can be performed in real time. As we described above, the noise source in MPI is currently dominated by the direct feedthrough interference, which decreases together with the FFP velocity. Thus, theoretically, dividing the signal by the velocity should not amplify the direct interfering noise. For these reasons, x-space reconstruction method is computationally efficient and well-conditioned.

The analysis above shows that the resulting MPI image is simply the nanoparticle density convolved with the native MPI point spread function (PSF), which is clearly identified as $h(x) \triangleq \dot{\mathscr{L}}\left[Gx/H_{sat}\right]$ (Fig. 1.4a-c). In the case of 2D or 3D excitation field, MPI can still be written as the multi-dimensional nanoparticle distribution convolved with a multi-dimensional PSF, as shown in Goodwill *et al.* [5]. This convolution relationship proves that MPI is a linear and shift-invariant imaging system. However, this result assumes that the *complete* MPI signal is available for reconstruction into a LSI image. In contrast, the first harmonic information is unavailable in practice due to the direct feedthrough high-pass filtering operation. We now analyze this challenge.

1.3.2 MPI Harmonic Image Basis Set

To understand how filtering affects the MPI image, it is powerful to assess the individual contribution each temporal harmonic signal makes to an MPI image. Building on insightful results from Rahmer *et al.* [2] on the harmonic decomposition of unfiltered particle signals, we apply here for the first time the x-space reconstruction algorithm to each harmonic, and we prove that filtering out the first harmonic information corresponds to losing a constant, or DC, component of the MPI image.

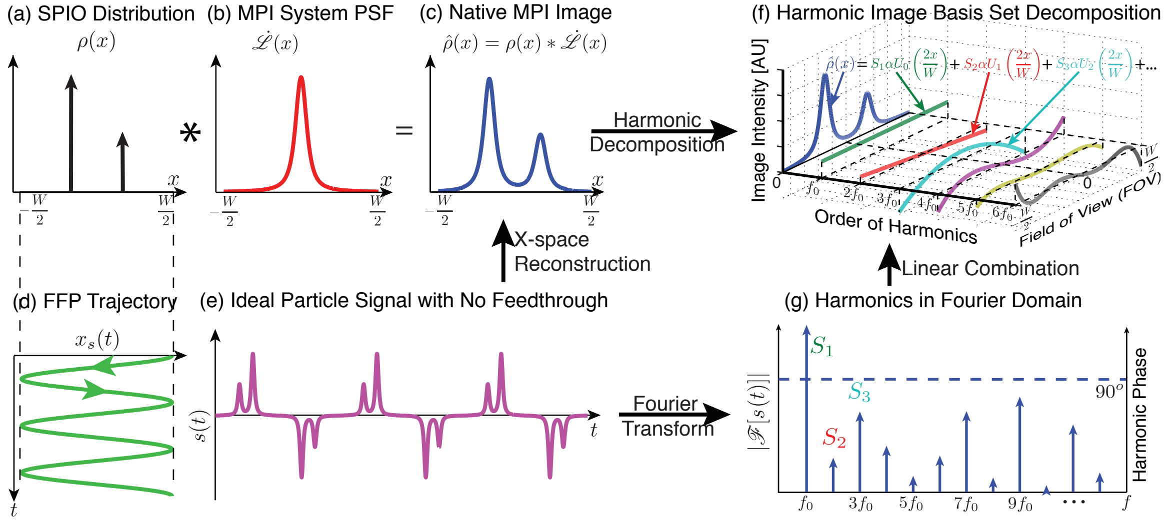

Figure 1.4: Illustration of 1D MPI imaging process, x-space reconstruction and harmonic decomposition of the MPI signal in the time and image domains. (a)-(c) MPI is intrinsically LSI – the native image can be written as a convolution of the input SPIO distribution and a point spread function (PSF). (d) Basic sinusoidal scanning sequence in 1D. (e) Theoretical time domain nanoparticle signal assuming no direct feedthrough. (f) Application of the x-space reconstruction to each harmonic signal expands the native image into the MPI harmonic image basis set, which is composed of Chebyshev polynomials of the second kind. (g) The Fourier representation of the time domain signal. Note that the phase is 90° across all the harmonics from the inductive detector.

We begin with Fourier analysis of the received particle signal $s(t)$. For periodic cosinusoidal excitation expressed in Eqn. 1.2, the received signal is composed of a series of sinusoidal harmonics of the excitation. Rahmer *et al.* decomposed the received particle signal into a Fourier Series [2]:

$$s(t) = \sum_{n=1}^{\infty} S_n \sin\left(2n\pi f_0 t\right) \tag{1.6}$$

where S_n is the Fourier coefficients of the n^{th} order harmonic signal.

We now apply the x-space reconstruction method to both sides of Eqn. 1.6 to derive an analytic decomposition of the MPI image. Because the x-space reconstruction is a *linear* operation, we can apply it to each term in the series and thereby isolate the spatial contribution from each harmonic. From the FFP trajectory in Eqn. 1.3, we can make the substitutions $\dot{x}_s(t) = -\pi f_0 W \sin(2\pi f_0 t)$ and $2\pi f_0 t = \arccos(2x/W)$ to obtain:

$$\begin{aligned}
\hat{\rho}(x) &= \left.\frac{s(t)}{\gamma \dot{x}_s(t)}\right|_{t=1/(2\pi f_0)\arccos(2x/W)} \\
&= \alpha \sum_{n=1}^{\infty} S_n \left.\frac{\sin(2n\pi f_0 t)}{\sin(2\pi f_0 t)}\right|_{t=1/(2\pi f_0)\arccos(2x/W)} \\
&= \alpha \sum_{n=1}^{\infty} S_n \frac{\sin(n \arccos(2x/W))}{\sin(\arccos(2x/W))} \\
&= \alpha \sum_{n=1}^{\infty} S_n U_{n-1}\left(\frac{2x}{W}\right) \qquad (1.7)
\end{aligned}$$

where α is a constant that only depends on the scanning parameters and particle properties, with the analytical form $\alpha \triangleq \frac{-H_{sat}}{B_1 m G \pi f_0 W}$. Hence, the n^{th} harmonic signal corresponds to a weighted version of a simple Chebyshev polynomial of the second kind, $U_{n-1}(x)$. In fact, this result implies that the set of Chebyshev polynomials constitutes a complete and natural *MPI harmonic image basis set* [2]. Therefore, Eqn. 8 motivates a straightforward analysis of the lost harmonic signals due to temporal filtering.

For reference, the first five Chebyshev polynomials are listed in Table 1.1. Most pertinent to this paper, the first harmonic basis image is simply a constant in space. The second harmonic reconstructs to a linear slope in space, and the third harmonic corresponds to the quadratic basis function in space. Figure 1.4 illustrates an example of decomposing an MPI native image from a simple nanoparticle distribution onto the MPI harmonic image basis set. This image decomposition highlights the fundamental transform in MPI between image space and harmonic space, and it allows a thorough analysis of the spatial frequency contents of all MPI harmonics.

Harmonic	MPI harmonic image basis set	Shape
$\sin(1\omega_0 t)$	1	constant
$\sin(2\omega_0 t)$	$2x$	linear slope
$\sin(3\omega_0 t)$	$4x^2 - 1$	parabola
$\sin(4\omega_0 t)$	$8x^3 - 4x$	cubic
$\sin(5\omega_0 t)$	$16x^4 - 12x^2 + 1$	quartic
$\vdots$	$\vdots$	$\vdots$

Table 1.1: Relationship between the time domain harmonic signal and the MPI harmonic image basis set.

1.3.3 Loss of Image Baseline and Shift Variance due to High Pass Filtering

Equation 1.7 provides deep and definitive insight into the precise *spatial* information lost due to filtering out the first *temporal* harmonic signal in MPI. Mathematically, the high-pass filter removes the first harmonic, which removes a constant from our image:

$$\hat{\rho}_{lost}(x) = \alpha S_1 U_0(2x/W) = \alpha S_1 \tag{1.8}$$

This artifact is confirmed in Figure 1.5, where we see that filtering out the fundamental frequency component of MPI signal indeed leads to a loss of a constant in the image. All the rest of odd harmonics (third, fifth, etc.) *also* contain DC content for the MPI image so *we conclude that losing the first harmonic information is precisely equivalent to having an* unknown *constant or DC offset in the uncompensated x-space MPI image.* This insight will inform our first harmonic recovery algorithm below.

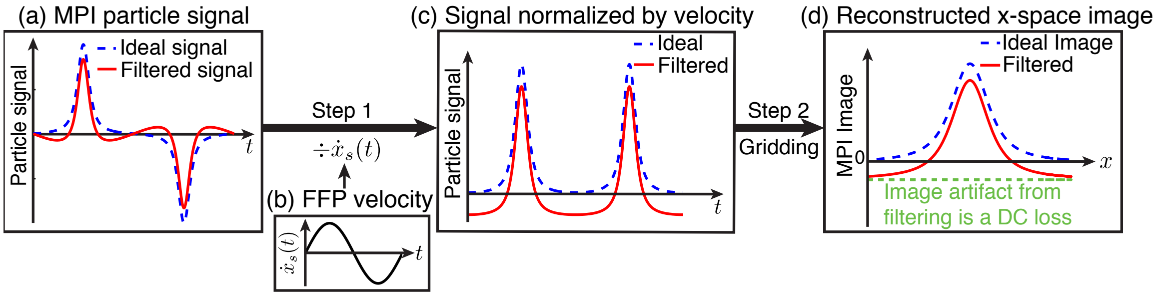

Figure 1.5: Filtering out the fundamental frequency component of the particle signal leads to a constant offset artifact in the MPI image. (a), (c), and (d) show the two-step x-space reconstruction from signal in time domain to MPI image in spatial domain. (b) A plot of the FFP velocity.

A crucial question is whether this loss of a constant value due to high-pass filtering destroys linearity or shift invariance. It is straightforward to prove that linearity is *not* destroyed by the loss of DC information, since each of the higher order S_n remains linear in $\hat{\rho}(x)$.

However, the loss of the first harmonic does destroy the shift-invariance of an uncompensated x-space image reconstruction. To see this, note that the first harmonic image (and in fact *every individual* harmonic image) is *shift variant.* For example, consider the lost first harmonic term, S_1, adapted from [2]:

$$S_1 = \beta \int_{-\frac{W}{2}}^{\frac{W}{2}} \hat{\rho}(x) \sqrt{1 - \left(\frac{2x}{W}\right)^2}\, dx \tag{1.9}$$

Here, $\beta = -4B_1 m G f_0 / H_{sat}$, a constant dependent on scanning parameters and particle properties. This equation reveals that S_1 varies when $\hat{\rho}(x)$ is shifted due to the space-variant velocity term, $\sqrt{1-(2x/W)^2}$, which is unity at $x = 0$, but it is zero at the edges of the pFOV, $x = \pm W/2$. This implies that a simple shift of the input image would alter the DC value of an MPI image reconstructed by x-space image reconstruction without the first harmonic information, in clear violation of LSI systems properties.

The fact that the DC loss leads to non-LSI properties is confirmed by simulation and experiments. We simulated shifting a simple impulse input in a single FOV, and observed a significantly different DC loss in the image (Fig. 1.6). Moreover, this artifact becomes far more complex *and* non-linear in a partial-FOV image reconstruction. As illustrated both in experiments and simulation (see Figs. 1.7 and 1.8), if we do not recover the lost DC information, our image reconstruction is not quantitative. Hence it is absolutely critical that this artifact be removed.

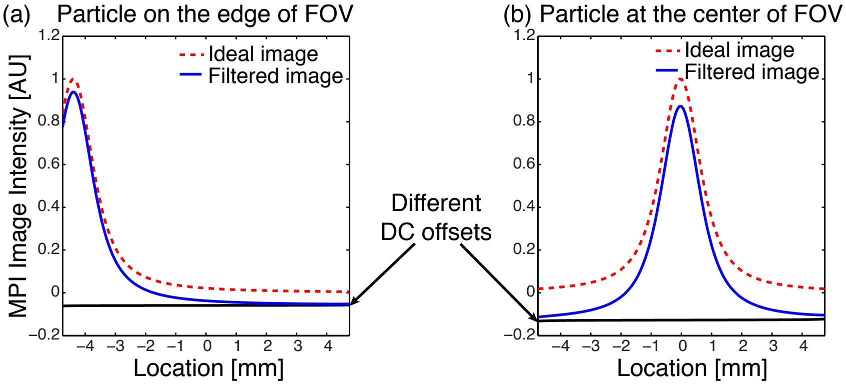

Figure 1.6: The DC offset lost due to filtering changes when the impulse input of particle distribution is shifted within the FOV, demonstrating that MPI is non-LSI after filtering. The simulated image of an impulse of particles located (a) toward the edge of the FOV, and (b) at the center of the FOV.

An apparent paradox arises: how can x-space reconstruction using all the harmonic signals be shift *invariant* while each harmonic image is shift *variant*? This paradox is resolved by the fact that the sum of *all* the harmonic basis images (including the unavailable first harmonic term) does indeed cancel the shift-variant velocity weighting term, revealing a linear and shift-invariant MPI image (see Appendix A for a rigorous proof). This reassures that the x-space theory remains valid, and it indicates that one should be able to restore LSI properties by simply restoring the lost first harmonic image.

Since there is no practical way to filter out direct feedthrough without also rejecting the first harmonic MPI signal, we must instead devise an algorithm to restore the lost DC information using *a priori* information. It is fortunate that the image artifacts from filtering are restricted to the DC components of the MPI image, since there exist many robust signal processing methods to restore baseline or DC components of an image using *continuity algorithms*. In Section 1.4 we present a fast and robust continuity algorithm that recovers the lost DC offset and thereby restores the quantitative LSI properties of the x-space MPI technique.

1.3.4 Partial Field of View MPI Scanning and Lost Baseline Information

Clinical MPI must obey human safety limits on SAR and magnetostimulation [14,15]. Within the typical operation frequency range of MPI, magnetostimulation has been shown to be the dominant safety concern [16]. For example, if we are to image a torso ($r =$ 20 cm) using a full body MPI scanner with 5 T/m gradient, it would require a 1 Tpp excitation field strength to cover the entire sample. However, magnetostimulation limits excitation field amplitudes of $\approx$ 8 mTpp at 25 kHz [16] to avoid stimulating the human subjects, which would only cover a partial field of view (pFOV) of about 3 mm. To address this magnetostimulation challenge while covering a large FOV, the Philips group introduced the 'focus field' approach [17–19], where they rapidly scan small sub-regions and slowly translate the center of the sub-region to cover the entire FOV. Each sub-region (or 'station') is reconstructed individually by system matrix inversion. The full FOV is then reconstructed by averaging the sub-regions together. Here we also address the magnetostimulation safety limit with a similar pFOV scanning scheme, but we instead use a modified x-space image reconstruction algorithm.

We now understand that high-pass filtering distorts only the global DC value. This situation is more complex for pFOV scanning. Figures 1.7 and 1.8 shows the pFOV scan data from both experiments and simulation. We can see that the high-pass filter shifts *each* pFOV by an unknown DC offset that we will denote by δ_i. If we fail to correct the DC offsets, it is apparent that the naively reconstructed MPI image is highly distorted and non-quantitative (for an example of a unrecovered image, see the experimental data in Fig. 1.8). To restore the desired native MPI image, we must estimate each of the δ_i robustly and then fully recover the desired MPI image over the entire FOV. This method is described below.

1.4 Continuity Algorithm to Restore Lost Baseline Information and LSI Properties in MPI

Consider a single MPI scan reconstructed with the x-space method from the high-pass MPI signal with no first harmonic information. This image will manifest the correct slope, quadratic term, and higher-order terms, but it will have an incorrect DC value. Fortunately, we know that the MPI image should be zero outside the FOV where no particles exist, so it is straightforward to offset the entire image so that the average value of the reconstructed image outside the FOV is zero. Essentially we are enforcing continuity

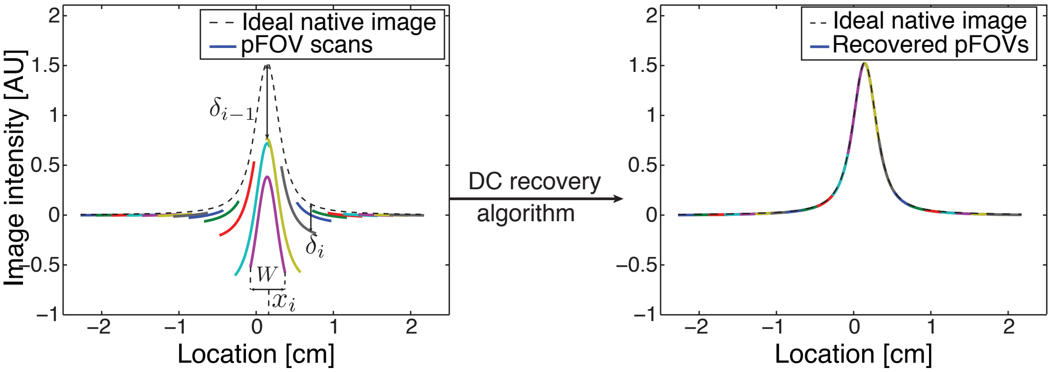

Figure 1.7: Simulation of pFOV scanning scheme and DC recovery algorithm on an impulse input (i.e., point source) of particles. Each pFOV scan loses a different DC offset δ_i as each scan sees a different particle distribution. After DC recovery, the lost DC offsets can be completely restored to each pFOV. The reconstructed image shows a perfect match with the ideal native MPI image.

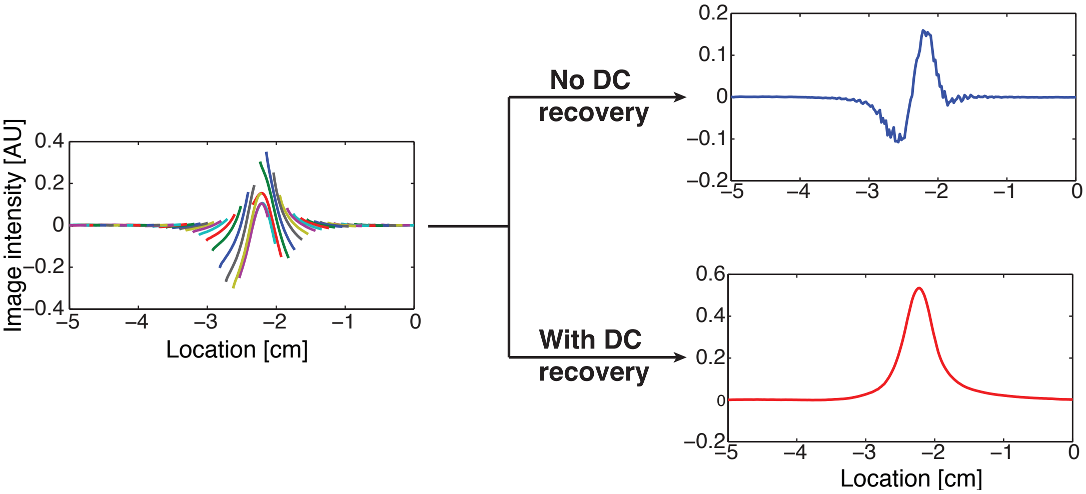

Figure 1.8: Experimental data of MPI images reconstructed without and with DC recovery. The data was acquired from an impulse input of the particles on Berkeley FFL projection scanner. The reconstructed image without DC recovery has a very different shape from the ideal image and does not have any quantitative value. In contrast, the reconstructed image with DC recovery effectively restores all the lost signal and matches well with the ideal MPI image shown in the simulation (Fig. 1.7).

to the known zero boundary condition. This *a priori* information allows us to robustly recover the lost DC information.

We can extend this continuity algorithm to pFOV scanning provided our FFP scanning trajectory satisfies two conditions:

1. Overlapping pFOVs: The pFOV scans must *have non-zero overlap* to ensure continuity of the overall full-FOV reconstruction.

2. Known boundary conditions: To have a robust recovery of the global baseline offset, we must have some *a priori* knowledge of the particle concentration at one reference location. For example, we need a location that is known to contain no tracer (such as a location outside the patient), or a fiducial with known concentration. This is akin to the FOV requirement to prevent aliasing in CT and MRI.

Figure 1.7 illustrates the operation of our DC or baseline recovery algorithm. For illustrative purposes, we will describe the algorithm working from left to right, but symmetric continuity algorithms are also feasible.

We first simply shift the leftmost pFOV sub-image so that the region outside the patient has zero average signal. Mathematically, this is identical to picking the first DC shift estimate, δ_1, as the negative of the sample mean of the leftmost pFOV.

The rest of the constant offsets can be estimated iteratively by maximizing the continuity of successive pFOV scans over the overlapping regions. Mathematically, we pick the DC shift estimates, $\hat{\delta}_i$, to be the sample mean of the difference between the successive pFOVs, where the averaging takes place only over the two regions' overlap zone.

This recovery algorithm is real-time since offsets can be directly calculated with linear computational complexity. In Appendix B, we prove that this algorithm provides statistically unbiased estimates of the real offsets, and a complete restoration of the linearity and shift invariance of MPI system. In the following sections, we demonstrate with experiments and simulation that with this modified x-space reconstruction, MPI images demonstrate linearity and shift invariance.

1.5 Methods

1.5.1 Simulations

We implemented a numerical simulation of the MPI imaging process, including magnetic field simulation, Langevin nanoparticle modeling, FFP trajectory generation, signal detection, direct feedthrough interference computation and filtering (MATLAB, Natick, MA). X-space reconstruction was implemented in the simulator to reconstruct the native MPI images. The simulated MPI signals and images were then decomposed into harmonic basis sets, and compared with the analytic forms. Specific harmonic images of interest included the first and second harmonic images.

1.5.2 Phantom Imaging

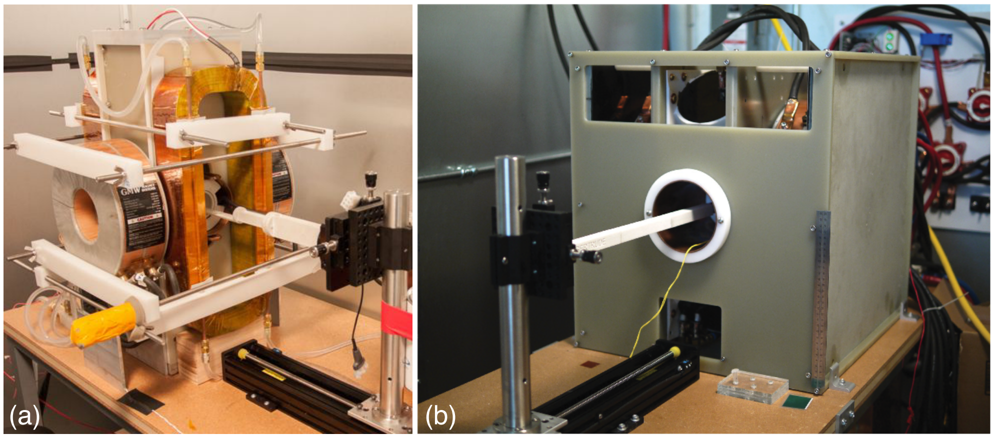

Figure 1.9: MPI scanners. (a) Berkeley FFL projection MPI scanner, with a gradient strength of 2.25 T/m along x and z axes. (b) Latest Berkeley 3D x-space MPI scanner, with a gradient strength of 7 T/m in the x axis and 3.5 T/m in y and z axes.

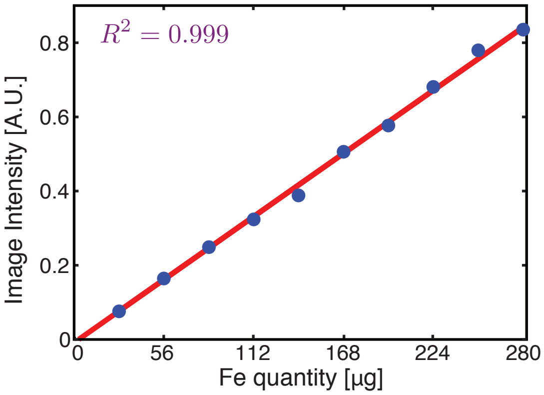

Figure 1.10: Experimental demonstration of MPI's linearity after recovery and stitching. The peak intensity of the corresponding MPI image is linearly proportional to the input particle quantity, showing a near-perfect correlation coefficient ($R^2 = 0.999$). The amount of iron tested ranges from 28 μg to 280 μg, with a step size of 28 μg. An image of 1 cm by 1 cm is taken and reconstructed for each sample, and the peak value of each impulse response is plotted.

The imaging experiments were performed on the Berkeley field free line (FFL) projection MPI scanner (Fig. 1.9(a)) [20] and 3D FFP MPI scanner (Fig. 1.9(b)). The gradient strength of FFL scanner is 2.25 T/m along x and z axes, yielding an imaging resolution of 3.9 mm in z axis and 7.6 mm in x axis with the contrast agent Resovist [20]. The 3D

FFP MPI scanner has a gradient strength of 7 T/m in the x axis, and 3.5 T/m in y and z axes, yielding an image resolution of 2.5 mm in all axes with Resovist. Both scanners excite along the z axis at 22 kHz. Along with a triangular slow-shifting magnetic field in x axis, the excitation field covers each pFOV in a Cartesian trajectory [21], while the additional slow-shifting magnetic fields in z axis (as well as y axis in the case of Berkeley 3D FFP MPI scanner) slowly translate the pFOV to cover the entire imaging sample [5].

To test the linearity of the system, we acquired a series of images on the Berkeley FFL scanner, each containing a single point source tracer with iron quantity ranging from 28 μg to 280 μg Fe, with a step size of 28 μg for a total of 10 measurements. An image of 1 cm by 1 cm is taken and reconstructed for each sample, and we measure the peak image intensity of each impulse response.

To test linearity and shift invariance simultaneously, we constructed an acrylic phantom containing multiple line sources of different concentrations (Fig. 1.11(a)) and imaged it using the FFL scanner. The phantom measures 10 cm by 2 cm and contains four laser-cut channels. Each channel has a width of 1.5 mm, a thickness of 3 mm and a length of 1 cm. The channels are spaced at 3 cm intervals and filled with exponentially decreasing concentrations of Resovist tracer: 50, 25, 12.5 and 6.25 millimoles Fe/L. The phantom was imaged with a 2D FOV of 6 cm × 12 cm in the horizontal xz imaging plane, with a scan time of 39 seconds. The FFL scanner has a pFOV of about 6 cm × 2.5 cm. The total scan was completed with a pFOV overlap ratio of 75%.

We also constructed two laser-cut acrylic "carotid artery" phantoms imitating two models of carotid arteries with and without a stenosis model (Fig. 1.12a). We scanned this phantom on a 3D FFP MPI scanner. The channel representing the common carotid artery is 4.5 mm wide, and the branching channels representing the external and internal carotid arteries have a width of 3 mm. Both are approximately 75% the size of a typical human carotid artery. In one of the phantoms, we created a stenosis where the internal carotid artery is half occluded. The phantom is filled with 20-fold diluted Resovist at 25 millimoles Fe/L concentration. The phantom was imaged with a full 3D FOV at a spatial coverage of 4.5 cm × 4.5 cm × 6.2 cm, and a scan time of 141 seconds. The pFOV size was around 4.5 cm × 4.5 cm × 1.3 cm. The overlap ratio between two successive pFOVs was 80%.

1.5.3 X-space Reconstruction and Recovery Algorithm Implementation

The received particle signals of the imaging phantoms are reconstructed using the two-step x-space reconstruction algorithm [4, 22]: the signal is first velocity compensated and then gridded to the instantaneous FFP position to form the MPI image of each pFOV scans. Due to relaxation effects and other non-interference noise sources in MPI scanners, the particle signal is non-zero at the edges of the pFOVs, where the FFP velocity is zero. To avoid the noise amplification at the two edges, we only reconstruct the central 95% of each pFOV. Experimentally, the data loss and the noise gain are negligible with a small amount of edge pFOV discarded.

The baseline or DC recovery continuity enforcement algorithm was implemented as described in Section 1.4 using MATLAB (Mathworks, Natick, MA). The computational time required for complete DC baseline recovery was minimal, on the order of milliseconds per line-scan using standard computing hardware (2x Intel Xeon E5645 CPUs, each with 6 cores, 2.4 GHz, 144 GB RAM, 64-bit Windows Server 2008 R2). Finally, we averaged the DC recovered pFOV scans to assemble a final MPI image.

1.6 Results

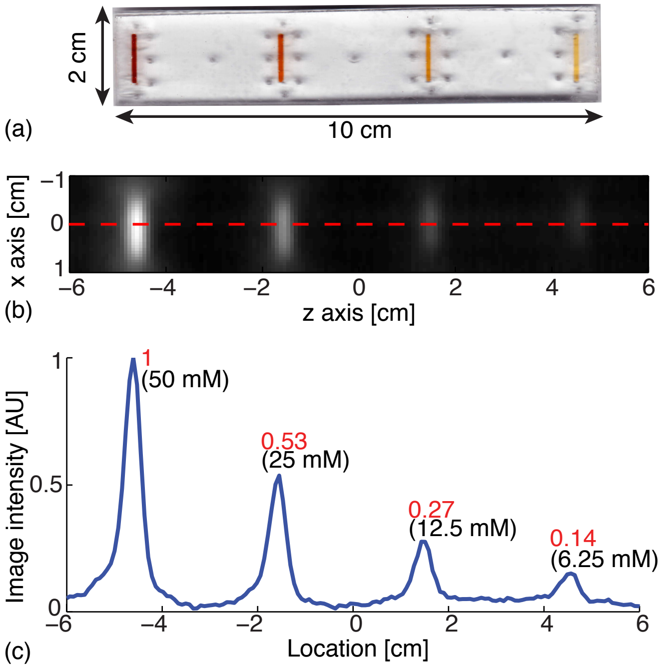

Figure 1.11: Experimental demonstration of MPI's linearity and shift invariance after recovery and stitching. (a) Linearity and shift invariance phantom. The phantom is injected with diluted Resovist, with iron concentration of 50, 25, 12.5, and 6.25 millimoles Fe/L in each channel from left to right respectively. (b) The undeconvolved native image is reconstructed after recovery and stitching. (c) The center line of the reconstructed image shows that the signal intensity is linearly proportional to the particle concentration, and the PSF shape and resolution is the same regardless of location.

Figure 1.10 shows the results of the linearity test. As demonstrated in this figure, MPI image is linear with respect to iron quantity with a near-perfect correlation coefficient ($R^2 = 0.999$) after we recover the DC offsets and stitch the pFOVs. The detection limit depends on the tracer type and has considerable room for improvement as we improve the system sensitivity and address interference sources in our system.

Figure 1.11 shows the result of the linearity and shift-invariance phantom. The reconstructed image following baseline recovery faithfully reflects the exponentially decreasing iron concentration within the channels. The center line of the reconstructed image shows that the signal intensity is linearly proportional to the particle concentration, and the PSF is the same regardless of location, verifying the linearity and shift invariance of the system.

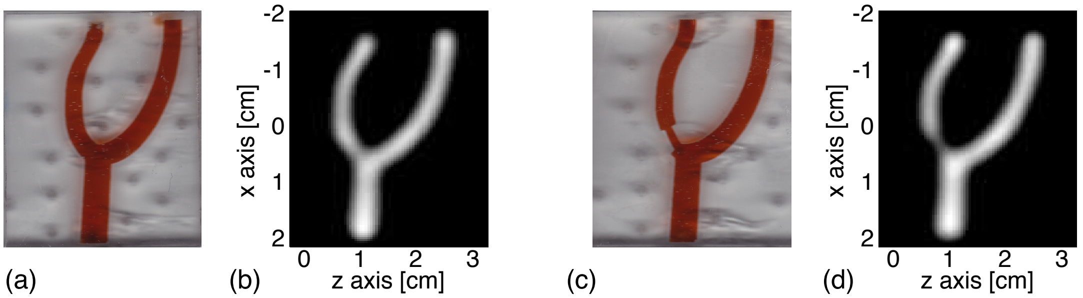

Figure 1.12: MPI shows promise as a quantitative angiographic imaging modality. (a,c) The carotid artery phantom is filled with 20x diluted Resovist (25 millimoles Fe/L). The phantoms represent the internal carotid artery with (a) no occlusion and (c) half occlusion. (b,d) Reconstructed native MPI images with baseline recovery, followed by mild Wiener deconvolution with a simulated 2D PSF, and displayed at 10% leveling. The occlusion in the phantom is very well captured in the MPI images in (d).

Figure 1.12 shows the carotid angiographic phantoms, and the reconstructed MPI images with baseline recovery and mild Wiener deconvolution. The occlusion in the vessel is clearly depicted by the reduced brightness, as well as the narrowing. These images are quantitative as the baseline recovery algorithm ensures the linearity and shift invariance of MPI system. This experiment demonstrates the tremendous potential of MPI for angiographic imaging.

1.7 Discussion

1.7.1 Tradeoffs Between Speed and Absolute Quantitation in MPI

Linearity and shift invariance (LSI) are crucial properties for quantitative imaging. In fact, almost all existing medical imaging modalities are modeled as LSI systems, including Ultrasound, CT, PET/SPECT and MRI. *Linearity* in MPI means that each pixel value is linearly related to the true nanoparticle concentration at that pixel. *Shift-invariance* means the MPI scanning process blurs the image of the nanoparticle concentration identically at every location in the image. Applications of quantitative MPI could include tracking and quantitating stem cells, or inflammation. As human MPI systems are developed, LSI qualities will also be crucial for clinicians to make quantitative diagnoses, such as ejection fraction, lumen diameter, and tumor volume.

In this paper, we both mathematically proved and experimentally demonstrated that MPI is linear and shift invariant, but only after the DC restoration algorithm recovers the lost first-harmonic image information. The modified x-space image reconstruction requires overlapping pFOVs, and full coverage of the entire FOV. These conditions enable a fast, robust algorithm to restore the lost DC information in real-time without inverting a large system matrix. Other imaging modalities also require boundary conditions. For example, MRI pulse sequence designers must choose the minimum number of phase encodes based on the FOV size to prevent spatial aliasing. In MPI, we need these conditions to ensure an absolutely quantitative and linear, shift-invariant MPI scan.

It is likely that clinicians will prefer speed over absolute quantification for certain clinical applications. For example, for cardiac imaging or coronary artery imaging, scanning speed is crucial because of the speed of cardiac motion. Also, the heart itself spans only a small fraction of the full patient FOV. Acquiring all the pFOVs out to the edge of the chest would require far more scan time than simply covering the heart. Clearly, full FOV acquisition may not be prudent for such clinical applications. Hence, one could modify the proposed method by finding a region near the heart (e.g., pericardiac fat) containing no contrast agent and use this region to provide the zero boundary condition. This would also still permit true quantitative and LSI imaging. Indeed, physicians may abandon *absolute* quantification for *relative* quantitation when imaging speed is paramount. Suppose we quickly scan only a small FOV over the heart at high speed. Then one could reconstruct a continuous image between pFOVs, using the continuity algorithm demonstrated here. As a result, the entire image would have an arbitrary DC baseline; but physicians may obviate this artifact with routine tools like window and level adjustment.

The second requirement, overlapping pFOVs, is somewhat similar to the requirement of adequate sampling to prevent spatial aliasing in CT, PET or MRI. We have found that, in practice, about 15% overlap is required during the scan (results not shown). Of course, this implies a small loss of overall imaging speed. Note that increasing the overlap region size can boost SNR, since we average independent noise sources across the overlapping regions. Our experimental pulse sequences on the latest 3D MPI scanner in Fig. 1.10(a) demonstrate that even with a 80% overlap, we can still achieve a reasonable scan time of 141 seconds at a 3D volumetric coverage of 4.5 cm × 4.5 cm × 6.2 cm. Clearly, optimizing the overlap region between pFOVs will require a delicate tradeoff between SNR, scan time, and motion artifacts. Hence, the optimal overlap region is likely to depend on the particular clinical application.

1.7.2 Parallels Between the System Function Method and X-space Image Reconstruction Methods

This analysis is the first time that the mathematical tools of x-space reconstruction have been applied to the Fourier decomposition that inspired Philips' excellent System Function method [2]. This effort could begin the unification of the two MPI image reconstruction methods. There remain significant differences between the complexity, speed and robustness of the two methods. We hope that these parallels will help researchers compare tradeoffs between the two dominant image reconstruction methods currently used in MPI.

Indeed, in theory, an MPI image could be reconstructed by summing the S_n-weighted Chebyshev-basis images in Eqn. 2.4, as proposed first by Rahmer *et al.* [2]. This image reconstruction method would be slightly slower than x-space reconstruction method (only due to the FFT operation), but faster than the system matrix inversion method. Of course, this reconstruction method and system function reconstruction method both fundamentally lack the first harmonic data, since high-pass filtering is essential for all MPI methods. Hence, we recommend applying a continuity algorithm to restore the lost DC offset information for both methods. Indeed, the successful demonstration of reconstruction using Chebyshev basis set would be a welcomed advancement to the field.

This analysis also confirms the Rayleigh limit of spatial resolution in MPI, given by Rahmer *et al.* [2] and Goodwill *et al.* [4]. One might hope that an infinite number of Fourier harmonic coefficients could enable reconstruction of an MPI image at arbitrarily high spatial resolution. However, this analysis confirms that even with an *infinite* number of Fourier coefficients, one can only perfectly reconstruct an MPI image that has already been blurred by the derivative of the Langevin function, $\hat{\rho}(x) \triangleq \rho(x) * \dot{\mathscr{L}}\,(Gx/H_{sat})$, as shown by Eqn. 1.5. Exceeding this spatial resolution defined by the nanoparticle's Langevin function and the applied gradient field then must rely on some form of deconvolution.

1.7.3 Higher Harmonic Restoration

Here we focused exclusively on the loss of first harmonic information due to the high-pass filter. However, the high-pass filter may not be sharp enough to leave the 2nd, or even 3rd, harmonic information intact. It is straightforward to extend the analysis above to include 2nd or 3rd harmonic restoration, which is precisely equivalent to restoring the linear or quadratic terms of our reconstructed MPI scans. Fortunately, low spatial frequency information can be robustly recovered provided there is adequate SNR and adequate overlap. While our current high-pass filter only removes the first harmonic, this may be an area of fruitful future investigation.

1.7.4 Extension to MPI Fluoroscopy

To date, the Fourier analysis of MPI, whether employed for x-space or system function methods, always assumes a periodic time domain received signal. This implies a discrete Fourier spectrum. Physically, this is only true when we repeat the scan of the same y-line in image space several times. However, the only clinically pertinent reason to scan the same line repeatedly is to increase SNR through averaging. We expect that future MPI scanners will scan faster, perhaps even a single period per y-line, with no repetition. At that point our received spectrum can no longer be modeled as a discrete spectrum. Fortunately, we believe that the modified x-space image reconstruction presented here will remain effective and robust, since it does not directly rely on the Fourier coefficients.

1.8 Conclusions

All MPI scanners employ high-pass filters to prevent direct feedthrough of the first harmonic from the transmit coil to the receiver coil, which could easily drown the received MPI signal. For a simple case of 1D sinusoidal excitation, we showed in theory, simulation, and in experiment that this high-pass temporal filtering removes *only* a DC component of an MPI scan. If left uncorrected, this loss of information destroys the shift invariance of x-space MPI images and also produces severe image artifacts. We showed both theoretically and experimentally that our proposed continuity algorithm restores the lost DC offsets accurately. We also showed that this restores linearity and shift invariance in x-space MPI. Last, we demonstrated the experimental MPI scans reconstructed with this modified x-space algorithm and measured near-perfect linearity and shift invariance with respect to the concentrations of SPIO contrast agent. This effort represents a crucial step toward making MPI a quantitative tracer imaging modality.

Chapter 2

Unification of X-space and System Function Views of MPI

As we mentioned in Chapter 1, there are two dominant worldviews of interpreting MPI signals and reconstructing MPI images: the *system function* method and the *x-space* method. The *system function* method was first proposed by Philips back in 2005 [23], where they establish the relationship between the frequency response signature of the magnetic particles to the spatial location of the tracer, and they reconstruct the particle distribution from the received harmonic spectrum. The *x-space* method was introduced later by Goodwill et al in 2009 [4] from our lab, where it took a linear systems approach to analyze the MPI imaging principle, and establishes a straightforward conversion from the temporal signal to the spatial distribution of the magnetic tracer.

There remain significant differences between the complexity, speed and robustness of these two methods. Therefore, for a long time, researchers in this community had viewed these two methods independently. There has been no unifying theory that bridges these two worldviews and make connections between the three domains of the MPI signal: the temporal domain, temporal frequency domain, and spatial imaging domain.

Almost all of the other mature medical imaging techniques have a well-established imaging theory that can easily transforms the signal across different domains. For example, in MRI, one can easily translate the temporal FID (free induction decay) signal into k-space, and with a simple Fourier transform, we can get the MRI image in real space. The flexibility to look at MRI signal in both the sampling domain and the final image domain is that we can analyze different MRI pulse sequences to assess k-space coverage, eddy current artifact, etc.

Similarly, in MPI, we would also like to have a unifying theory that can provide the researchers a way to connect the MPI signals in different domains. This would tremendously help to translate the previous works done with one method to implications for the other method, and help to foster communication and developement of the entire field regardless of what MPI approach to take.

In this chapter, we unify the two worldviews through the use of the MPI harmonic image basis set discovered in Chapter 1. We establish that the transform that connects the temporal frequency domain and x-space domain is a pair of Chebyshev transforms.

2.1 Review of System Function Method

Different particle distributions yield signals with different signature harmonic spectrums. For example, if we move an impulse particle distribution throughout the FOV, the harmonic spectrum changes with the input location, and is independent of each other. These impulse signature spectra thus form a basis set for decomposing any measured signal spectrum from a given particle distribution, and the decomposing coefficients reflect the amount of particle concentration at each input location. The system function method seeks to understand this spatial dependence of each harmonic from an impulse input, to construct a basis set matrix from the harmonic-spatial depencence, and to reconstruct the particle distribution from any given harmonic spectrum by matrix inversion.

Here we present a brief description of the system function theory adapted from [2]. With a harmonic drive field $H_s\left(t\right)$, the nth harmonic has the following dependence on particle position x:

$$S_n\left(x\right) \propto U_{n-1}\left(2x/W\right)\sqrt{1-\left(2x/W\right)^2},\ n=1,2,3,... \tag{2.1}$$

where $U_n\left(x\right)$ represents Chebyshev polynomials of the second kind, and W represents the width of the partial Field of View each FFP scan covers.

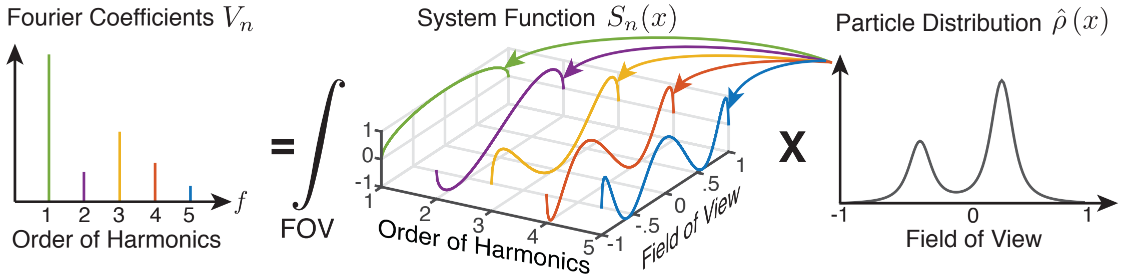

Figure 2.1: System function $S_n\left(x\right)$ is a sensitive map of the spatial dependence of each harmonic. The Fourier coefficients V_n is a sum total of the nth harmonic generated from the tracer distribution at every spatial location, weighted by the system function $S_n\left(x\right)$.

The $S_n\left(x\right)$ represents the *system function* (see Fig. 2.1), which can be seen as a sensitive map, describing the spatial sensitivity dependence of each frequency component n on particle location x.

We could measure or calculate $S_n\left(x\right)$ by measuring the magnetization response of a point-like sample at a large number of spatial positions corresponding to the number of image pixels or voxels, e.g., we could place an impulse input at a position x_0 within the

FOV and measure the particle signal in its Fourier domain. The amplitude of the harmonic frequencies gives us one sample of the system function: $S_n(x_0)$, $n = 1, 2, 3, ...$ By moving the impulse throughout the entire FOV, we can fully sample the system function matrix, $S_n(x)$, for all location x. Therefore, assuming a given particle distribution $\rho(x)$, the tracer at any particular location x_0 would contribute to the n-th harmonic by $\rho(x_0) S_n(x_0)$. The received harmonic component V_n would thus be the following integral (see Fig. 2.1):

$$V_n = \int_{FOV} S_n(x)\, \hat{\rho}(x)\, dx,\ n = 1, 2, 3, ... \tag{2.2}$$

In the equation, $\hat{\rho}(x) \triangleq \rho(x) * \dot{\mathscr{L}}(Gx/H_{sat})$, where $\dot{\mathscr{L}}(Gx/H_{sat})$ is the 1D MPI system point spread function. This equation shows that the amount of n-th harmonic from a given tracer distribution $\rho(x)$ is a summation of the amount of n-th harmonic generated by an impulse from all location x ($S_n(x)$) weighted by the blurred tracer concentration at that location $\hat{\rho}(x)$.

Reconstructing the particle concentration $\hat{\rho}(x)$ involves inverting the system matrix $S_n(x)$. Analytically, the inverse transform is equivalent to:

$$\hat{\rho}(x) \propto \frac{1}{\sqrt{1 - (2x/W)^2}} \sum_{n=1}^{\infty} V_n S_n(x) \tag{2.3}$$

As seen in the derivation, the system function method establishes the relationship between the temporal frequency domain V_n and the spatial image domain $\hat{\rho}(x)$. The system function $S_n(x)$ functions as the foward and inverse mathematical transform between the two domains.

2.2 Review of X-space Method

X-space method, on the contrary, does not require inverting a complex matrix enlisting all the signature harmonic spectrums from all the impulse responses. It establishes the direct relationship between the temporal signal to the native MPI image through gridding the temporal signal onto the corresponding spatial location instantaneously. As a result, this reconstruction method is linear, a lot faster computationally, and much better posed than system function method.

The x-space reconstruction has been introduced in Eq. 1.5, Chapter 1 (illustrated in Fig. 1.4). Here we restate the equation:

$$\hat{\rho}(x_s(t)) = \frac{s(t)}{\dot{x}_s(t)} \tag{2.4}$$

Basically, in x-space reconstruction, we normalize the received signal by instantaneous FFP velocity $\dot{x}_s(t)$, and then grid the normalized signal onto the x-space following the FFP trajectory $x_s(t)$. The x-space method establishes the relationship between the temporal signal domain $s(t)$ and the spatial image domain $\hat{\rho}(x)$. The x-space is straightfoward, and does not require one to invert an ill-posed harmonic system matrix, making the reconstruction computational fast and well-conditioned.

2.3 X-space MPI Harmonic Image Basis Set

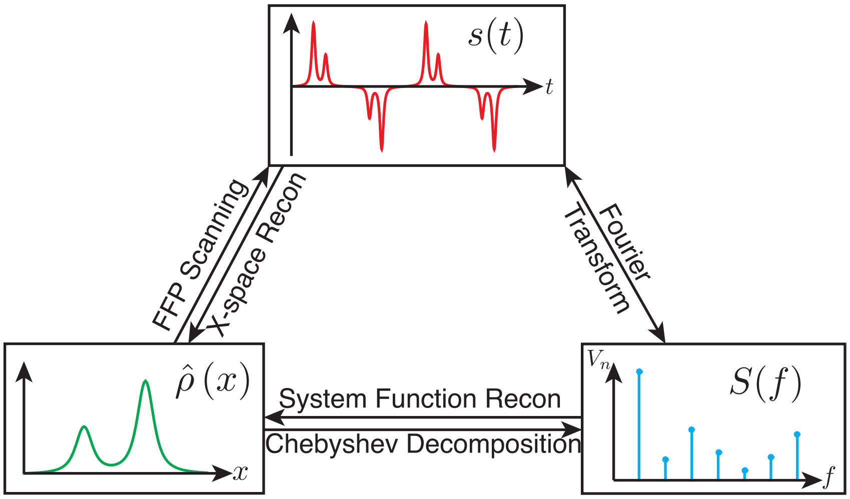

Figure 2.2: Relationships between three signal domains in MPI: temporal domain, temporal frequency domain and spatial image domain.

Though the two methods are very different in their complexity and performance, they are fundamentally unified as they compliment each other in providing information in different image domains. A combination of the understandings from both system function method and x-space method can lead to a complete chart of relationships between the three domains of interest in MPI: temporal, frequency and spatial domains. System function method relates the spatial image to the resultant temporal frequency spectrum, the x-space method relates the temporal signal domain to the spatial image domain, and in between the temporal signal domain and the temporal signal domain, Fourier transform bridges the two. As a summary, the connections between the three domains are shown in Fig. 2.2.

One way to compare and bridge the two methods is through the x-space MPI harmonic image basis set that were analyzed in the previous chapter. Since we can decompose the temporal received signal $s(t)$ into different harmonic signals, consequently, we can also decompose the spatial image $\hat{\rho}(x)$ into the harmonic images following linear approaches. To do so, we can apply x-space reconstruction on each of the harmonic frequency of the received signal $s(t)$ independently, and the resultant images form the x-space MPI harmonic image basis set, which describes the individual image contribution from each harmonic frequencies.

To recap the process, first, let us expand our temporal signal $s(t)$ into its Fourier series:

$$s(t) = \sum_{n=1}^{\infty} V_n \sin(2n\pi f_0 t) \tag{2.5}$$

where V_n is the Fourier coefficients of the nth order harmonic signal. After applying x-space reconstruction method to both sides of Eqn. 2.5, we arrive at an analytic decomposition of the MPI image:

$$\hat{\rho}(x) \propto \sum_{n=1}^{\infty} V_n U_{n-1}\left(\frac{2x}{W}\right) \tag{2.6}$$

This x-space decomposition unveils that any MPI image $\hat{\rho}(x)$ can be decomposed into a summation of Chebyshev polynomials of the second kind $U_{n-1}\left(\frac{2x}{W}\right)$ (see Fig. 2.3). Each polynomial of order n is the image contribution from the n-th harmonic frequency. As the Chebyshev polynomials are orthogonal to each other, $U_{n-1}(x)$ forms the x-space harmonic image basis set of MPI images.

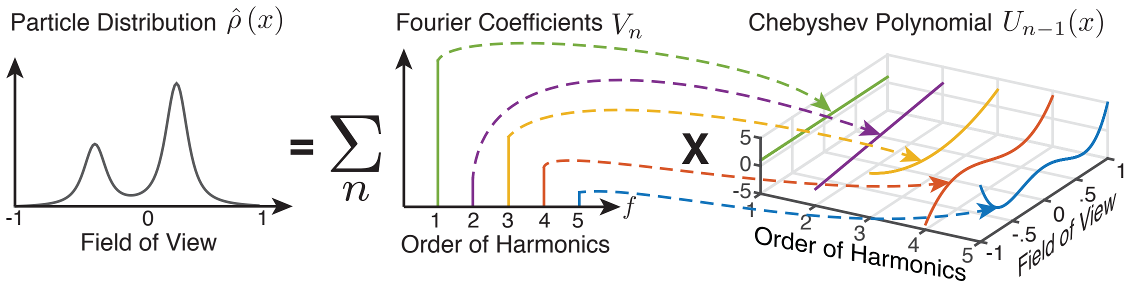

Figure 2.3: X-space MPI harmonic image basis set decomposition shows that for a tracer distribution that has a Fourier spectrum of V_n after scanning, the tracer image could be decomposed into a summation of Cheybshev polynomials of second kind (harmonic image basis set), with V_n being the coefficient of expansion onto the harmonic image basis set.

When compare the system function reconstruction in Eq. 2.3 and the x-space harmonic image basis set decomposition in Eq. 2.6, there are astounding mathematical similarities. In the next section, we will explore the unity behind the two methods.

2.4 Relationship between X-space and System Function Method

Table 2.1 compares the differences of expanding MPI image onto the system function or the x-space harmonic image basis set in the same V_n and $\rho(x)$ domains. It could be seen that in both methods, the image expansion only differs in the basis set. For system function method, the basis set is the system function $S_n(x)$, whereas, in x-space harmonic image decomposition, the basis set is the Chebyshev polynomials of second kind $U_{n-1}(x)$.

System Function	X-space MPI Image Basis Set
$V_n = \int\limits_{FOV} S_n(x)\,\hat{\rho}(x)\,dx$	$V_n = \int_0^T s(t)\,e^{-in\omega_0 t}dt$
$\hat{\rho}(x) = \frac{1}{\sqrt{1-x^2}} \sum\limits_{n=1}^{\infty} S_n(x)\,V_n$	$\hat{\rho}(x) = \sum\limits_{n=1}^{\infty} U_{n-1}(x)\,V_n$

Table 2.1: Relationship between System Function method and x-space method.

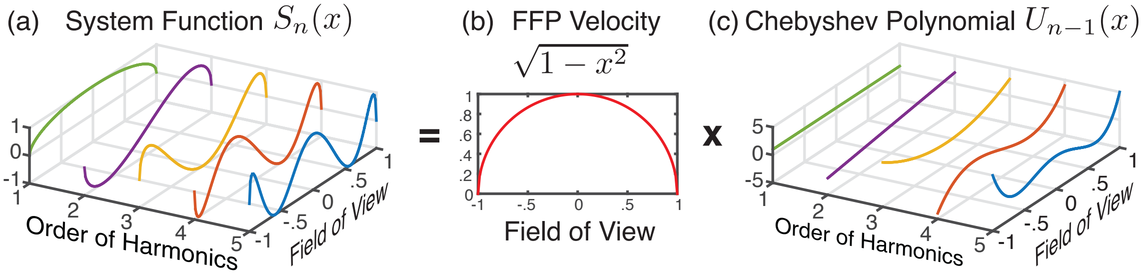

Figure 2.4: System function method and x-space method can be unified fundamentally. The system function $S_n(x)$ is essentially the x-space MPI harmonic image basis set (which is Chebyshev polynomial of second kind) $U_{n-1}(x)$ weighted by FFP velocity across the FOV.

Fig. 2.4 illustrates the relationship between $S_n(x)$ and $U_{n-1}(x)$, and we can see that

$$S_n(x) = \sqrt{1-x^2}\,U_{n-1}(x) \tag{2.7}$$

These two basis sets are related by the ratio of $\sqrt{1-x^2}$, which is essentially the shape of FFP velocity in space.

Though the two basis sets have such similar expressions, the physical meaning of each basis set is fundamentally different.

As for system function $S_n(x)$, it is a sensitive map showing each harmonic's spatial dependence on the input locations. For example, in Fig. 2.4 (a), $S_1(x)$ shows the amount of the first harmonic an impulse input would generate when moving the input within the FOV along x. Likewise, $S_2(x)$ shows how much second harmonic a point-like source generates when placed at different locations, so on and so forth. Therefore, the system function method builds a forward transform that transforms a tracer input $\rho(x)$ to the amount of harmonic V_n generated by it through Eq. 2.2.

As for x-space harmonic image basis decomposition $U_{n-1}(x)$, it shows the harmonic image shape regardless of the input tracer distribution. For example, $U_0(x) = 1$ shows that, no matter what the input is, when we sum the 1st harmonic from all of the tracer locations and reconstruct the first harmonic into image space, it yields a constant offset. Likewise, $U_1(x) = 2x$ shows that any distribution of second harmonic contributes to a slope in the image. Therefore, x-space harmonic image basis decomposition builds an inverse transform that transforms from the harmonic coefficients V_n to the reconstructed image $\hat{\rho}(x)$ through Eq. 2.6.

Analogous to the forward and inverse transform in the Fourier transform, we could see Eq. 2.2 as the forward transform, and Eq. 2.6 as the inverse transform for transforming MPI image into or from the Fourier coefficients of the time domain particle signal. It could be proven that the inversion of the system function $S_n(x)$ matrix is the Chebyhev polynomial of second kind $U_{n-1}(x)$. As it can be proven:

$$\int_{-1}^{1} U_n(x)\, S_m(x)\, dx = \int_{-1}^{1} U_n(x)\, U_m(x)\, \sqrt{1-x^2} dx = \begin{cases} 0 & : n \neq m \\ \pi/2 & : n = m \end{cases} \tag{2.8}$$

The $\sqrt{1-x^2}$ ratio term comes from the velocity term of the FFP. Intuitively, when the FFP speed is fast, the induced signal is going to be proportionally stronger due to the bigger dB/dt. The FFP scans each FOV in a sinusoudal way, which means, the FFP speed is the highest in the center of the FOV, but very slow at the edge of the FOV. Thus the induced signal (as well as harmonics) is much lower than the particle located in the center of the FOV, causing this $\sqrt{1-x^2}$ weighting. In x-space reconstruction, we compensate for the signal different due to velocity change in the FOV by normalizing the signal by $\sqrt{1-x^2}$, but in system function method, the signal is never normalized.

2.5 Conclusion

The x-space harmonic image basis set developed in Chapter 1 has further implications than understanding the different image contribution from each harmonic frequency. Using this basis set, we proved that there is a simple Chebyshev transform that connects the image (x-space) domain and the temporal frequency domain, which shows that the x-space method and the theoretical form of the system functions method are indeed two sides of the same coin.

Until today, the field of MPI is divided into two worldviews in how to interpret MPI signals and reconstruct the signal into images. Because of this difference in understanding MPI signal and image process, different groups have been developing their theory, hardware and applications separately without much mutual understanding or transfer of knowledge among the field. This chapter aims to provide a theoretical diagram of how these two worldviews can fundamentally converge as they are analyzing MPI imaging process in different domains, and only when we take both perspective can we fully understand MPI signal and images. It is also crucial for the two worldviews to converge for communication of knowledge and expertise within the field.

Chapter 3

Multi-channel Acquisition for Isotropic Resolution in Magnetic Particle Imaging

As we discussed in chapter 1, like almost all the other clinical imaging techniques, such as Computerized Tomography, Magnetic Resonance Imaging and Nuclear Medcine, MPI can be modeled as a linear and shift-invariant system with a well-defined point spread function capturing the system blur. The key difference, as we show, however, is that MPI's PSF is highly dependent on the scanning parameters, and is anisotropic using a simple linear drive field, which leads to ambiguous and inaccurate diagnosis. Therefore, anisotropic spatial resolution in MPI poses a major challenge for its clinical and preclinical adoption. In this chapter, we generalized a tensor imaging theory for multidimensional x-space MPI to explore the physical source of this anisotropy, presented a multichannel scanning trajectory to remove anisotropy, and designed and constructed two orthogonal excitation and detector coils to enable isotropic resolution. We experimentally verified the resolution improvement with the new hardware and reconstruction, and showed that isotropic resolution enabled quantitative measurement of lumen diameter with MPI.

3.1 Introduction

Magnetic particle imaging (MPI) is a promising tracer modality that has superb tracer sensitivity [24–27] that can even exceed Nuclear Medicine under dose limit [26]. MPI directly images the biodistribution of a magnetic and biocompatible tracer, superparamagnetic iron oxides (SPIOs) [28–30]. MPI images have positive contrast, unlimited depth penentation and suffer no background tissue signal. Moreover, MPI is much safer than nuclear medicine, as there is no ionizing radiation, and the magnetic tracer is biocompatible and kidney-safe [30–32]. MPI is thus ideally suited for tracer imaging, and promising for many biological and medical applications, such as safe angiography [26, 33–35], cell tracking [26], cancer detection, and inflammation imaging.

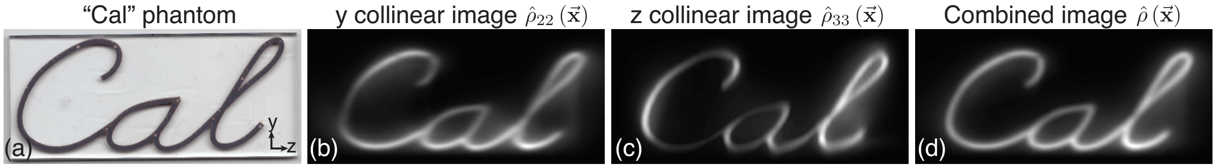
"Cal" phantom

y collinear image $\hat{\rho}_{22}(\vec{\mathbf{x}})$

z collinear image $\hat{\rho}_{33}(\vec{\mathbf{x}})$

Combined image $\hat{\rho}(\vec{\mathbf{x}})$

Figure 3.1: Combining multi-channel acquisition enables isotropic MPI native resolution. Experimental MPI imaging data acquired on a 7 T/m x 3.5 T/m x 3.5 T/m MPI scanner. (a) Photograph of a "Cal" shaped acrylic phantom injected with Micromod Nanomag-MIP particles (10.6 μg/ml). (b) Collinear scan acquired with a single y channel, showing anisotropic resolution. The horizontal haze is due to the slow signal decay perpendicular to excitation direction, and this haze blurs image and reduces its contrast. (c) Collinear scan acquired with single z channel. (d) Combining two orthogonal collinear scans from (b) and (c) achieves planar isotropic resolution.

Since the first introduction of the technique by Gleich and Weizenecker [23], there have been many significant technological advancements in instrumentation [20, 22, 36–42], particle physics [12, 43–47], imaging theory and reconstruction [2, 3, 5, 26, 48–52], safety [16, 53, 54] and developements in biomedical applications [25, 26, 33–35].

Notation	**Value**	**Size**
$\vec{\mathbf{x}}$	Spatial Location Vector	$\mathbb{R}^{n\times 1}$
$\mathbf{h}(\vec{\mathbf{x}})$	Point Spread Function	$\mathbb{R}^{n\times n}$
$h_{ij}(\vec{\mathbf{x}})$	i, j^{th}Component of $\mathbf{h}(\vec{\mathbf{x}})$	$\mathbb{R}^{1}$
$E_T(\vec{\mathbf{x}})$	Tangential Envelope (Good Resolution)	$\mathbb{R}^{1}$
$E_N(\vec{\mathbf{x}})$	Normal Envelope (Bad Resolution)	$\mathbb{R}^{1}$
$\mathbf{W}_T(\vec{\mathbf{x}})$	Tangential Weighting Matrices	$\mathbb{R}^{n\times n}$
$\mathbf{W}_N(\vec{\mathbf{x}})$	Normal Weighting Matrices	$\mathbb{R}^{n\times n}$
$\mathbf{\Omega}(\vec{\mathbf{x}})$	Multidimensional Image Tensor	$\mathbb{R}^{n\times n}$
$\hat{\rho}_{ij}(\vec{\mathbf{x}})$	i, j^{th} Component of $\mathbf{\Omega}(\vec{\mathbf{x}})$	$\mathbb{R}^{1}$
$\vec{\mathbf{u}}_a(t)$, $\vec{\mathbf{u}}_b(t)$	Excitation and detection vector	$\mathbb{R}^{n\times 1}$
$\hat{\rho}_{\vec{\mathbf{u}}_a,\vec{\mathbf{u}}_b}(\vec{\mathbf{x}}, t)$	Image with Tx/Rx Vector $\vec{\mathbf{u}}_a(t)$ and $\vec{\mathbf{u}}_b(t)$	$\mathbb{R}^{1}$
$\hat{\rho}(\vec{\mathbf{x}})$	Isotropic Summed Image	$\mathbb{R}^{1}$
$\mathbf{G}$	Gradient Matrix	$\mathbb{R}^{n\times n}$

Table 3.1: Variable Definitions. n is the degree of freedom of the scanner system. For a Field Free Point (FFP) scanner, $n = 3$, for a Field Free Line (FFL) scanner, $n = 2$.

However, MPI's millimeter spatial resolution is not yet competitive enough for preclinical imaging. There have been different efforts to improve MPI resolution and image quality from different aspects, including optimizing nanoparticles for resolution [43], simulating different trajectories for better image quality [21], proposing and building scanners with stronger gradient field [2, 4, 55], and deconvolving signal with a tolerable tradeoff in SNR loss [27].

Moreover, the MPI point spread function (PSF) is unique among all medical imaging modalities as the image resolution changes depending on the scanning velocity vector and is anisotropic with single channel excitation and detection. Fig. 3.1 (b,c) illustrates the anisotropy shown in the native MPI images using only a single excitation/receive channel (left-right and up-down, respectively), where there is intensity variations in different parts of the “Cal”, while the original phantom has approximately constant lumen diameter. The variations are highly dependent on the scanning parameters. This sort of variation would prevent the use of MPI to measure blood vessel diameter in a tortuous vessel.

In order to produce robust, high-quality images, the native MPI image should not depend on scanning parameters. In this paper, we implement two orthogonal excitation and detection coils, and demonstrate theoretically and experimentally that, with proper choice of MPI scanning trajectory and image processing, we are able to make native MPI images isotropic resolution independent of the scanning direction, thus enabling quantitative measurement of lumen diameter.

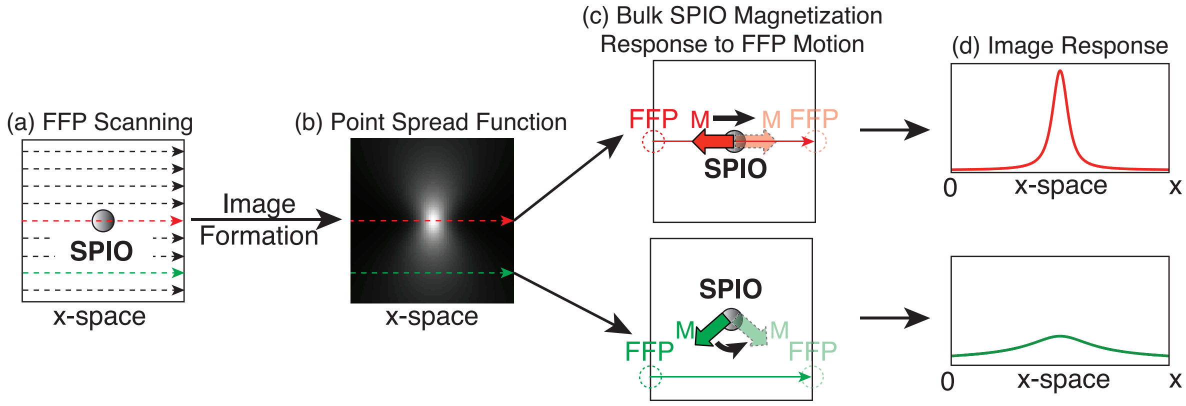

Figure 3.2: Illustration of MPI anisotropy with linear scanning. (a) An SPIO point source scanned with linear FFP trajectory. (b) PSF as a result of the linear scanning shows anisotropic resolution. (c) Two ways that the bulk magnetization responds to FFP line scans, through either magnetization magnitude change following Langevin physics, or merely rotation of the bulk magnetization. (d) Image response. In the red subfigure, the bulk magnetization desaturates and saturates obeying the Langevin function as the FFP swiftly scans right across the SPIOs, inducing a sharp image response. In the green subfigure, the FFP does not scan across the particles, keeping the SPIOs saturated. The SPIOs align with the external field through only changing the orientation of their magnetic moments. This slow angular change also induces a signal in the detector coil, but with a much lower and broader intensity.

3.2 Theory

In this section, we will investigate the source of the anisotropy inherent to the MPI PSF, and explore the necessary and sufficient condition to produce an isotropic PSF. To best analyze the resolution dependence on trajectory, we propose a tensor formulation of the MPI x-space imaging theory.

3.2.1 Physical Intuition of Anisotropy in MPI: Two Mechanisms of SPIO Reponse Applied Field

Intuitively, the anisotropy in MPI is a result of two different physical mechanisms that the assemble particles undertake to respond to the external applied field. Fig. 3.2 illustrates a simple example of anisotropy assuming a single point source in the center of the field of view (FOV), and a linear FFP trajectory. This scanning pattern produces a dumbell shaped resolution (Fig. 3.2 (b)). The resolution is better along the FFP scan direction, but worse along the perpendicular direction. The red line and green line shows the two different mechanisms individually.

The first mechanism is that the bulk magnetization changes magnitude to follow the FFP motion (shown in red). As the FFP scans through the center, the bulk magnetization desaturates to zero, flips 180°, and resaturates. This fast magnitude change induces a sharp image response.

The second mechanism is that the bulk magnetization rotates to align with the FFP motion with the same magnitude (shown in green). When the FFP offsets far enough from the center (shown in green), the bulk magnetization stays saturated during the line scan, and only rotates to realign with the external field instantaneously. The signal induced is mostly contributed from the slow angular change, which is a much lower and broader image response.

At any other point in the FOV, the image response is a mixture of these two different physical mechanisms. As the FFP scan offsets further from the center of the FOV, the angular change the assemble particles experience is smaller over the entire scan, thus the induced signal is lower and broader as the FFP moves further away from the center. Thus we observe a continous signal drop out and broadening from the center of the FOV to the outer margin of the FOV, resulting in a dumbell shaped resolution.

3.2.2 MPI's PSF: A Sum of Good and Bad Resolution Envelopes

We have demonstrated both theoretically and experimentally that, with baseline recovery [52], MPI is a LSI system. Therefore, we can analyze MPI resolution by exploring its PSF. We begin with the analytic PSF here [5]:

$$\begin{aligned}\mathbf{h}\left(\vec{\mathbf{x}}\right) =& \dot{\mathscr{L}}\left(\frac{\|\mathbf{G}\vec{\mathbf{x}}\|}{H_{sat}}\right)\frac{\mathbf{G}\vec{\mathbf{x}}}{\|\mathbf{G}\vec{\mathbf{x}}\|}\left(\frac{\mathbf{G}\vec{\mathbf{x}}}{\|\mathbf{G}\vec{\mathbf{x}}\|}\right)^{\mathbf{T}}\mathbf{G} \\ &+ \frac{\mathscr{L}\left(\|\mathbf{G}\vec{\mathbf{x}}\|/H_{sat}\right)}{\|\mathbf{G}\vec{\mathbf{x}}\|/H_{sat}}\left(\mathbf{I} - \frac{\mathbf{G}\vec{\mathbf{x}}}{\|\mathbf{G}\vec{\mathbf{x}}\|}\left(\frac{\mathbf{G}\vec{\mathbf{x}}}{\|\mathbf{G}\vec{\mathbf{x}}\|}\right)^{\mathbf{T}}\right)\mathbf{G} \qquad (3.1)\end{aligned}$$

where $\vec{\mathbf{x}}$ is a location vector in the imaging system, $\mathscr{L}$ is the Langevin function that describes the superparamagnetism behavior of the particles, H_{sat} is the saturation field strength of the magnetic tracer, $\mathbf{G}$ is the gradient field matrix that has the form $\begin{bmatrix} G_x & 0 & 0 \\ 0 & G_y & 0 \\ 0 & 0 & G_z \end{bmatrix}$. The system PSF can be decomposed into tangential and normal components [5]:

$$\mathbf{h}\left(\vec{\mathbf{x}}\right) = E_T\left(\vec{\mathbf{x}}\right)\mathbf{W}_T\left(\vec{\mathbf{x}}\right) + E_N\left(\vec{\mathbf{x}}\right)\mathbf{W}_N\left(\vec{\mathbf{x}}\right) \qquad (3.2)$$

where the tangential component is comprised of a tangential envelope $E_T\left(\vec{\mathbf{x}}\right)$ weighted by a spatially varying tangential weighting matrix $\mathbf{W}_T\left(\vec{\mathbf{x}}\right)$:

$$\begin{aligned}E_T\left(\vec{\mathbf{x}}\right) &= \dot{\mathscr{L}}\left(\frac{\|\mathbf{G}\vec{\mathbf{x}}\|}{H_{sat}}\right) \\ \mathbf{W}_T\left(\vec{\mathbf{x}}\right) &= \frac{\mathbf{G}\vec{\mathbf{x}}}{\|\mathbf{G}\vec{\mathbf{x}}\|}\left(\frac{\mathbf{G}\vec{\mathbf{x}}}{\|\mathbf{G}\vec{\mathbf{x}}\|}\right)^{\mathbf{T}}\mathbf{G} \qquad (3.3)\end{aligned}$$

and the normal component can also be expressed as the weighting of a normal envolope $E_N\left(\vec{\mathbf{x}}\right)$ by a normal weighting matrix $\mathbf{W}_N\left(\vec{\mathbf{x}}\right)$:

$$\begin{aligned}E_N\left(\vec{\mathbf{x}}\right) &= \frac{\mathscr{L}\left(\|\mathbf{G}\vec{\mathbf{x}}\|/H_{sat}\right)}{\|\mathbf{G}\vec{\mathbf{x}}\|/H_{sat}} \\ \mathbf{W}_N\left(\vec{\mathbf{x}}\right) &= \left(\mathbf{I} - \frac{\mathbf{G}\vec{\mathbf{x}}}{\|\mathbf{G}\vec{\mathbf{x}}\|}\left(\frac{\mathbf{G}\vec{\mathbf{x}}}{\|\mathbf{G}\vec{\mathbf{x}}\|}\right)^{\mathbf{T}}\right)\mathbf{G} \qquad (3.4)\end{aligned}$$

To provide intuition to these equations, we note that in response to a time-varying magnetic field, SPIO magnetization can change in both magnitude and orientation. Mathematically, it can be shown that the detected MPI signal is comprised from both components (Eq. 7 in [5]). $E_T\left(\vec{\mathbf{x}}\right)$, the high-resolution PSF envelope, arises from the change in the magnitude of the SPIO magnetization, which traverses the Langevin curve. Physically, this corresponds to the traversal of the FFP across a SPIO particle. This change in magnetic saturation has the shape of the derivative of the Langevin curve [4]. The low-resolution normal envelope, $E_N\left(\vec{\mathbf{x}}\right)$, arises from the rotation of the bulk magnetization to align with the time-varying magnetic field direction. $E_N\left(\vec{\mathbf{x}}\right)$ has been shown to have a 2.6× wider Full Width at Half Maximum (FWHM) than $E_T\left(\vec{\mathbf{x}}\right)$ [5]. We note that it also has a slow and undesirable drop-off as $1/\|\mathbf{G}\vec{\mathbf{x}}\|$, which manifests as image background haze and significantly reduces image contrast and resolution. Figure 3.3 displays the relative shapes of $E_T\left(\vec{\mathbf{x}}\right)$ and $E_N\left(\vec{\mathbf{x}}\right)$.

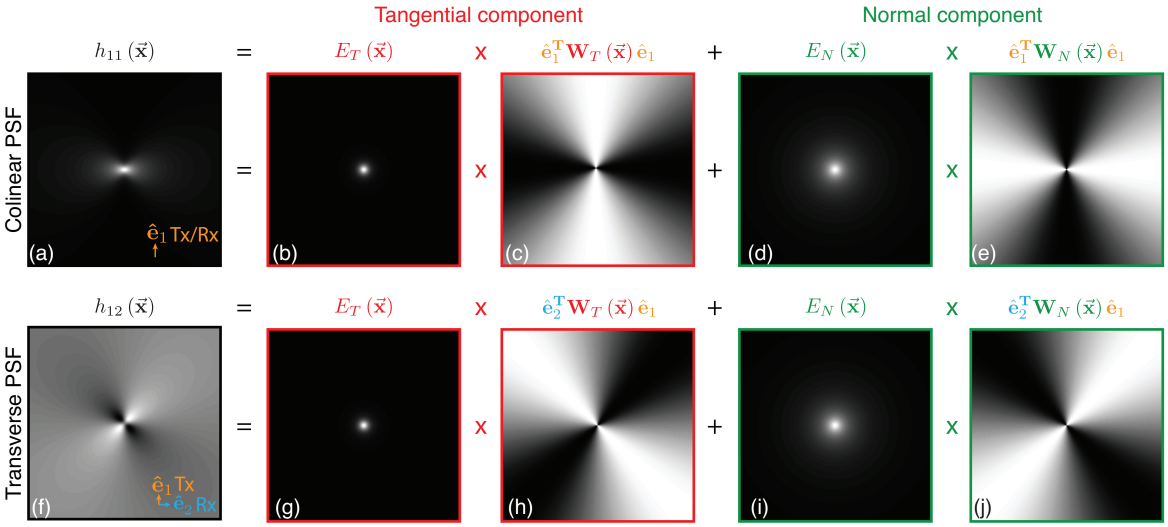

Figure 3.3: Dual-component decomposition of a collinear PSF (top), and a transverse PSF (bottom). Both tangential component and normal component consist of a multiplication of a radially symmetric envelope (b,d,g,i) by a spatially asymmetric weighting matrix (c,e,h,j). The tangential (b,g) and normal envelopes (d,i) are only dependent on the static gradient configuration and the particle properties, thus remain the same for the collinear/transverse scans. Normal envelope is the contour of the 2D Langevin distribution, whereas the tangential envelope is the contour of the 2D derivative of the Langevin distribution, which has 2.6 x better resolution than the normal envelope. Thus, the tangential component constitutes the better resolution component of the PSF. The weighting maps are dependent on both the gradient configuration and the scan/reception directions, and they are the source of anisotropy. For collinear scans, the tangential weighting matrix has the maximum value along with the scan direction whereas the normal weighting matrix is zero along the scan direction. The non-isotropic weighting maps cause the native MPI resolution with single scanning/receiving direction to be non-isotropic (dumbbell shaped PSF).

3.2.3 Recasting Multidimensional X-space Theory as Tensor Formulation

A closer look at the MPI PSF shows that, while $E_T(\vec{\mathbf{x}})$ and $E_N(\vec{\mathbf{x}})$ are scalar fields, $\mathbf{W}_T(\vec{\mathbf{x}})$ and $\mathbf{W}_N(\vec{\mathbf{x}})$ are 2^{nd} order tensors. Hence $\mathbf{h}(\vec{\mathbf{x}})$ is also a 2^{nd} order tensor for each position $\vec{\mathbf{x}}$. It is important to note that $\mathbf{h}(\vec{\mathbf{x}})$ (Eq. 3.1) only depends on the tracer magnetic property H_{sat} and the gradient field strength $\mathbf{G}$, and *is independent of scanning direction.*

For a Field Free Point (FFP) scanner, the tensor PSF $\mathbf{h}(\vec{\mathbf{x}}) \in \mathbb{R}^{3\times3}$, and we can enumerate elements of the PSF tensor as scalar images $h_{ij}(\vec{\mathbf{x}})$:

$$\mathbf{h}(\vec{\mathbf{x}}) = \begin{bmatrix} h_{11}(\vec{\mathbf{x}}) & h_{12}(\vec{\mathbf{x}}) & h_{13}(\vec{\mathbf{x}}) \\ h_{21}(\vec{\mathbf{x}}) & h_{22}(\vec{\mathbf{x}}) & h_{23}(\vec{\mathbf{x}}) \\ h_{31}(\vec{\mathbf{x}}) & h_{32}(\vec{\mathbf{x}}) & h_{33}(\vec{\mathbf{x}}) \end{bmatrix} \tag{3.5}$$

The MPI tensor image is similar in concept to diffusion tensor imaging in MRI, where the value at each spatial position is not a scalar intensity, but is instead a tensor comprised of directional diffusion coeffcients and their covariances. We generalize the MPI imaging equation in [5] (Eq. 12) to be the scalar nanoparticle density convolved with this tensor PSF. The resulting multidimensional MPI image $\boldsymbol{\Omega}(\vec{\mathbf{x}}) \in \mathbb{R}^{3\times3}$ is also a tensor, and can be expressed:

$$\begin{aligned} \boldsymbol{\Omega}(\vec{\mathbf{x}}) &= \rho(\vec{\mathbf{x}}) *** \mathbf{h}(\vec{\mathbf{x}}) && (3.6) \\ &= \begin{bmatrix} \hat{\rho}_{11}(\vec{\mathbf{x}}) & \hat{\rho}_{12}(\vec{\mathbf{x}}) & \hat{\rho}_{13}(\vec{\mathbf{x}}) \\ \hat{\rho}_{21}(\vec{\mathbf{x}}) & \hat{\rho}_{22}(\vec{\mathbf{x}}) & \hat{\rho}_{23}(\vec{\mathbf{x}}) \\ \hat{\rho}_{31}(\vec{\mathbf{x}}) & \hat{\rho}_{32}(\vec{\mathbf{x}}) & \hat{\rho}_{33}(\vec{\mathbf{x}}) \end{bmatrix} && (3.7) \end{aligned}$$

where $\rho(\vec{\mathbf{x}})$ is the scalar nanoparticle distribution and $\hat{\rho}_{ij}(\vec{\mathbf{x}})$ are the enumeration of each element of the multidimensional image tensor $\boldsymbol{\Omega}(\vec{\mathbf{x}})$ and are individually scalar images. We note that mathematically, $\hat{\rho}_{ij}(\vec{\mathbf{x}}) = \rho(\vec{\mathbf{x}}) *** h_{ij}(\vec{\mathbf{x}})$ and is merely the convolution of the input nanoparticle distribution with the corresponding scalar element of the PSF.

3.2.4 Probing the Multidimensional Image Tensor with Scanning

To produce an image, we probe the MPI system by scanning the FFP using a specific drive field trajectory through the FOV and receiving the signal using a combination of receiver coils [5]. Assuming an excitation field along an arbitrary excitation vector $\vec{\mathbf{u}}_a$, and a receiver coil receiving along a detection vector $\vec{\mathbf{u}}_b$, the image produced is a projection of the native tensor image $\boldsymbol{\Omega}(\vec{\mathbf{x}})$ onto the two respective vectors (Eq. 12 in [5]), which we generalize here as:

$$\hat{\rho}_{\vec{\mathbf{u}}_a,\vec{\mathbf{u}}_b}(\vec{\mathbf{x}}) = \vec{\mathbf{u}}_b{}^{\mathbf{T}}\boldsymbol{\Omega}(\vec{\mathbf{x}})\vec{\mathbf{u}}_a \tag{3.8}$$

where $\hat{\rho}_{\vec{\mathbf{u}}_a,\vec{\mathbf{u}}_b}(\vec{\mathbf{x}})$ is the acquired image using this trajectory, and is a scalar image. The concept of acquiring a scalar image by projecting an imaging tensor onto predefined axes is analogous to diffusion weighted imaging (DWI) in MR, where the diffusion tensor is projected onto a predetermined axis to form a scalar image of the directional diffusivity of water only along that axis.

Current MPI instruments are built with a fixed set of drive and receiver coils along the instrument's cardinal axes ($\vec{\mathbf{e}}_1$, $\vec{\mathbf{e}}_2$, and $\vec{\mathbf{e}}_3$). When we use one drive coil in direction $\vec{\mathbf{e}}_j$ and one receiver coil in direction $\vec{\mathbf{e}}_i$, the resulting MPI image selects the scalar element $\hat{\rho}_{ij}\left(\vec{\mathbf{x}}\right)$ from the multidimensional tensor image $\mathbf{\Omega}\left(\vec{\mathbf{x}}\right)$. For example, if we only use the x coil sets to both excite and receive along $\vec{\mathbf{e}}_1$, we get the collinear image along the instrument x-axis, which is also the 1st diagonal element $\hat{\rho}_{11}\left(\vec{\mathbf{x}}\right)$ of $\mathbf{\Omega}\left(\vec{\mathbf{x}}\right)$. On the other hand, if we use the y transmit coil to excite along $\vec{\mathbf{e}}_2$ and use the x receive coil to receive along $\vec{\mathbf{e}}_1$, we get the transverse image $\hat{\rho}_{12}\left(\vec{\mathbf{x}}\right)$, which is an off-axial element of $\mathbf{\Omega}\left(\vec{\mathbf{x}}\right)$. We show impulse responses generated using these two example trajectories, $h_{11}\left(\vec{\mathbf{x}}\right)$ and $h_{12}\left(\vec{\mathbf{x}}\right)$, in Fig. 3.3a and f.

In practice, however, the excitation and detection vectors can be time-varying and along any arbitrary direction. Examples of time-varying excitation trajectories include Lissajous or spiral FFP trajectories [2, 21, 23]. Notably, the detection vector can also be time-varying, which is feasible through linearly combining time-varying signals from orthogonal receiver coils. Assuming the instantaneous excitation and detection vectors are $\vec{\mathbf{u}}_a\left(t\right)$ and $\vec{\mathbf{u}}_b\left(t\right)$, then we can recast Eq. 3.8, where the instantaneous image $\hat{\rho}_{\vec{\mathbf{u}}_a,\vec{\mathbf{u}}_b}\left(\vec{\mathbf{x}}\left(t\right)\right)$ can be expressed as the following inner product:

$$\hat{\rho}_{\vec{\mathbf{u}}_a,\vec{\mathbf{u}}_b}\left(\vec{\mathbf{x}}\left(t\right)\right) = \vec{\mathbf{u}}_b\left(t\right)^{\mathbf{T}}\mathbf{\Omega}(\vec{\mathbf{x}}\left(t\right))\vec{\mathbf{u}}_a\left(t\right) \tag{3.9}$$

where $\vec{\mathbf{x}}\left(t\right)$ is the instantaneous FFP position. This equation shows that, as a result of a time-varying scanning and detection trajectory, the instantaneous image intensity obtained, $\hat{\rho}_{\vec{\mathbf{u}}_a,\vec{\mathbf{u}}_b}\left(\vec{\mathbf{x}}\left(t\right)\right)$, is a linear combination of the scalar components of the tensor image $\mathbf{\Omega}\left(\vec{\mathbf{x}}\left(t\right)\right)$ with respect to the instantaneous $\vec{\mathbf{u}}_a\left(t\right)$ and $\vec{\mathbf{u}}_b\left(t\right)$.

We note that each scalar image element $\hat{\rho}_{ij}\left(\vec{\mathbf{x}}\right)$ has different properties (see Fig. 3.3). Therefore, the property of the acquired image is dependent on how these scalar elements $\hat{\rho}_{ij}\left(\vec{\mathbf{x}}\right)$ are combined through $\vec{\mathbf{u}}_a\left(t\right)$ and $\vec{\mathbf{u}}_b\left(t\right)$. It quickly becomes clear that the MPI imaging trajectory can be chosen to optimize parameters such as resolution, SNR, magnetostimulation, and scan time. In this paper, we demonstrate a choice of trajectory to improve resolution, where we use two simple linear scans to sample the elements $\hat{\rho}_{22}$, $\hat{\rho}_{33}$ with no noise gain. However, this tensor imaging fomulation can be easily adapted to analyze other trajectories with no mathematical difference.

3.2.5 Excitation / Reception Trajectory Dependent Anisotropy

Each scalar component of the image tensor, $\hat{\rho}_{ij}$, has different directional anisotropy. This is visually apparent in Fig. 3.1b and c, which shows distinct differences between the two experimentally acquired “Cal” phantom images, $\hat{\rho}_{22}$ and $\hat{\rho}_{33}$, imaged along the y and z directions. The reason for this difference is that the projection of the PSF, $\mathbf{h}(\tilde{\mathbf{x}})$, onto the cardinal instrument axes $\vec{\mathbf{e}}_i$, namely, $h_{ii}(\vec{\mathbf{x}})$, is itself directionally anisotropic (visualized in Fig. 3.4a and b). To investigate the source of this anisotropy, we analyze $h_{ii}(\vec{\mathbf{x}})$ using Eq. 3.2and Eq. 3.8:

$$h_{ii}(\vec{\mathbf{x}}) = E_T(\vec{\mathbf{x}})\,\vec{\mathbf{e}}_i^{\mathbf{T}}\mathbf{W}_T(\vec{\mathbf{x}})\,\vec{\mathbf{e}}_i + E_N(\vec{\mathbf{x}})\,\vec{\mathbf{e}}_i^{\mathbf{T}}\mathbf{W}_N(\vec{\mathbf{x}})\,\vec{\mathbf{e}}_i \tag{3.10}$$

The envelopes $E_T(\vec{\mathbf{x}})$ and $E_N(\vec{\mathbf{x}})$ are isotropic regardless of the scanning pattern (Fig. 3.3). Thus, the directional anisotropy of $h_{ii}(\vec{\mathbf{x}})$ is due to the projection of the weighting matrices $\mathbf{W}_T(\vec{\mathbf{x}})$ and $\mathbf{W}_N(\vec{\mathbf{x}})$ onto the excitation and detection vectors, i.e. $\vec{\mathbf{e}}_i^{\mathbf{T}}\mathbf{W}_T(\vec{\mathbf{x}})\,\vec{\mathbf{e}}_i$ and $\vec{\mathbf{e}}_i^{\mathbf{T}}\mathbf{W}_N(\vec{\mathbf{x}})\,\vec{\mathbf{e}}_i$ (shown in Fig. 3.3c and e).

3.2.6 Achieving Isotropic Resolution with Multiple Orthogonal Scans

In this section, we will attempt to demonstrate that a simple summation is sufficient to eliminate MPI image anistropy for improved resolution. The technique presented here is deterministic (e.g. does not require choice of any regularization parameters) and reduces image noise through averaging.

We first normalize the orthogonal collinear images (i.e. $\hat{\rho}_{ii}$) by the gradient strength along each direction, then sum the resulting images together. With some effort (see Appendix C), we can prove that such a summation produces isotropic resolution. These normalization and summation operations can be succintly described:

$$\begin{aligned}\hat{\rho}(\vec{\mathbf{x}}) &= \mathrm{trace}[\boldsymbol{\Omega}(\vec{\mathbf{x}})\mathbf{G}^{-1}]\\ &= \sum_{i=1}^{3}\frac{\hat{\rho}_{ii}(\vec{\mathbf{x}})}{G_{ii}}\\ &= \rho(\vec{\mathbf{x}}) *** \left(E_T(\vec{\mathbf{x}}) + 2E_N(\vec{\mathbf{x}})\right)\end{aligned} \tag{3.11}$$

where$\hat{\rho}(\vec{\mathbf{x}})$ is the summed image and G_{ii} is the (i,i)-th element of the gradient matrix $\mathbf{G}$.

The key to Eq. 3.11 is that $\hat{\rho}(\vec{\mathbf{x}})$ no longer has weighting matrix dependencies. Removing the $\mathbf{W}_T(\vec{\mathbf{x}})$ and $\mathbf{W}_N(\vec{\mathbf{x}})$ dependence is powerful and produces an image that *does not depend on scanning direction.* We can see the improvement in image quality as we change from anisotropic to isotropic in Figure 3.4, where we show the yz cross-section of two orthogonal collinear PSFs probed along y and z axes, as well as the sum of these PSFs. We also see that this holds experimentally for experimental data in Figs. 3.1d and Fig. 3.6d.

3.2.7 Projection MPI Improves Resolution over 3D

For a field free line (FFL) scanner, we only need to make some minor modifications to Eq. 3.6 to make it a double convolution in addition to changing the dimensionality of

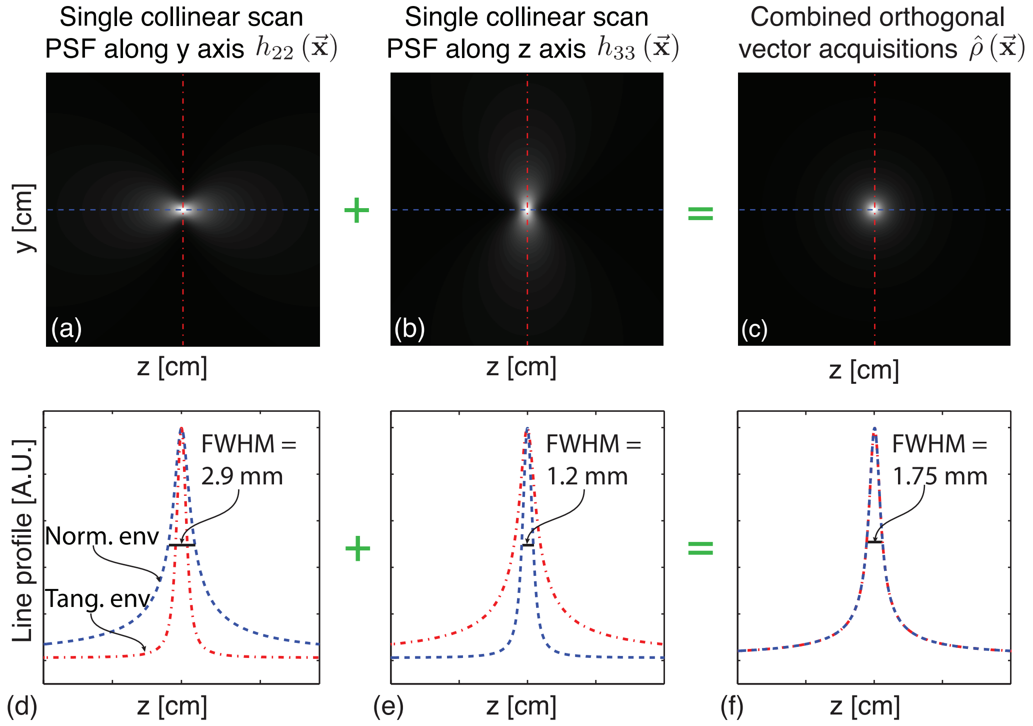
Single collinear scan PSF along y axis $h_{22}(\vec{\mathbf{x}})$

Single collinear scan PSF along z axis $h_{33}(\vec{\mathbf{x}})$

Combined orthogonal vector acquisitions $\hat{\rho}(\vec{\mathbf{x}})$

Figure 3.4: [Top] Two orthogonal collinear scans are sufficient to cancel out the anisotropy from the weighting factors to restore the averaged tangential and normal envelope in a 2D plane. (a-b) The xz cross-sectional image of the two collinear scans acquired along x and z directions respectively. (c) The combined orthogonal collinear PSF yield isotropic resolution. Similarly, three orthogonal collinear scans is sufficient for 3D isotropic resolution, if the gradient is isotropic in space. For Maxwell pair gradient configuration (where the gradient strength is twice as big as the other two directions), the combined PSF has a prolate spheroid shape. [Bottom] The line profile of the respected PSFs. It is shown that the resolution of the averaged collinear PSF is in between the resolution of the two envelopes.

the matricies to $\mathbf{h}, \mathbf{\Omega} \in \mathbb{R}^{2\times 2}$.

It is possible to extend Eq. 3.11 to FFL projection imaging with modest changes to the sizes of matrices [20, 38]. Again, summing the collinear images ($\hat{\rho}_{ii}$) gives us an isotropic image

$$\hat{\rho}(\vec{\mathbf{x}}) = \sum_{i=1}^{2} \frac{\hat{\rho}_{ii}\left(\vec{\mathbf{x}}\right)}{G_{ii}} = \rho\left(\vec{\mathbf{x}}\right) ** \left(E_T\left(\vec{\mathbf{x}}\right) + E_N\left(\vec{\mathbf{x}}\right)\right) \tag{3.12}$$

This result shows that, fundamentally, a combined image $\hat{\rho}$ from a FFL gradient will have better resolution than a 3D FFP imager with the same gradient strength. This occurs because the averaged PSF from a FFL would have one part of the good resolution component E_T and one part of the bad resolution component E_N compared to two parts of E_N in a 3D scanner.

3.3 Hardware Realization

As shown above, in order to achieve isotropic resolution, we need to implement multiple excitation and detection channels to be able to fully sample the trace of $\mathbf{\Omega}\left(\vec{\mathbf{x}}\right)$. To achieve a full 3D isotropic resolution, we need 3 orthogonal channels. However, due to bore size and power limitations in our current system, we can only implement two orthogonal transmit and receive channels to partially demonstrate the concept of this paper. We have chosen to implement two full channels along the cardinal instrument axes, y and z axis. The reason for this choice is that we want to take advantage of the natural resolution benefit along x axis, as the gradient strength along x is 7 T/m, which is 2x better than that of y and z. And also it is the easiest hardware configuration to make the direction of the coils align with the instrument axes, since we can use conventional solenoidal coils and saddle coils.

We also decide to drive each channel independently, forming a linear scanning trajectory. It is because that this is the simplest way to drive the system to fully sample the diagonal elements of $\mathbf{\Omega}\left(\vec{\mathbf{x}}\right)$ separately with no noise gain. With additional decoupling matrix in the hardware between y and z channels, we could potentially drive the two coils simultaneously to form different scanning trajectories, such as Lissajous or spiral, but these trajectories need to be implemented with care, because they do not fully sample the trace elements without noise gain.

3.4 Methods and Materials

3.4.1 Multichannel Hardware

All the experiments were performed on a FFP scanner [55] developed at UC Berkeley (Fig. 3.5 (a)). To enable multichannel acquisition, we built two orthogonal excitation and receive channels. Fig. 3.5 (b) shows the two excitation coils. The transverse coil was a double layered Golay coil pair (7 turns/layer, 12.7 cm long) made out of thin copper sheet (2 mm) cut out by a programmed Dremel (Robert Bosch Tool Corp., Germany). The two layers were separated and insulated by Kapton tape (Dupont, DE, USA, 1 mil), jointed by soldering, and formed on a G-10 tubing (ID = 2.75", OD = 3.15"). On top of the transverse coil, we wound an axial coil wound with hollow magnet wire. The transmit coil assembly was then potted together by heat conductive epoxy (company) and integrated into the scanner. Two AE 7796 power amplifiers (AE Techron Inc., IN, USA) were connected in series to power the transmit coils. Both the axial and transverse coils can produce 40 mTpp field using 1.6 kW and 2.7 kW respectively. We also custom built two orthogonal receive coils with homogeneous reception in the imaging volume. Gradiometer configuration is implemented to cancel direct feedthrough (Fig. 3.5 (c)). The coil body was designed with Solidworks (SolidWorks Corp., MA, USA) and 3d printed (3D Systems, Inc., SC, USA), and wound with Litz wire (MWS Wire Industries, CA, USA). The sensitivity of the axial and transverse coil is 860 μT/A and 420 μT/A respectively.

3.4.2 Phantom Construction

To validate the resolution improvement by this proposed method, we constructed three different imaging phantoms; all were laser engraved out of an acrylic plate.

First, we constructed a "Cal" phantom (Fig. 3.6 (a)), which has approximately 2 mm uniform channel width throughout the phantom. The channels were then injected with undiluted Mircomod nanomeg Mip particles (micromod Partikeltechnologie GmbH, Germany).

We also constructed a resolution phantom (Fig. 3.6 (a)), and we evenly distributed 6 groups of channels around the circumference of the phantom. Within each group, the channels are separated by a well controled distance, from 3 mm to 0.5 mm. We then injected the channels with 5x diluted Micromod Nanomeg MIP particles and seal the channels with clear nail polish.

Lastly, we constructed a coronary artery phantom (Fig. 3.7 (a)). We placed a stenosis model in one of the branching vessels, and we also injected the arterial channels with 5x diluted Micromod nanoparticles.

3.4.3 Scanning Parameters

The experiments were performed with linear excitations. In each set of experiments, we acquire two orthogonal collinear scans. In each scan, the FFP is excited sinusoidally in either y or z axis with the corresponding RF coil to create a partial FOV (pFOV). Both channels produced RF excitation fields with strength of 30 mTpp. The pFOV is then rastered with a cartesian trajectory across the entire imaging FOV. Mechanical movement of the sample occurs in the z axis with 67% pFOV overlap.

For the “Cal” phantom, the imaging FOV for collinear y scan is 2 cm by 4.1 cm by 10 cm along x, y and z axis respectively. The scan time is 7.5 minutes. The imaging FOV for collinear z scan is 2 cm by 4.5 cm by 9.9 cm, with a scan time of 2 minutes.

For the resolution phantom and the coronary artery phantom, the imaging FOVs for both channels were 2 cm by 4.5 cm by 5 cm, with a y scan time of 3.75 minutes, and z scan time of 1 minute.

3.4.4 Reconstruction / Post-Processing

To reconstruct and process the MPI imaging data, we first reconstruct each collinear channel separately with x-space reconstruction in software (MATLAB, Mathworks, MA, USA). The signal is normalized by the receive coil sensitivity, and interpolated onto the same sampling density and averaged to form a composite image.

3.4.5 Equalization Filter

To reduce the haze in the MPI image from the normal envelope, we constructed an equalization filter in k-space (a detailed explanation of this equalization filter, appears in the next chapter). We analytically calculate the 3D Fourier transform of the tangential and normal envelope, and take a ratio of the desirable tangential envelope over the summation of the tangential and normal envelope. This operation forms the 3D equalization filter, and we apply this filter to the averaged MPI image of the coronary artery phantom. This equalization operation dehazes the image, improves image contrast, and thus makes the MPI signal truly quantitative to the lumen diameter.

3.5 Results

In Fig. 3.6 we see how multichannel acquisition achieves isotropic resolution in a resolution phantom. The subfigures (b) and (c) show the two orthogonal collinear scans in the horizontal and vertical directions respectively, both showing anisotropic resolution. After processing the two scans and averaging, the result shown in Fig, 3.6 (d), shows isotropic resolution.

Fig. 3.7 shows that multichannel acqusition with equalization enables quantitative measurement of sub-millimeter lumen diameter. Fig. 3.7 (a) shows the MPI phantom, Fig. 3.7 (b) shows a representative single channel MPI scan, and Fig. 3.7 (c) shows the combined MPI image with equalization. We compare the MPI image with micro-CT images of the same phantom in Figs. 3.7 (d,e,f), which show that MPI image intensity is within 3% of the measured lumen diameter (Fig. 3.7 (g)).

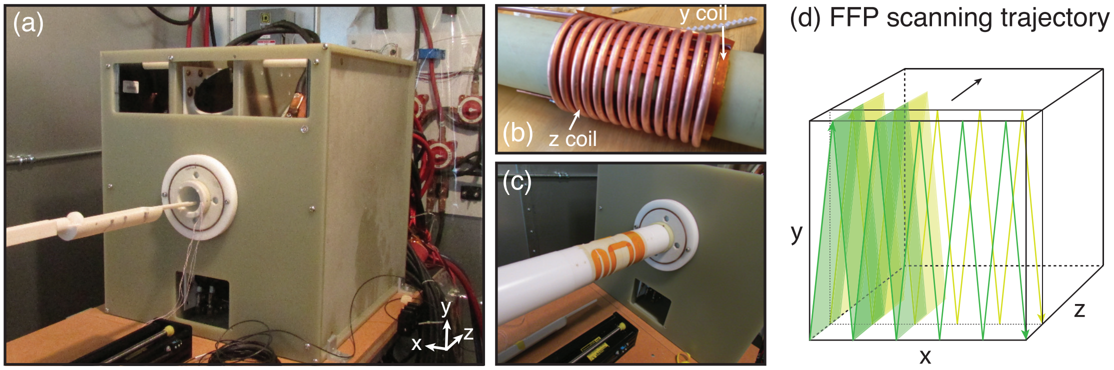

Figure 3.5: Photos of multi-channel MPI hardware. (a) Gertrude x-space FFR scanner developed at UC Berkeley. (b) Customized transmit coil assembly with a water-cooled solenoid coil for generating axial RF field and a double-layered Golay coil pair for generating transverse RF field. (c) Customized receive coil assembly with an axial and transverse receive coil respectively. (d) One example of FFP trajectories used to acquire the collinear z images.

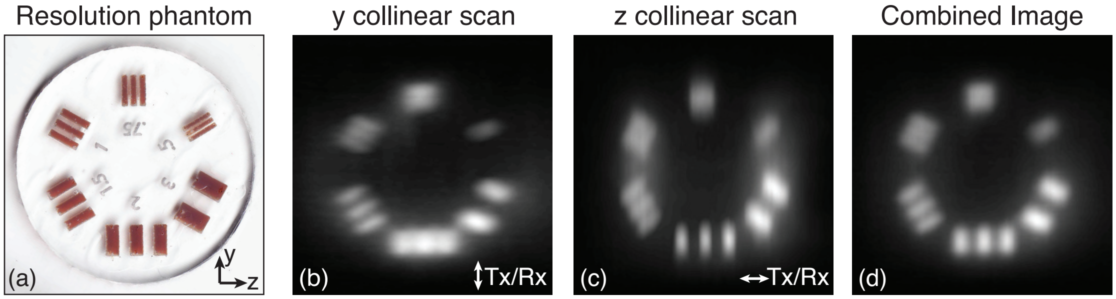

Figure 3.6: Experimental data on a resolution phantom shows resolution and contrast improvement with combining two orthogonal channels and equalization. (a) Photograph of a resolution acrylic phantom injected with 5x diluted Micromod Nanomag-MIP particles. The laser-cut numbers represent the width and spacing of the channels within each group, with the unit in [mm]. (b-c) Collinear scan acquired with a single y or z channel, showing anisotropic resolution. (d) Combining two orthogonal collinear scans from (b) and (c) achieves isotropic resolution.

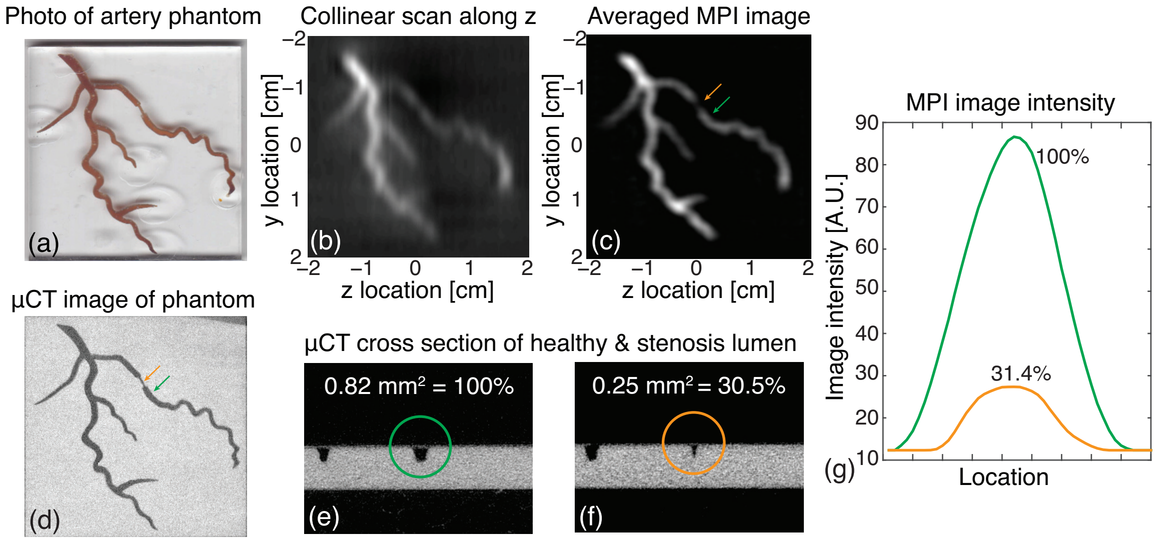

Figure 3.7: Combined vector acquisition and equalized MPI images can be used to quantify lumen size. (a) Photograph of a coronary artery phantom injected with 5x diluted Micromod Nanomag-MIP particles, with a built-in stenosis model in the right branch of the arteries. (b) Collinear scan acquired along z. (c) Combined and equalized MPI image of the two orthogonal collinear scans, the two arrows point out the intensity differences for different artery sizes. (d) μCT image of the same phantom with air-filled channels as contrast mechanism. (e-f) μCT images of the two cross sections of the healthy and stenosis artery channels pointed out by arrows in (d), and the lumen size was quantified in the image. (g) The MPI image intensity is proportional to the lumen size quantified by μCT images.

3.6 Discussion

The implications of this paper are beyond multichannel acquisition for isotropic resolution. In this paper we have also explored the mathematical properties of the MPI PSF, and discovered the PSF is actually a tensor. The tensor formulation helps us understand analytically how the particle interacts with the applied field, which lends understanding into the physical sources of resolution anisotropy, SNR, trajectory-dependent LSI, etc. Deep knowledge of the PSF leads to improving x-space resolution, optimizing scanning trajectory design, and consequently, the ability to quantitatively measure lumen diameter.

3.6.1 Properties of the MPI PSF

The two competing mechanisms that produce signal in MPI are the nanoparticle passing through the Langevin curve (E_T) and the rotation of the magnetic moment to align with the applied field (E_N). The bad resolution component E_N has a 2.6-fold broader Full Width at Half Maximum (FWHM) than the good resolution component E_T, and it has a slow drop-off as a $1/Gr$ tail, which introduces a lot of background haze to the image undesirably. The two resolution envelopes are determined by the gradient field strength and the physical properties of the particle tracer. With a stronger gradient field or better nanoparticles, we could improve MPI resolution by have sharper E_T and E_N.

The best native resolution a specific scanner can achieve is E_T. However, the received signal will always be a mixture of those two physical mechanisms from E_T and E_N, and will always be acquired simultaneously. This means no acquisition technique (e.g. scanning pattern, analog filter, or time domain digital filter) can separate these two physical processes from each other. This means, to tease out the good resolution component E_T, we need to apply some more advanced image processing technique, and this will be the topic of the next chapter.

3.6.2 Field Free Line Scanner Is More Advantageous Over Field Free Point Scanner

It needs to be highlighted that, for a FFL scanner, we only need to implement two orthogonal channels instead of three to achieve isotropic resolution. The need for one fewer excitation and receive channel has a lot of hardware advantages: there would be more imaging bore space freed up for larger subjects, less power consumption from a 3rd channel, and less complex controls and decoupling circuitry.

Another advantage of FFL scanner over FFP scanner lies in resolution. First of all, in FFL, we only need to average two orthogonal channels, which means the averaged PSF is $E_T + E_N$, which has better resolution than the FFP averaged PSF $E_T + 2E_N$, making the images shaper and better quality. Secondly, FFL configuration guarantees the resolution envelopes E_T and E_N are isotropic, whereas in FFP, the two envelopes shape like oblate spheroids (looks like an M&M shape), which is not strictly isotropic in all three directions. The reason for this is that MPI gradient uses the maxwell coil pair configuration for both FFP and FFL scanners, to achieve an optimal linear gradient field. If it is an FFL scanner, an examplary gradient field would be 6 T/m in both Y and Z axis, and zero along Z axis, creating isotropic planar resolution in YZ plane. With projection reconstruction, we can achieve the same resolution along the third X axis, ensuring 3D isotropic resolution. On the contrary, for a FFP scanner, an examplary gradient field would be 3.5 T/m along Y and Z axis, while the gradient is 7 T/m along the third X axis, yielding an oblate spheroidal 3D resolution. Therefore, FFL has better resolution benefit than FFP scanner.

Lastly, the FFL scanner is advantageous over the FFP scanner because it has higher SNR as the FFL signal is an integral of the signal along its projection direction.

In summary, we see that the FFL is better than the FFP scanner because of the hardware simplicity, lower power consumption, more bore size, better resolution and higher SNR.

3.6.3 Tensor PSF has Implications for FFP Scanning Trajecoty Design

The scope of this paper only focused on linear scans that is excited and detected along the instrument coordinate axes. A natural question would be, what about other arbitrary linear scans that do not follow the coordinate axes? Moreover, what about nonlinear trajectories, such as Lissajous, rose, or spiral? As it turns out, these trajectories differ in how they probe and project the MPI tensor PSF onto different scanning trajectories. Therefore, we could analyze the tensor PSF to assess the effect of different trajectories on the MPI images.

For other off-axis linear trajectories, it could be shown that the resultant image is just a linear combination of the tensor PSF components, namely, it is a linear mixture of the 3 collinear images and the 6 transverse images acquired by 3 channels along the instrument coordinate axis. It could be proven that 3 orthogonal on-axis scans are sufficient for isotropic resolution – therefore, scans along any other linear direction will add no further information.

Nonlinear trajectories might have advantage over linear trajectories in terms of SNR, scan efficiency, magnetostimulation/SAR limit and resolution. The SNR benefit might come as a fact that nonlinear trajectories could potentially incorporate in the signal energy from the transverse scans (the off-diagonal components in the tensor PSF).

Currently, it is unclear how to design these pulse sequences, nor is there a good way to assess the performance of these pulse sequences, or instruct optimal reconstruction algorithms for each trajectory. In this chapter, we have proposed the generalized tensor formulation of x-space theory. It is a powerful tool as the tensor PSF contains the complete analytic information of the whole system – its resolution, anisotropy, and it describes how different trajectories project the PSF onto the real image space. It could be used to analyze different nonlinear trajectories, to assess the performance of each case – whether or not it is still LSI, whether or not it yields a better resolution, and it could instruct the most optimal reconstruction algorithm for each specific case if we need to optimize or ensure a certain property, such as SNR, resolution, or LSI.

3.6.4 Quantitative MPI Measurement of Lumen Diameter

Fig. 3.7 is a proof of concept experiment of lumen diameter measurement with MPI imaging result. We demonstrate that with the improved resolution and image contrast, MPI can be used to quantitatively measure small lumen sizes in a angiogram. Along with other benefits of MPI as an angiographic imaging technique, for instance, the utility of a much safer tracer, magnetic nanoparticles, than the iodine or gadolinium used in CTA or MRA, and non-ionizing radiation, MPI has a great potential to be used as a safer angiogram imaging modality.

3.7 Conclusion

We proved and experimentally demonstrated that we can reshape the MPI PSF to be isotropic and well-behaved with multi-channel acquisition. This allows us to improve MPI resolution. Finally, these improvements enable us to use MPI to quantitatively measure the lumen diameter of small arteries in angiograms.

Chapter 4

Dehazing with K-space Equalization Filter for Improved Resolution and Conspicuity in *In Vivo* Magnetic Particle Imaging

The image quality of MPI is defined by the properties of the Point Spread Function (PSF), which is defined as the image that is produced for a single point source [5]. In the previous chapter, we have demonstrated that with multichannel acquisition, we can reshape MPI resolution to be isotropic (see Fig. 4.1d) ; however, the native MPI images

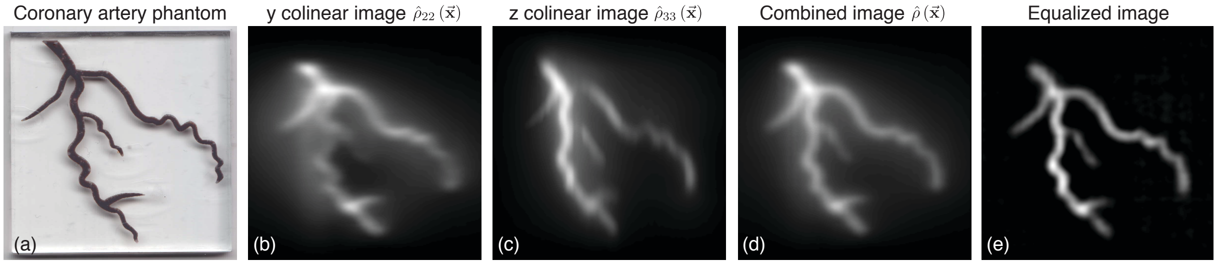

Figure 4.1: Equalization improves MPI native resolution and conspicuity. Experimental MPI imaging data acquired on a 7 T/m x 3.5 T/m x 3.5 T/m MPI scanner. (a) Photograph of a coronary artery shaped acrylic phantom injected with undiluted Micromod Nanomag-MIP particles. (b) Collinear scan acquired with a single y channel, showing anisotropic resolution. The horizontal haze is due to the slow signal decay perpendicular to excitation direction, and this haze blurs image and reduces its contrast. (c) Collinear scan acquired with single z channel. (d) Combining two orthogonal collinear scans from (b) and (c) achieves isotropic resolution. (e) Equalization filter in k-space dehazes the combined multichannel acquisition image without amplifying noise.

still have significant haze that reduces image contrast and conspicuity.

MPI's signal haze is mathematically related to the haze seen in non-filtered backprojection in Computed Tomography (CT). To illustrate the undesireability of the signal haze, Fig. 4.2e shows an CT image reconstructed with nonfiltered backprojection. In non-filtered CT, a bright signal from bone would obscure smaller signals from nearby white matter and grey matter, and so unfiltered CT remains a mathmatical curiosity and is never used clinically.

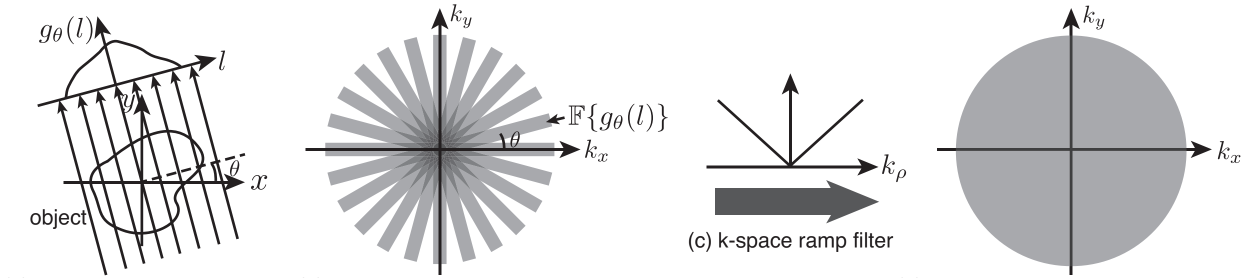

(c) k-space ramp filter

(a) projection in real space (b) nonfiltered backprojection in k-space (d) filtered backprojection in k-space

(e) image reconstructed with nonfiltered backprojection (f) image recon with filtered backprojection

Figure 4.2: Background on CT reconstruction and the source of haze from nonfiltered backprojection algorithm. (a) CT projection in the real space. (b) The k-space illustration of a direct backprojection of each of the projection data $g_\theta(l)$ back onto the image space. According to the central slice theorem, the 1D Fourier transform of each projection along a specific angle is equivalent to a line in k-space at the same projection angle. For example, the projection in (a) at angle θ corresponds to the anglular θ line in k-psace of the object after Fourier transform. One thing to note is that without any filtering, the center of the k-space is heavily oversampled, which leads to the 1/r haze seen in (e). (c) A k-space ramp filter could be applied to dehaze the nonfiltered backprojected image. (d) After applying the k-space ramp filter, the k-space sampling density is normalized, therefore there is no over-emphasis on the center of the k-space (the low spatial frequency part). (f) Filtered backprojection reconstruction dehazes and achieves a sharp resolution image.

Fortunately, we demonstrate here that the haze is mathematically well behaved and is a result of over-emphasis of the center of the k-space and, with image equalization, it is possible to reshape MPI's PSF so that it produces no haze in images. This form of equalization is already used in Filtered Back-projection (FBP) CT, which suppresses the 1/r haze from backprojection using a k-space ramp filter (see Fig. 4.2). A k-space ramp filter in MPI unnecessarily amplifies noise, and so instead we analytically derive a robust k-space equalization filter that does not amplify noise and demonstrates the technique experimentally.

We have demonstrated that multichannel acquisition and equalization, taken individually, improve image resolution and contrast only modestly. However, taken together, these improvements dramatially increase image conspicuity and enable the first quantitative measurements of lumen area in a sub-millimeter diameter blood vessel phantom.

4.1 Theory

In this section, we will investigate the source of the haze inherent to the MPI PSF, and then explore, using an equalization filter to eliminate the signal haze, enabling higher contrast and improved resolution without amplifying noise.

4.1.1 Review on Multichannel Acquisition

We have proven that a summation three orthogonal collinear MPI images produces isotropic resolution. This can be succintly expressed

$$\begin{aligned}\hat{\rho}(x) = \mathrm{trace}[\mathbf{\Omega}(\vec{\mathbf{x}})\mathbf{G}^{-1}] &= \sum_{i=1}^{3}\hat{\rho}_{ii}\left(\vec{\mathbf{x}}\right)/G_{ii} \\ &= \rho\left(\vec{\mathbf{x}}\right) *** \left(E_T\left(\vec{\mathbf{x}}\right) + 2E_N\left(\vec{\mathbf{x}}\right)\right) \qquad (4.1)\end{aligned}$$

where $\rho\left(\vec{\mathbf{x}}\right)$ is the input particle distribution, $\hat{\rho}(x)$ is the combined image after summing multichannel acquistion, $\mathbf{\Omega}(\vec{\mathbf{x}})$ is the multidimensional image matrix, $\mathbf{G}$ is the magnetic field gradient, $\hat{\rho}_{ii}\left(\vec{\mathbf{x}}\right)$ is one of the three orthogonal collinear images, $E_T\left(\vec{\mathbf{x}}\right)$ and $E_N\left(\vec{\mathbf{x}}\right)$ are the two PSF envelopes that have different resolutions, governed by two different physical mechanisms of the particle response to the applied magnetic field. The key accomplishment of this multichannel acquisition technique is that it removes the scanning trajectory dependency of the image and thus produces an image that *does not depend on scanning direction.* We can see the improvement in image quality as we change from anisotropic to isotropic from experimental data in Figs. 4.1d and 4.7d.

We have also shown that it is possible to extend Eq. 4.1 to projection imaging with modest changes to the sizes of matrices [20]. Again, summing the collinear images ($\hat{\rho}_{ii}$) gives us an isotropic image

$$\begin{aligned}\hat{\rho}(\vec{\mathbf{x}}) &= \sum_{i=1}^{2}\frac{\hat{\rho}_{ii}\left(\vec{\mathbf{x}}\right)}{G_{ii}} \\ &= \rho\left(\vec{\mathbf{x}}\right) ** \left(E_T\left(\vec{\mathbf{x}}\right) + E_N\left(\vec{\mathbf{x}}\right)\right) \qquad (4.2)\end{aligned}$$

Thus fundamentally, a combined image $\hat{\rho}$ from a field free line (FFL) gradient will have better resolution than a 3D imager with the same gradient.

4.1.2 Fourier Equalization for MPI Dehazing

As seen in Fig. 3.3 from the previous chapter, the normal envelope $E_N(\vec{\mathbf{x}})$ has worse resolution, namely, broader Full Width at Half Maximum (FWHM) than $E_T(\vec{\mathbf{x}})$. The normal envelope $E_N(\vec{\mathbf{x}})$ also drops off as a function of $1/r$. This wider FWHM and slow dropoff make this component far less desireable, and indeed the $1/r$ dropoff introduces an image "haze" that reduces image contrast.

The signal haze resembles unfiltered CT back-projection, which also has a $1/r$ signal dropoff and is not used clinically because of poor image quality. In this section, we are inspired by the solution in CT to eliminate the background haze through k-space ramp filtering, and we proposed a k-space equalization filter that is similar in concept, but strategically chosen to only eliminate the E_N component of the image but preserve the E_T component. We will explore the theory, implementation, robustness, and noise performance of this simple equalization approach to eliminate the haze by decomposing an MPI image into tangential and normal images.

We begin by transforming the summed image into the Fourier domain.

$$\mathbb{F}_{3D}\left\{\hat{\rho}(\vec{\mathbf{x}})\right\} = \mathbb{F}_{3D}\left\{\rho(\vec{\mathbf{x}})\right\}\mathbb{F}_{3D}\left\{E_T(\vec{\mathbf{x}}) + 2E_N(\vec{\mathbf{x}})\right\} \tag{4.3}$$

Eq. 4.3 gives the summed image in the Fourier domain. Here, we see that the blur arises from two different envelopes, E_T and E_N. The source of the image haze (See Figs. 4.1d) is the bad envelope E_N, which arises from the physical rotation of the magnetic nanoparticle. Images produced by this rotation drop off as $1/r$, giving a signal haze.

The key insight to dehazing the image without noise gain is that this drop-off is very similar to the $1/r$ blur seen in unfiltered CT backprojection. In unfiltered backprojection, the center of the k-space is oversample by the simple backprojection reconstruction, and the over-emphasis in the low spatial frequency part of the k-space results in a $1/r$ blurry kernel that introduces significant hazes in the image. To reduce the haze, namely, to suppress the low spatial frequencies in the k-space, we use a k-space ramp filter, which equalizes the k-space spectrum to compensate for higher sampling density at the center of k-space. Similarily, in MPI the $1/r$ tail of the bad envelope E_N overemphasizes low spatial frequencies. This suggests that careful choice of a k-space filter could reshape the PSF and eliminate the $1/r$ haze.

Constructing an equalization filter for MPI requires knowledge of the PSF as defined by physics as well as the desired PSF (which is E_T). From the relationship between the two PSF envelopes, we can derive a k-space filter that de-emphasizes the low spatial frequencies. Through careful choice of this filter, we can ensure that there is no ringing or noise gain.

Let us demonstrate this concept by deriving a k-space filter to isolate the E_T and E_N components of the PSF. In Appendix D, we have provided a complete analytical derivation and approximation of the x-space and k-space expression of each envelope components and the analytic expression of the equalization filter. Here, we will just provide the final expression of this k-space filter

$$\Phi_{3D,T}\left(\vec{\mathbf{k}}\right) = \frac{\mathbb{F}_{3D}\left\{E_T\left(\vec{\mathbf{x}}\right)\right\}}{\mathbb{F}_{3D}\left\{E_T\left(\vec{\mathbf{x}}\right) + 2E_N\left(\vec{\mathbf{x}}\right)\right\}} \tag{4.4}$$

$$\approx \frac{|k|}{|k| + G_0(2\pi H_{sat})^{-1}} \tag{4.5}$$

$$\Phi_{3D,N}(\vec{\mathbf{k}}) = 1 - \Phi_{3D,T}(\vec{\mathbf{k}}) \tag{4.6}$$

where $\Phi_{3D,T}\left(\vec{\mathbf{k}}\right)$ is the k-space filter to only extract the tangential envleope E_T, and it is the desirable equalization filter to get the best spatial resolution in MPI given a specific scanner. $\Phi_{3D,N}\left(\vec{\mathbf{k}}\right)$ is the compliment filter that extracts the undesirable normal envelope E_N. The shape of the first equalization filter can be seen in Fig. 4.3a.

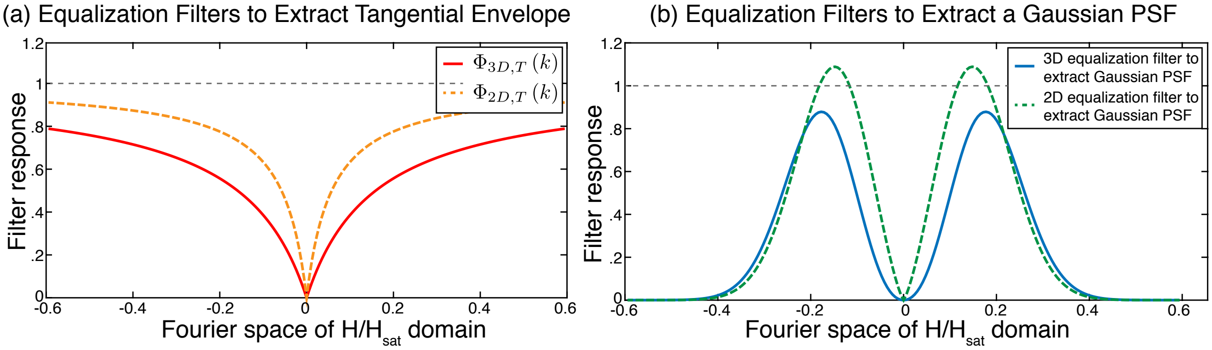

Figure 4.3: 1D profile of different equalization filters in the magnetic-Fourier space for a 20 nm nanoparticle in a 3.5 T/m gradient. (a) Equalization filters to extract the tangential component (good resolution) in a 2D projection scanner or a 3D FFP scanner. (b) Equalization filters to reshape the PSF into a Gaussian with the same FWHM as the tangential component in 2D and 3D case.

In a 2D FFL projection scanner, with some modification, the equalization filter can be expressed as below and visualized in Fig. 4.3a:

$$\Phi_{2D,T}\left(\vec{\mathbf{k}}\right) = \frac{\mathbb{H}_0\left\{E_T\left(\vec{\mathbf{x}}\right)\right\}}{\mathbb{H}_0\left\{E_T\left(\vec{\mathbf{x}}\right) + E_N\left(\vec{\mathbf{x}}\right)\right\}} \tag{4.7}$$

$$\approx \frac{|k|}{|k| + G_0(5.5\pi H_{sat})^{-1}} \tag{4.8}$$

Applying the k-space equalization filter to the averaged PSF from multichannel acquisitions gives us the tangential component E_T of the PSF:

$$\hat{\rho}_T(\vec{\mathbf{x}}) = \mathbb{F}_{3D}^{-1}\left\{\Phi_{3D,T}(k)\mathbb{F}_{3D}\left\{\hat{\rho}(x)\right\}\right\} \tag{4.9}$$

$$\approx \rho\left(\vec{\mathbf{x}}\right) *** E_T\left(\vec{\mathbf{x}}\right) \tag{4.10}$$

$$\hat{\rho}_N(\vec{\mathbf{x}}) = \mathbb{F}_{3D}^{-1}\left\{\Phi_{3D,N}(k)\mathbb{F}_{3D}\left\{\hat{\rho}(x)\right\}\right\} \tag{4.11}$$

$$\approx \rho\left(\vec{\mathbf{x}}\right) *** E_N\left(\vec{\mathbf{x}}\right) \tag{4.12}$$

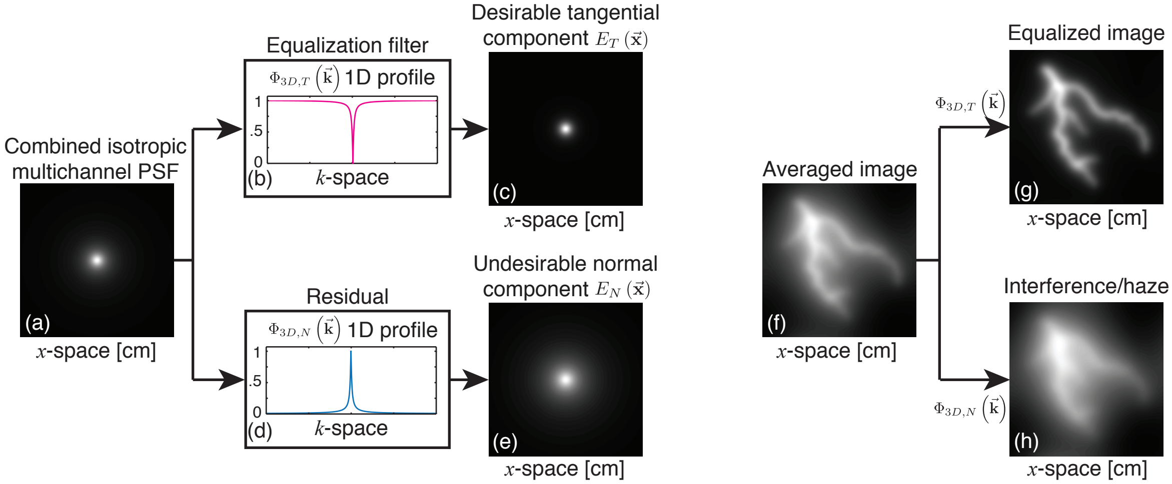

Figure 4.4: Demonstration of equalization technique to get rid of the haze. (a) Combined multichannel acquisition PSF to be equalized. (b) 1D profile of the radially symmetric k-space equalization filter. (c) Equalized PSF is effectively the tangential envelope (good resolution component). (d) 1D profile describing the transfer function of the residual after equalization operation in k-space. (e) The residual component is effectively the normal envelope that contribute to bad resolution and contrast. (f) Combined isotropic MPI "coronary artery" image from multichannel acquisition. (g) Equalized coronary artery image containing the good resolution component. (h) The residual normal component consititutes the blurry background haze.

For illustration, we show how this equalization filter works on the combined isotropic PSF and MPI images in Fig. 4.1.2. We see that after applying the equalization filter, the two filters handily separate the tangential component and the normal component of the PSF and the image.

We should also note that the numerator of the filter in eq. 4.5 is not restricted to E_N and E_T. We can choose any shape of a desired PSF and with the equalization filter we can reshape the received image resolution into the aimed resolution. For example, we can reshape the desired PSF into a gaussian, because a gaussian PSF is well-behaved in both spatial and k-space domain, and it is convenient for SNR analysis for MPI. We have adapted the equalization filter to reshape the PSF into a gaussian with the same

FWHM as the tangential envelope, and the two filters for FFP and FFL cases are shown in Fig. 4.3b. It is noted that the equalization filter for FFL case would increase noise in a small k-space frequency range by 5-10%. While a minimal noise amplification for a small frequency range is tolerable, we need to be careful in choosing a target PSF for the equalization, because improper and aggressive choice of a target PSF can lead to substantial noise gain, ringing, etc.

4.2 Performance of Equalization Filter

We have proposed this equalization filter to reshape the PSF from physical principles. One advantage of this equalization filter is its well-behaved noise properties. In this section, we will explore the noise performance as we run the equalization filter on a series MPI images with different SNRs, and compared the SNR and noise power before and after equalizing.

However, another bigger concern would be the robustness of this equalization scheme. When we use different tracers with different magnetic properties, the native MPI resolution differs, so as both the tangential and normal envelopes. Moreover, even with the same particle, when it is in aqueous solutions as opposed to biological environments, such as blood, intracellular matrix, or inside of cells, the local chemical environment and viscocity differences would profoundly change how the nanoparticle relaxes and responds to the applied field, thus introducing relaxation effect, which translates to broadening or skewing of the PSF. This will also significantly change the shape of the tangential and normal envelopes. In certain applications, we would like to ulitize the PSF change as an indicator for targeting or biological contrast. Would the same equalization filter be able to account for these changes, and still faithfully only suppresses the normal envelope and preserves the tangential envelope in all circumstances? It is a very interesting area for investigation, and we certainly would like to have an equalization filter that is robust and unaffected by all of these parameters. This means the dehazed image would still reproduce the same resolution differences expected from two different groups of tracers. In this section, we will conduct a preliminary experiment to compare the resolution differences before and after equalization between two well characterized particle groups, and assess the robustness of the same equalization filter across two different particles.

4.2.1 Noise properties of Fourier Equalization

Fourier equalization differs substantially from deconvolution. Equalization is a method for reshaping the point spread function of a system, which was demonstrated in the early 1900s for telephonly [56], and later for audio equalization in acoustics [57]. Importantly, we are able to demonstrate here that equalization does not rely on knowing the PSF parameters to unreasonable accuracy or choices of regularization parameters, it does not amplify noise (Fig. 4.5), and is reliable across a wide range of nanoparticle sizes, conditions, and SNRs (See Fig. 4.6).

Deconvolution, on the other hand, aims to reverse the effect of the system blur through inversion. A typical imaging system, e.g., camera, medical imaging modalities, is a low pass filter. When an input passes through the system, the high spatial frequency content is inevitably filtered out. For the frequency content that was filtered below the noise floor of the system, those frequencies are completely lost. Deconvolution is trying to proportionally amplify these attenuated high frequencies according to the inverse of the system filter, but in this process, not only the high frequencies are amplified, the noises are amplified dramatically. The key limitation of any deconvolution technique is the choice of the regularization parameter, which is an estimate of image SNR. Choice of this regularization parameter can be unreliable, particularly in images that do not have a consistent SNR throughout the image, e.g., images with high dynamic range with high and low SNR regions adjacent to each other.

We can begin exploring the noise properties of equalization through simple inspection. Fig. 4.3 shows that the filter gain of the equalization filter is never greater than unity, *indicating that the filter does not amplify noise.* We have also solved for equalization filters analytically, which confirm this result (See Table 4.1).

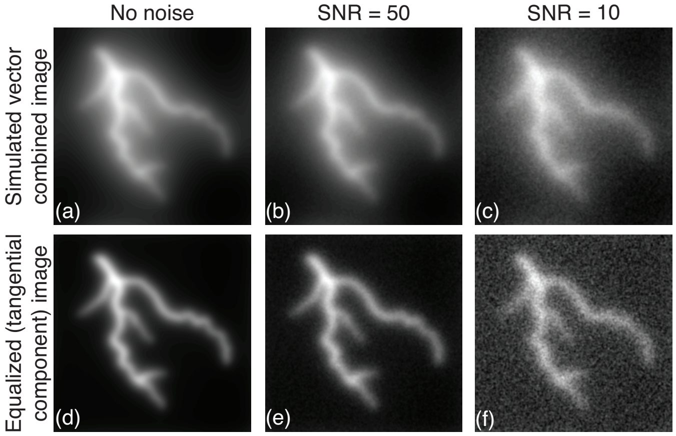

Figure 4.5: Noise performance of the equalization filter. [Top] Simulated images of an arterial phantom with combined multichannel acquistion on a Gertrude equivalent scanner, adding the following levels of noise: (a) No additional noise. (b) Peak SNR = 50. (c) Peak SNR = 10. [Bottom] Equalized images showing removed haze and the same level of background noise to their corresponding input images. It is noted that in (f) the background noise looks more grainy. However, it is not because the noise is amplified, but because the noise was unmasked due to the removal of haze.

One of the big advantage of using this equalization filter to dehaze over other deconvolution methods is that it does not amplify noise and is stable for low SNR or high dynamic range images. To illustrate the noise performance of this filter, we perform the filter on a series of simulated image that are synthetically added white Gaussian noise with known noise power.

Figure 4.5 shows an example of applying the equalization filter to a virtual arterial phantom, and it demonstrated the filter's performance regarding resolution and noise. In all the three cases simulated here, first without noise, and then with peak SNR of 50 and 10, we can see that the result after equalization contains no haze from the the normal envelope $E_N(\vec{\mathbf{x}})$, and it is confirmed to have the same resolution to the tangential component of the image.

With added noise, we confirm that the equalization filter does not amplify noise in the equalized image. It is noteworthy that in the case of SNR = 10, the equalized image Fig. 4.5f visually seems to be more noisy than Fig. 4.5c, as the noise background seems to be more grainy, however, with a complete analysis of the noise power before and after equalization, there is no ampfilication at all. The reason for this misleading visual noise gain is that the equalization filter removes the haze. The haze has a lot of signal energy, and effectively masks the noise in the original image, therefore with a peak SNR = 10, the original image Fig. 4.5c visually looks a lot better than a typical SNR = 10 image. Now with the equalization filter and removal of the haze in Fig. 4.5f, the noise is unmasked. In practice, we can apply a hamming window in k-space in addition to the equalization filter to improve image quality, by mitigating the higher frequency noises outside of the image bandwidth.

Note that we can both increase resolution and yet do not amplify noise with this equalization filter, because fundamentally, equalization technique is very different from deconvolution. In deconvolution, one is trying to make a guess of the already lost higher k-space information, and this operation is very risky in amplifying noise and introducing ringing. As we discussed earlier, with regularization, we can make a more educated guess of the attenuated higher k-space information by the SNR in that frequency band; however, regularization could arbitrarily suppress lower intensity regions in the image and lead to misdiagnosis. The equalization filter, however, does not attempt to restore any of the lost higher k-space information, but only tries to de-emphasize the over-accentuated low k-space frequencies with a full understanding of the composition of these frequencies. The shape of the equalization filter is completely determined from first principles physics, and thus there is no need for regularization, no noise amplification, and no ringing effect.

4.2.2 Robustness of the Equalization Filter

Another concern for the universal application of this equalization filter is whether it is robust to different particles. When the tracer has different sizes or structures, or it experiences different physiological microenvironment during a scan, the tracer would exhit very different PSFs with different resolution and relaxation effect. However, it is good news that the equalization filter is not very sensitive to all of these changes in the tracer, and thus would not require additional calibrations before each study.

We run two tests on two groups of particles with different sizes on the scanner, and applied multichannel aquisition, averaging and equalization filter on both data set. To cross-verify the resolution obtained after the equalization filter, we run the same tracer with a much higher concentration on relaxometor [11,12], which is essentially a 0-D imager (see Fig. 4.6). The relaxometer is used to make an accurate measurement of the 1D profile of the tangential envelope of the particles as well as relaxation, and specifically it is a tool to characterize the relaxation effect from different sizes or micro-enviroment. It serves as a good cross-validation to compare with the resolution from the equalized scanner imaging data.

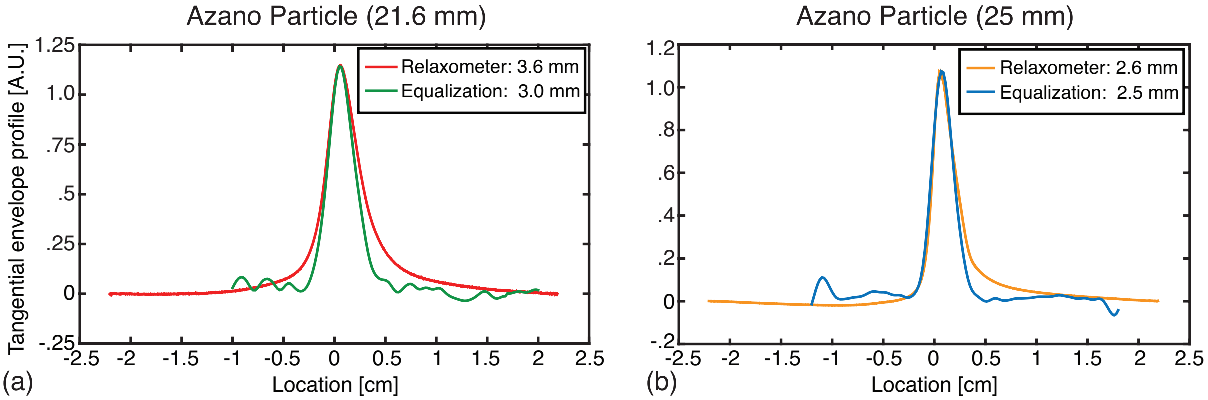

Figure 4.6: Illustration of robustness of the equalization filter to two different sizes of Azano nanoparticles. In both sets of experiments, we compared the 1D PSF profile from $1\mu L$ of undiluted Anazo particles after equalization to the 1D relaxometer data of 400 μL of the same Azano particles. The equalized resolution is consistent with the relaxometer resolution for both groups of particles, showing that this equalization filter works for both particle sizes and is thus robust. (a) Azano particle of 21.6 nm, with mostly Neel relaxation. (b) Azano particle of 25 nm, with a worse resolution and Brownian relaxation.

In the experiment, we acquired the PSFs from two Azano nanoparticles with 21.6 nm and 25 nm core size respectively from the relaxometer. The experiments were run at 25 kHz, with a drive field amplitude of 40 mTpp, and the sample quantity is 400 μL undiluted Azano tracers. The acquired PSF reflects only the 1D profile of the tangential envelope $E_T(\vec{\mathbf{x}})$ that is blurred by the relaxation effect. It could be shown that for 21.6 nm Azano particles, the PSF is more symmetric and broader, meaning it has less Browian relaxation effect and a bigger FWHM due to the smaller core size; for 25 nm Azano particle, the PSF is more assymetric and narrower, meaning it has more Brownian relaxation effect and a sharper FWHM, thus better resolution. We also made a point source with 5 μg iron (1 μL) of each tracer and imaged them on the scanner, with a drive frequency of 20.5 kHz and a drive field amplitude of also 40 mTpp, followed by the reconstruction and equalization proposed in this paper. After equalization, we plot the profile of the resultant image, which should also be only the tangential component.

Seen in Fig. 4.6, the equalized PSF has very similar resolution to the relaxometer data, with a more suppressed relaxation effect (the right side of the PSF dies off much faster to zero) because the equalization filter could suppress some of the low k-space frequency relaxation effect. Thus, the equalized PSF is closer in form to the desired tangential envelope. It shows that the equalization filter works well with both particle sizes and indeed is insensitive to the particle differences and can be applied universally.

4.3 Methods and Materials

4.3.1 Phantom Construction

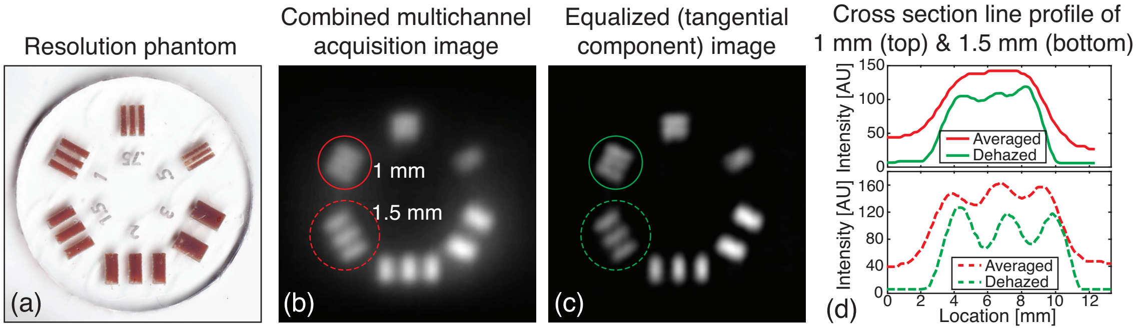

Resolution phantom

Combined multichannel acquisition image

Equalized (tangential component) image

Cross section line profile of 1 mm (top) & 1.5 mm (bottom)

Figure 4.7: Experimental data on a resolution phantom show resolution and contrast improvement with combining two orthogonal channels and equalization. (a) Photograph of a resolution acrylic phantom injected with 5x diluted Micromod Nanomag-MIP particles. The laser-cut numbers represent the width and spacing of the channels within each group, with the unit in [mm]. (b) Combining two orthogonal collinear scans achieves isotropic resolution. (c) Equalization filter in k-space de-hazes the averaged image without amplifying noise. (d) Intensity profile comparison of two lines across the averaged and dehazed images. Top graph shows the intensity profile of the 1mm bars, and it shows that the three bars are resolvable after dehazing. Bottom graph shows the intensity profile of the 1.5 mm bars. As both graphs show that dehazing significantly removes the background haze and increases contrast.

To validate the resolution improvement by this proposed method, we constructed a resolution phantom (Fig. 4.7a), and we evenly distributed 6 groups of channels around the circumference of the phantom. Within each group, the channels are separated by a well controlled distance, from 3 mm to 0.5 mm. We then injected the channels with 5x diluted Micromod nanomeg Mip particles and seal the channels with clear nail polish.

We also constructed a "Cal" phantom (see Fig. 4.8a), which was 2 mm channels laser-cutted out of an acrylic plate. The channels were then injected with undiluted Micromod nanomag-MIP particles (micromod Partikeltechnologie GmbH, Germany).

Lastly, we constructed a coronary artery phantom (Fig. 4.1a) designed using Illustrator (Adobe Systems Inc.), and laser engraved out of an acrylic plate. We then injected the arterial channels with 5x diluted Micromod nanoparticles and sealed the channels with transparent tape and clear nail polish.

4.3.2 Rat Preparation

We injected 100 uL Resovist (Bayer AG) SPIO tracer, diluted ten-fold in PBS, through the tail vein of a Fisher 344 female rat (7 weeks old, 140 g) under isofluorane anesthesia at 1.5 L/min (4% isofluorane for induction, 2% to maintain anesthesia). Approximately one hour post-injection, we sacrificed the animal via isofluorane overdose and imaged the animal using a 7 T/m 3D MPI scanner, with 591 second scan time and FOV 4 cm (X) by 3.75 cm (Y) by 9.5 cm (Z).

Subsequent to MPI imaging, we acquired CT anatomical images of the animal using a RS9-80 Micro CT scanner (GE Healthcare) with 25 minutes acquisition time and 184 um isotropic resolution. MPI-CT image coregistration was performed in an OsiriX image viewer (Pixmeo SARL).

4.3.3 Scanning Parameters

The experiments were performed with linear excitations. In each set of experiments, we acquire two orthogonal colinear scans. In each scan, the FFP is excited sinusoidally in one direction with the excitation coils, and the pFOV is then rastered with a cartesian trajectory across the FOV. Mechanical movement of the sample occurs in the z axis with 67% partial field of view overlap.

For the “Cal” phantom, the imaging FOV for collinear y scan is 2 cm by 4.1 cm by 10 cm along x, y and z axis respectively. The scan time is 7.5 minutes. The imaging FOV for collinear z scan is 2 cm by 4.5 cm by 9.9 cm, with a scan time of 2 minutes.

For the resolution phantom and the coronary artery phantom, the imaging FOVs for both channels were 2 cm by 4.5 cm by 5 cm, with a y scan time of 3.75 minutes, and z scan time of 1 minute.

4.3.4 Reconstruction / Post-Processing

To reconstruct and process the MPI imaging data, we first reconstruct each collinear channel separately with x-space reconstruction in software (MATLAB, Mathworks, Natik, MA). The signal is normalied by the receive coil sensitivity, and interpolated onto the same sampling density and averaged to form a composite image. Then images were then equalized in k-space to produce the final images.

Figure 4.8: Experimental data on a "Cal" shaped phantom shows resolution and contrast improvement with equalization filter. (a) Photograph of a "Cal" shaped acrylic phantom. (b) Combined image from multichannel acquisition shows isotropic resolution and uniform channel width. (c) Equalization filter dehazes the image without amplifying noise, improving resolution and image quality.

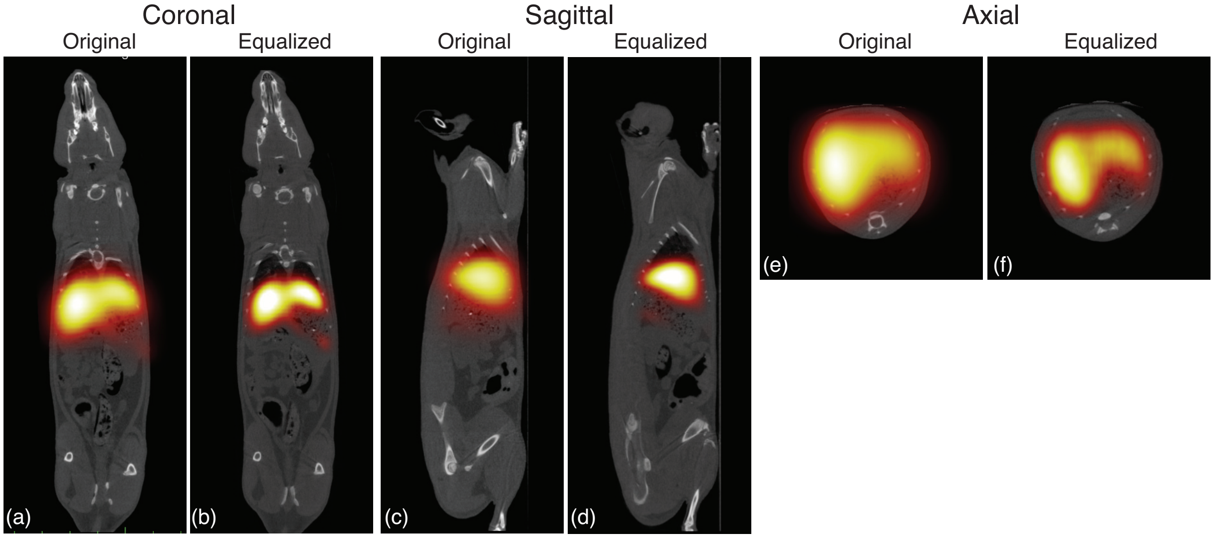

Figure 4.9: Equalization improves MPI native resolution and contrast in *in vivo* MPI imaging. Experimental rat data was acquired with a 7 T/m x 3.5 T/m x 3.5 T/m MPI scanner with only z RF channel. The rat was sacrificed and imaged 15 minutes after injecting Resovist nanoparticles. (a,c,e) Coronal, sagittal and axial multiplanar reconstruction (MPR) views of the rat liver image, exhibiting substantial background haze. (b,d,f) Coronal, sagittal and axial MPR views of the equalized rat liver image, with the background haze removed, and the spleen structure more resolvable.

4.3.5 Robustness Testing (SNR, Different Nanoparticles)

To test whether the equalization filter is robust for images with different levels of noise, we performed equalization on a series of synthetic images with known noise powers. We analyzed the resolution, ringing and SNR after equalization. The noise performance of the equalization filter across images with different input SNR can be seen in Fig. 4.5.

We then experimentally tested the sensitivity of the equalization filter to nanoparticle size against a set of nanoparticle. For validation, we also tested these particles on the relaxometer, which gives ideal the 1D PSF. We compared the equalized PSF from these particles with their corresponding relaxometer PSF, and the result is shown in Fig. 4.6.

4.4 Results

$f(r)$	Approx	$\mathbb{F}_{1D}(k)$	$\mathbb{F}_{2D}(k)/\mathbb{H}_0(k)$	$\mathbb{F}_{3D}(k)$
$\dot{\mathscr{L}}(r) = 1 - \coth^2(r) + \frac{1}{r^2}$	$\frac{4}{3(4+r^2)}$	$\frac{2\pi}{3} e^{-4\pi\lvert k\rvert}$	$\frac{8\pi}{3} K_0(4\pi \lvert k\rvert)$	$-\frac{4\pi}{3\lvert k\rvert} e^{-4\pi\lvert k\rvert}$
$\frac{\mathscr{L}(r)}{r} = \frac{\coth(r)}{r} - \frac{1}{r^2}$	$\frac{2\arctan\left(\frac{r}{2}\right)}{3r}$	$-\frac{2\pi}{3} Ei(-4\pi \lvert k\rvert)$	$\approx \frac{16}{33\lvert k\rvert} K_0(4\pi \lvert k\rvert)$	$-\frac{1}{3\lvert k\rvert^2} e^{-4\pi\lvert k\rvert}$

Table 4.1: Elementary functions to approximate PSF envelopes as well as the analytic expressions for 1D, 2D and 3D Fourier transforms of both envelopes, $r = \frac{\|\mathbf{G}\vec{\mathbf{x}}\|}{H_{sat}}$.

Table 4.1 briefly summarizes the analytic expressions of the two envelopes as well as their Fourier transforms of a 1D line profile, 2D plane and 3D volume of the envelopes. The derivation of the equalization filter uses these analytic formulas.

In Fig. 4.7 we see how multidimensional acquisition and equalization improves resolution and conspicuity in a resolution phantom. After combining the multichannel acquisitions, Fig, 4.7b shows isotropic resolution. The equalized image is shown in Fig. 4.7c, showing that the equalization filter removes the image haze. Fig. 4.7d compares the image intensity before and after equalization, showing the equalization filter improves both resolution and conspicuity of the MPI image.

In Fig. 4.8 we see equalization filter improving resolution and image contrast in a “Cal” shaped phantom with no noise gain.

In Fig. 4.9 we show how multidimensional acquisition and equalization enable improved images in an *in vivo* rat injected with Resovist. Fig 4.9a,c,e shows before equalization, and Fig 4.9b,d,e shows the improvement after equalization. Especially to be noted is the spleen structure in the image, which shows up a lot more obviously in the equalized images, showing that the equalization filter could really resolve finer structures that would’ve otherwise been lost in the original MPI scans.

4.5 Conclusion

We proved and experimentally demonstrated that we can reshape the MPI PSF to be isotropic and well-behaved with multichannel acquisition and equalization. This allows us to improve MPI resolution and image contrast with no noise amplification. Finally, these improvements enable us to use MPI to quantitatively measure the lumen diameter of small arteries in angiograms and

Each of these improvements, multichannel excitation and equalization, taken individually improve image resolution contrast only modestly. However, taken together, these improvements dramatially increase image contrast and enable the first quantitative measurements of lumen area in a sub-millimeter diameter blood vessel phantom.

Bibliography

[1] J.L. Prince and J.M. Links. *Medical imaging signals and systems.* Pearson Prentice Hall Upper Saddle River, NJ, 2006.

[2] Jurgen Rahmer, Jurgen Weizenecker, Bernhard Gleich, and Jorn Borgert. Signal encoding in magnetic particle imaging: properties of the system function. *BMC Medical Imaging*, 9(1), 2009.

[3] Jurgen Rahmer, Jurgen Weizenecker, Bernhard Gleich, and Jorn Borgert. Analysis of a 3-D system function measured for magnetic particle imaging. *IEEE Trans Med Imag*, 31(6):1289–1299, 2012.

[4] Patrick W Goodwill and Steven M Conolly. The X-space formulation of the magnetic particle imaging process: 1-D signal, resolution, bandwidth, SNR, SAR, and magnetostimulation. *IEEE transactions on medical imaging*, 29(11):1851–1859, 2010.

[5] Patrick W Goodwill and Steven M Conolly. Multidimensional x-space magnetic particle imaging. *IEEE transactions on medical imaging*, 30(9):1581–1590, 2011.

[6] Tobias Knopp, Sven Biederer, Timo F Sattel, Marlitt Erbe, and Thorsten M Buzug. Prediction of the spatial resolution of magnetic particle imaging using the modulation transfer function of the imaging process. *IEEE transactions on medical imaging*, 30(6):1284–1292, 2011.

[7] CR Huang, WD Pan, HQ Chen, and AL Copley. Thixotropic properties of whole blood from healthy human subjects. *Biorheology*, 24(6):795–801, 1986.

[8] R. Fahraus and T. Lindqvist. The viscosity of the blood in narrow capillary tubes. *American Journal of Physiology*, 96.

[9] J Weizenecker, B Gleich, J Rahmer, and J Borgert. Particle dynamics of mono-domain particles in magnetic particle imaging. *Magnetic nanoparticles: particle science, imaging technology, and clinical applications. Singapore: World Scientific Publishing Co Pte Ltd*, pages 3–15, 2010.

[10] DB Reeves and JB Weaver. Simulations of magnetic nanoparticle Brownian motion. *Journal of Applied Physics*, 112(12), 2012.

[11] PW Goodwill, A Tamrazian, LR Croft, et al. Ferrohydrodynamic relaxometry for magnetic particle imaging. *Applied Physics Letters*, 98(26), 2011.

[12] Laura R Croft, Patrick W Goodwill, and Steven M Conolly. Relaxation in x-space magnetic particle imaging. *IEEE transactions on medical imaging*, 31(12), 2012.

[13] R Matthew Ferguson, Amit P Khandhar, Christian Jonasson, et al. Size-Dependent Relaxation Properties of Monodisperse Magnetite Nanoparticles Measured Over Seven Decades of Frequency by AC Susceptometry. *IEEE Transactions on Magnetics*, 49(7), 2013.

[14] JP Reilly. Maximum pulsed electromagnetic field limits based on peripheral nerve stimulation: application to IEEE/ANSI C95. 1 electromagnetic field standards. *IEEE Transactions on Biomedical Engineering*, 45(1):137–141, 1998.

[15] JP Reilly. Peripheral nerve stimulation by induced electric currents: exposure to time-varying magnetic fields. *Medical and Biological Engineering and Computing*, 27(2):101–110, 1989.

[16] EU Saritas, PW Goodwill, GZ Zhang, and W Yu. Safety limits for human-size magnetic particle imaging systems. In T.M. Buzug; and J. Borgert, editors, *Magnetic Particle Imaging*, volume 140, pages 325–330, Lubeck, Germany, 2012. Springer Proceedings in Physics.

[17] J Weizenecker, B Gleich, J Rahmer, H Dahnke, and J Borgert. Three-dimensional real-time in vivo magnetic particle imaging. *Physics in medicine and biology*, 54(5):L1–LL10, 2009.

[18] J. Rahmer, B. Gleich, J. Schmidt, et al. Increased volume coverage in 3D magnetic particle imaging. *Proceedings of the 4th International Symposium on Applied Sciences in Biomedical and Communication Technologies - ISABEL '11*, C(1):1–5, 2011.

[19] I. Schmale, J. Rahmer, B. Gleich, et al. First phantom and in vivo MPI images with an extended field of view. *Proceedings of SPIE medical imaging*, 2011.

[20] P. W. Goodwill, J. J. Konkle, Bo Zheng, E. U. Saritas, and S. T. Conolly. Projection X-Space Magnetic Particle Imaging. *IEEE Transactions on Medical Imaging*, 31(5):1076–1085, 2012.

[21] T Knopp, S Biederer, T Sattel, et al. Trajectory analysis for magnetic particle imaging. *Physics in medicine and biology*, 54(2):385–397, 2009.

[22] Patrick W Goodwill, Kuan Lu, Bo Zheng, and Steven M Conolly. An x-space magnetic particle imaging scanner. *The Review of scientific instruments*, 83(3), 2012.

[23] B Gleich and J Weizenecker. Tomographic imaging using the nonlinear response of magnetic particles. *Nature*, 435(7046):1214–1217, 2005.

[24] B Zheng, W Yang, and T Massey. High-power active interference suppression in magnetic particle imaging. *Magnetic Particle Imaging (IWMPI), 2013 International Workshop on. IEEE,*, 2013.

[25] B Zheng, T Vazin, W Yang, and PW Goodwill. Quantitative stem cell imaging with magnetic particle imaging. *Magnetic Particle Imaging (IWMPI), 2013 International Workshop on. IEEE,*, 2013.

[26] Emine U Saritas, Patrick W Goodwill, Laura R Croft, et al. Magnetic particle imaging (MPI) for NMR and MRI researchers. *Journal of magnetic resonance (San Diego, Calif. : 1997)*, 229:116–126, 2013.

[27] J Weizenecker, J Borgert, and B Gleich. A simulation study on the resolution and sensitivity of magnetic particle imaging. *Physics in Medicine and Biology*, 52(21):6363–6374, 2007.

[28] QA Pankhurst, J Connolly, and SK Jones. Applications of magnetic nanoparticles in biomedicine. *Journal of physics D: Applied physics*, 36(13):R167, 2003.

[29] Leslie LaConte, Nitin Nitin, and Gang Bao. Magnetic nanoparticle probes. *Materials Today*, 8(5):32–38, 2005.

[30] EA Neuwelt, BE Hamilton, CG Varallyay, et al. Ultrasmall superparamagnetic iron oxides (USPIOs): a future alternative magnetic resonance (MR) contrast agent for patients at risk for nephrogenic systemic fibrosis (NSF)? *Kidney International*, 75(5):465–474, 2008.

[31] M Lu, MH Cohen, D Rieves, and R Pazdur. FDA report: Ferumoxytol for intravenous iron therapy in adult patients with chronic kidney disease. *American Journal of Hematology*, 85(5):315–319, 2010.

[32] R Weissleder, DD Stark, BL Engelstad, et al. Superparamagnetic iron oxide: pharmacokinetics and toxicity. *American Journal of Roentgenology*, 152(1):167–173, 1989.

[33] P Goodwill, E Saritas, L Croft, et al. X-Space MPI: Magnetic Nanoparticles for Safe Medical Imaging. *Advanced materials*, 24(28), 2012.

[34] J Borgert, JD Schmidt, I Schmale, et al. Fundamentals and applications of magnetic particle imaging. *Journal of cardiovascular computed tomography*, 6(3), 2012.

[35] J Rahmer, A Antonelli, C Sfara, et al. Nanoparticle encapsulation in red blood cells enables blood-pool magnetic particle imaging hours after injection. *Physics in medicine and biology*, 58(12):3965–3977, 2013.

[36] J Weizenecker, B Gleich, and J Borgert. Magnetic particle imaging using a field free line. *Journal of Physics D: Applied Physics*, 41(10), 2008.

[37] M Erbe, T Knopp, TF Sattel, S Biederer, and TM Buzug. Experimental generation of an arbitrarily rotated field-free line for the use in magnetic particle imaging. *Medical physics*, 38(9):5200–5207, 2011.

[38] Justin J Konkle, Patrick W Goodwill, Oscar M Carrasco-Zevallos, and Steven M Conolly. Projection reconstruction magnetic particle imaging. *IEEE transactions on medical imaging*, 32(2):338–347, 2013.

[39] TF Sattel, T Knopp, S Biederer, et al. Single-sided device for magnetic particle imaging. *Journal of Physics D: Applied Physics*, 42(2), 2009.

[40] J Haegele, J Rahmer, B Gleich, et al. Magnetic particle imaging: visualization of instruments for cardiovascular intervention. *Radiology*, 265(3), 2012.

[41] J Haegele, S Biederer, H Wojtczyk, et al. Toward cardiovascular interventions guided by magnetic particle imaging: First instrument characterization. *Magnetic Resonance in Medicine*, 69(6), 2013.

[42] P Vogel, MA Ruckert, and P Klauer. Traveling wave magnetic particle imaging. *Medical Imaging, IEEE Transactions on*, 33(2):400–407, 2014.

[43] RM Ferguson, KR Minard, and KM Krishnan. Optimization of nanoparticle core size for magnetic particle imaging. *Journal of Magnetism and Magnetic Materials*, 321(10), 2009.

[44] RM Ferguson, KR Minard, AP Khandhar, and KM Krishnan. Optimizing magnetite nanoparticles for mass sensitivity in magnetic particle imaging. *Medical Physics*, 38(3), 2011.

[45] RM Ferguson, AP Khandhar, and KM Krishnan. Tracer design for magnetic particle imaging (invited). *Journal of Applied Physics*, 111(7), 2012.

[46] RJ Deissler, Y Wu, and MA Martens. Dependence of Brownian and Néel relaxation times on magnetic field strength. *Medical physics*, 41(1), 2014.

[47] JB Weaver, X Zhang, E Kuehlert, et al. Quantification of magnetic nanoparticles with low frequency magnetic fields: compensating for relaxation effects. *Nanotechnology*, 24(32), 2013.

[48] J Rahmer, A Halkola, B Gleich, I Schmale, and J Borgert. First experimental evidence of the feasibility of multi-color magnetic particle imaging. *Physics in Medicine and Biology*, 60(5):1775–1791, 2015.

[49] T Knopp, J Rahmer, T F Sattel, et al. Weighted iterative reconstruction for magnetic particle imaging. *Physics in medicine and biology*, 55(6):1577–1589, 2010.

[50] T Knopp, T Sattel, S Biederer, et al. Model-based reconstruction for magnetic particle imaging. *Medical Imaging, IEEE Transactions on*, 29(1):12–18, 2010.

[51] J Konkle, P Goodwill, Carrasco-Zevallos, O, and S Conolly. Experimental 3D X-space magnetic particle imaging using projection reconstruction. pages 243–247, 2012.

[52] Kuan Lu, Patrick W Goodwill, Emine U Saritas, Bo Zheng, and Steven M Conolly. Linearity and shift invariance for quantitative magnetic particle imaging. *IEEE transactions on medical imaging*, 32(9):1565–1575, 2013.

[53] EU Saritas, PW Goodwill, and D Chang. Effects of frequency and pulse duration on magnetostimulation limits for MPI. *Magnetic Particle Imaging (IWMPI), 2013 International Workshop on*, 2013.

[54] EU Saritas, PW Goodwill, and GZ Zhang. Magnetostimulation limits in magnetic particle imaging. *Medical Imaging, IEEE Transactions on*, 32(9):1600–1610, 2013.

[55] P Goodwill, L Croft, J Konkle, et al. Third generation X-space MPI mouse and rat scanner. pages 261–265, 2012.

[56] A Clausing and W Kautter. Linear Distortions in Broadcast Receivers and Their Compensation by Low-Frequency Equalization Devices. *Radio Engineers, Proceedings of the Institute of*, 20(9), 1932.

[57] HH Scott. The Philosophy of Amplifier Equalization. *Journal of the Audio Engineering Society*, 2(1), 1954.

[58] Wolfram Research Inc. Chebyshev polynomials of the second kind: Summation. `http://functions.wolfram.com/Polynomials/ChebyshevU`, Oct. 29, 2001 [Jan. 15, 2013].

Appendix A

Sum of Harmonic Components Manifests Linearity and Shift-Invariance

One apparent paradox uncovered in the analysis in Chapter 1 is the fact that each harmonic image is *shift variant*, yet the sum of *all* basis images is *shift invariant.* Here we resolve this paradox by summing all the harmonic basis functions, and showing that the shift-variant term, $\sqrt{1-(2x/W)^2}$, cancels out *only* after we add all the terms together.

Here, we rely on the Chebyshev polynomial identity [58]:

$$\sum_{n=0}^{\infty} U_n\left(x\right) U_n\left(y\right) = \frac{\pi}{2} \frac{1}{\left(1-x^2\right)^{-1/4} \left(1-y^2\right)^{-1/4}} \delta(x-y)$$

First, we adapted the analytic expression of S_n from [**?**] to our notations, which has the form:

$$S_n = \beta \int_{-\frac{W}{2}}^{\frac{W}{2}} \hat{\rho}(x) U_{n-1}\left(\frac{2x}{W}\right) \sqrt{1-\left(\frac{2x}{W}\right)^2} dx \tag{A.1}$$

where $\beta = -4B_1 mGf_0/H_{sat}$, is a constant dependent on scanning parameters and particle properties; and $\hat{\rho}(x)$, is the native MPI image reconstructed using the x-space method.

Let us substitute the Fourier coefficient S_n into the image decomposition equation (Eqn. 1.7). We have:

$$\begin{aligned}
\hat{\rho}(x) &= \sum_{n=1}^{\infty} S_n \alpha U_{n-1}\left(\frac{2x}{W}\right) \\
&= \sum_{n=1}^{\infty} \alpha\beta \left[\int_{-\frac{W}{2}}^{\frac{W}{2}} \hat{\rho}(u) U_{n-1}\left(\frac{2u}{W}\right)\sqrt{1-\left(\frac{2u}{W}\right)^2}\,du\right] U_{n-1}\left(\frac{2x}{W}\right) \\
&= \alpha\beta \int_{-\frac{W}{2}}^{\frac{W}{2}} \left\{\hat{\rho}(u)\left[\sum_{n=1}^{\infty} U_{n-1}\left(\frac{2u}{W}\right) U_{n-1}\left(\frac{2x}{W}\right)\right]\sqrt{1-\left(\frac{2u}{W}\right)^2}\,du\right\} \\
&= \frac{\pi}{2}\alpha\beta \int_{-\frac{W}{2}}^{\frac{W}{2}} \hat{\rho}(u) \frac{\sqrt[4]{1-(2u/W)^2}}{\sqrt[4]{1-(2x/W)^2}} \delta\left(\frac{2}{W}(u-x)\right) du \\
&= \frac{\pi W}{4}\alpha\beta\hat{\rho}(x) = \hat{\rho}(x)
\end{aligned}$$

We conclude that the sum of all the *linear but shift-variant* harmonic images does indeed provide a *linear and shift-invariant* MPI image.

Appendix B

Mathematical Proof of LSI Restoration

Here we give a complete derivation of the DC recovery algorithm and prove that our algorithm robustly restores all the lost image information, and the linearity and shift invariance of MPI images.

First of all, let us denote the ideal native MPI image as $\hat{\rho}(x)$, the center position of each pFOV as x_i, the noise in this pFOV image as $n_i(x)$. Let us also denote the lost DC value from the i^{th} pFOV scan as δ_i, while the estimator of this lost DC value as $\hat{\delta}_i$. Then with an unmodified x-space reconstruction, the lossy pFOV image will have this form:

$$g_i(x) = \hat{\rho}(x) + n_i(x) - \delta_i, \text{ for } |x - x_i| < W/2 \tag{B.1}$$

The lost DC value δ_i can be estimated by maximizing the continuity between the i^{th} pFOV scan and its previous scans over the overlapping region. Let us denote P_i as the dataset that includes all the points within the overlapping region between the i^{th} and $(i-1)^{th}$ pFOV scan, which is defined as $P_i \triangleq \left[x_i - \frac{W}{2},\, x_{i-1} + \frac{W}{2}\right]$. Let's further denote $g_0(x) \triangleq 0$ and $n_0(x) \triangleq 0$, corresponding to a virtual 0^{th} scan that incorporates the boundary condition into the same mathematical framework. Thus, the process of estimation for each DC offset, $\hat{\delta}_i$, can be expressed as

$$\begin{aligned} \hat{\delta}_i &= \sum_{k=1}^{i} \underset{x \in P_k}{\text{mean}} \left\{ g_{k-1}(x) - g_k(x) \right\} \\ &= \delta_i - \sum_{k=1}^{i} \underset{x \in P_k}{\text{mean}} \left\{ n_k(x) - n_{k-1}(x) \right\} \end{aligned} \tag{B.2}$$

As one would hope, $\hat{\delta}_i$ is an unbiased estimate of the actual DC loss to each pFOV, provided that all the image noise, $n_i(x)$, is zero-mean, i.e.,

$$E\left\{\hat{\delta}_i\right\} = \delta_i \tag{B.3}$$

where $E\{X\}$ denotes the expected value of a random variable X.
After restoring the DC values to each of the pFOVs, our final estimate of the true MPI nanoparticle density can be computed as

$$\hat{g}_i(x) = g_i(x) + \hat{\delta}_i \cong \hat{\rho}(x) + n_i(x), \text{ for } |x - x_i| < W/2 \tag{B.4}$$

This analysis proves that restored image $\hat{g}_i(x)$ is an unbiased estimation of the ideal native MPI image $\hat{\rho}(x)$ with no amplification of noise and within the same subregion, which we already know to be linear and shift invariant from Eqn. 1.5. This algorithm obtains (at least) two estimates of the native MPI image in the overlapping zone, and we can average these to reduce image noise. To form our final MPI image, we simply join all the pFOVs numerically on an interpolated uniform grid that spans the full FOV. This algorithm is able to reconstruct an accurate rendition of the ideal MPI image $\hat{\rho}(x)$, with fully restored LSI properties. Fig. 1.7 and Fig. 1.8 illustrates the recovered images from both simulation and experiment, demonstrating that the continuity algorithm does recover the lost DC image information.

Appendix C

Proof of 3 orthogonal colinear scans for isotropic resolution

In this section, we will prove that by combining three orthogonal collinear scans, we can achieve isotropic resolution. As shown in Eq. 4.1, the analytic expression of the combined three orthogonal collinear scans is

$$\begin{aligned}\hat{\rho}\left(\vec{\mathbf{x}}\right) &= \mathrm{trace}[\mathbf{\Omega}(\vec{\mathbf{x}})\mathbf{G}^{-1}] \\ &= \sum_{i=1}^{3}\hat{\mathbf{e}}_{\mathbf{i}}^{\mathbf{T}}\mathbf{\Omega}\left(\vec{\mathbf{x}}\right)\mathbf{G}^{-\mathbf{1}}\hat{\mathbf{e}}_{\mathbf{i}} &\text{(C.1)} \\ &= \rho\left(\vec{\mathbf{x}}\right) *** \sum_{i=1}^{3}\hat{\mathbf{e}}_{\mathbf{i}}^{\mathbf{T}}\mathbf{h}\left(\vec{\mathbf{x}}\right)\mathbf{G}^{-\mathbf{1}}\hat{\mathbf{e}}_{\mathbf{i}} &\text{(C.2)}\end{aligned}$$

Let us denote the unit vector $\frac{\mathbf{G}\vec{\mathbf{x}}}{\|\mathbf{G}\vec{\mathbf{x}}\|}$ as $\vec{\mathbf{r}}\left(\vec{\mathbf{x}}\right)$, thus $\mathbf{W}_T\left(\vec{\mathbf{x}}\right) = \vec{\mathbf{r}}\left(\vec{\mathbf{x}}\right)\vec{\mathbf{r}}\left(\vec{\mathbf{x}}\right)^{\mathbf{T}}\mathbf{G}$, and $\mathbf{W}_N\left(\vec{\mathbf{x}}\right) = \mathbf{G} - \mathbf{W}_T\left(\vec{\mathbf{x}}\right)$. Thus

$$\begin{aligned}\hat{\rho}\left(\vec{\mathbf{x}}\right) &= \rho\left(\vec{\mathbf{x}}\right) *** \left(E_T\left(\vec{\mathbf{x}}\right)\sum_{i=1}^{3}\hat{\mathbf{e}}_{\mathbf{i}}^{\mathbf{T}}\vec{\mathbf{r}}\left(\vec{\mathbf{x}}\right)\vec{\mathbf{r}}\left(\vec{\mathbf{x}}\right)^{\mathbf{T}}\hat{\mathbf{e}}_{\mathbf{i}}\right. \\ &\qquad \left. + E_N\left(\vec{\mathbf{x}}\right)\left[3 - \sum_{i=1}^{3}\hat{\mathbf{e}}_{\mathbf{i}}^{\mathbf{T}}\vec{\mathbf{r}}\left(\vec{\mathbf{x}}\right)\vec{\mathbf{r}}\left(\vec{\mathbf{x}}\right)^{\mathbf{T}}\hat{\mathbf{e}}_{\mathbf{i}}\right]\right) &\text{(C.3)}\end{aligned}$$

As has been shown, the two envelopes $E_T\left(\vec{\mathbf{x}}\right)$ and $E_N\left(\vec{\mathbf{x}}\right)$ are isotropic. Therefore, for the entire equation to remain isotropic, it hinges on the isotropy of $\sum_{i=1}^{3}\hat{\mathbf{e}}_{\mathbf{i}}^{\mathbf{T}}\vec{\mathbf{r}}\left(\vec{\mathbf{x}}\right)\vec{\mathbf{r}}\left(\vec{\mathbf{x}}\right)^{\mathbf{T}}\hat{\mathbf{e}}_{\mathbf{i}}$. It can be proven that the sum is merely a constant value, thus is spatially invariant:

$$\begin{aligned}\sum_{i=1}^{3}\hat{\mathbf{e}}_{\mathbf{i}}^{\mathbf{T}}\vec{\mathbf{r}}\left(\vec{\mathbf{x}}\right)\vec{\mathbf{r}}\left(\vec{\mathbf{x}}\right)^{\mathbf{T}}\hat{\mathbf{e}}_{\mathbf{i}} &= \sum_{i=1}^{3}\vec{\mathbf{r}}\left(\vec{\mathbf{x}}\right)^{\mathbf{T}}\hat{\mathbf{e}}_{\mathbf{i}}\hat{\mathbf{e}}_{\mathbf{i}}^{\mathbf{T}}\vec{\mathbf{r}}\left(\vec{\mathbf{x}}\right) \\ &= \vec{\mathbf{r}}\left(\vec{\mathbf{x}}\right)^{\mathbf{T}}\left(\sum_{i=1}^{3}\hat{\mathbf{e}}_{\mathbf{i}}\hat{\mathbf{e}}_{\mathbf{i}}^{\mathbf{T}}\right)\vec{\mathbf{r}}\left(\vec{\mathbf{x}}\right) \\ &= \vec{\mathbf{r}}\left(\vec{\mathbf{x}}\right)^{\mathbf{T}}\mathbf{I}\vec{\mathbf{r}}\left(\vec{\mathbf{x}}\right) = 1 &\text{(C.4)}\end{aligned}$$

where we make the substitution of $\sum_{i=1}^{3}\left(\hat{\mathbf{e}}_i\hat{\mathbf{e}}_i^{\mathbf{T}}\right) = \begin{bmatrix} \hat{\mathbf{e}}_1 & \hat{\mathbf{e}}_2 & \hat{\mathbf{e}}_3 \end{bmatrix}\begin{bmatrix} \hat{\mathbf{e}}_1^{\mathbf{T}} \\ \hat{\mathbf{e}}_2^{\mathbf{T}} \\ \hat{\mathbf{e}}_3^{\mathbf{T}} \end{bmatrix}$, and apply the orthogonal matrix identity $AA^T = I$, as $A = \begin{bmatrix} \hat{\mathbf{e}}_1 & \hat{\mathbf{e}}_2 & \hat{\mathbf{e}}_3 \end{bmatrix}$ is chosen to be orthogonal during scanning. If we plug Eq. C.4 into Eq. C.3, we arrive at the conclusion that

$$\hat{\rho}\left(\vec{\mathbf{x}}\right) \quad = \quad \rho\left(\vec{\mathbf{x}}\right) *** \left(E_T\left(\vec{\mathbf{x}}\right) + 2E_N\left(\vec{\mathbf{x}}\right)\right) \tag{C.5}$$

It shows that the anisotropy from the weighting matrix $\mathbf{W}_T\left(\vec{\mathbf{x}}\right)$ and $\mathbf{W}_N\left(\vec{\mathbf{x}}\right)$ goes away after weighted-summing three orthogonal scans.

Appendix D

Analytic Derivation of Equalization Filter

To find the correct form of the equalization filter, we will need to calculate the ratio of the Fourier transforms of the desired tangential envelope and the summed image:

$$\Phi_{3D,T}\left(\vec{\mathbf{k}}\right) = \frac{\mathbb{F}_{3D}\left\{E_T\left(\vec{\mathbf{x}}\right)\right\}}{\mathbb{F}_{3D}\left\{E_T\left(\vec{\mathbf{x}}\right) + 2E_N\left(\vec{\mathbf{x}}\right)\right\}}$$

For reference, here is a table of all of the approximation to the envelopes and the analytic expression of the Fourier transforms in 1D, 2D and 3D. The shape of the functions are shown as well in each corresponding section.

One theorem we used is that for a radially symmetric function, the relationship between the 3D Fourier transform and its 1D fourier transform is:

$$\mathbb{F}_{3D}\left\{f\left(r\right)\right\} = \frac{1}{2\pi k}\frac{d}{dk}\mathbb{F}_{1D}\left\{f\left(r\right)\right\}$$

And the derivative of the exponential integral is:

$$\frac{d}{dx}Ei\left(x\right) = \frac{e^x}{x}$$

Therefore, for the 3D scanner case the equalization would be:

$$\begin{aligned}\Phi_{3D,T}\left(\vec{\mathbf{k}}\right) &= \frac{\mathbb{F}_{3D}\left\{E_T\left(\vec{\mathbf{x}}\right)\right\}}{\mathbb{F}_{3D}\left\{E_T\left(\vec{\mathbf{x}}\right) + 2E_N\left(\vec{\mathbf{x}}\right)\right\}} \\ &\approx \frac{\left|\vec{\mathbf{k}}\right|}{\left|\vec{\mathbf{k}}\right| + G_0/2\pi H_{sat}}\end{aligned}$$

It is noted that there is no analytic expression for the 2D Fourier transform of the normal envelope E_N, so we can only approximate the equalization by numerically taking the ratio of the 2D Fourier transform of the two envelopes. And the approximated equalization filter for a 2D projection scanner is:

$$\begin{aligned}\Phi_{2D,T}\left(\vec{\mathbf{k}}\right) &= \frac{\mathbb{F}_{2D}\left\{E_T\left(\vec{\mathbf{x}}\right)\right\}}{\mathbb{F}_{2D}\left\{E_T\left(\vec{\mathbf{x}}\right)+2E_N\left(\vec{\mathbf{x}}\right)\right\}} \\ &\approx \frac{\left|\vec{\mathbf{k}}\right|}{\left|\vec{\mathbf{k}}\right|+G_0/5.5\pi H_{sat}}\end{aligned}$$